# The neural dynamics and intrinsic properties of heterogeneous ventral tegmental area populations in motivated behavior

Jordan Elum

A dissertation

submitted in partial fulfillment of the

requirements for the degree of

Doctor of Philosophy

University of Washington

2024

Reading Committee:

Larry Zweifel, Chair

Michael Bruchas

Garret Stuber

Program Authorized to Offer Degree:

Neuroscience

University of Washington

**Abstract**

The neural dynamics and intrinsic properties of heterogeneous ventral tegmental area populations in motivated behavior

Jordan Elum

Chair of the Supervisory Committee:

Professor Larry Zweifel

Psychiatry and Behavioral Sciences

Ventral tegmental area (VTA) dopamine neurons regulate reward-related associative learning and reward-driven motivated behaviors, but how these processes are coordinated by distinct VTA neuronal subpopulations remains unresolved. Here we examine the neural correlates of reward-related prediction-error, action, cue, and outcome encoding as well as effort exertion and reward anticipation during reward-seeking behaviors. We compare the contribution of two primarily dopaminergic and largely non-overlapping VTA subpopulations, all VTA dopamine neurons, and VTA GABAergic neurons of the mouse midbrain to these processes. The dopamine subpopulation that projects to the nucleus accumbens (NAc) core preferentially encodes prediction-error and reward-predictive cues. In contrast, the dopamine subpopulation that projects to the NAc shell preferentially encodes goal-directed actions and reflects relative reward anticipation. VTA GABA neuron activity strongly contrasts VTA dopamine population activity and preferentially encodes reward outcome and retrieval. Electrophysiology, targeted optogenetics, and whole-brain input mapping reveal heterogeneity among VTA dopamine subpopulations. Our results demonstrate that VTA subpopulations carry distinct reward-related learning and motivation signals and reveal a striking pattern of functional heterogeneity among projection-defined VTA dopamine neuron populations.

**Table of Contents**

**List of Figures and Tables**

**Acknowledgments**

I came to the University of Washington from Baltimore after a summer of travel abroad determined to study addiction during my PhD. Unsure of where to do my final rotation, I encountered Larry at a neuroscience program retreat-style symposium. I was hypnotized by his visually stunning figures and intellectually intrigued by his ability to dissect learning and motivational processes from a basic science perspective in such a satisfying way. Since joining his lab, I have learned a lifetime's worth of wisdom and knowledge about the genetic regulation of neural systems and behavior and the keys to success in academic science. He has facilitated productive collaborations, reviewed countless scientific proposals, written letters of recommendation, and encouraged and improved secret passion science projects. In some ways we live on opposite ends of a scientific spectrum spanning molecular genetic regulation of circuits and behavior to complex dynamical systems neuroscience but found a natural resonance somewhere in between.

I want to thank Michael Bruchas for reminding me that when it comes to neuroscience scholarship, reading is fundamental and that the library is open. And for providing a series of masterclasses on how to write a persuasive and actionable letter for any academic occasion. I thank Garret Stuber for providing an unwavering and aspirational standard of technical competence and mathematical rigor in studying the brain. Susan Ferguson provided a gentle and enjoyable introduction to conducting research at the UW during my rotation in her lab and provided a consistent source of calm wisdom and levity during my committee meetings. David Gire protected me from the wiles of an insular NAPE center and set the bar for thinking creatively and deeply in the study of animal behavior. Paul Phillips helped me elevate my understanding and description of the role of dopamine in behavior. Garret and Michael helped establish a collaborative center that laid the foundation for my ability to do cutting-edge and meaningful work. As a collective, you have been described as the 'dream team' for advising a thesis such as this and it has been an honor to think about science with you.

Eric, Barb, Avery, Meagan, Yong, Marta, Scott, Charles, Richard, and Seung-Woo played instrumental roles in my development as a scientist and experimental prowess. Grigory and Beatriz helped me find my footing as a scientific mentor. Adrienne Fairhall and Rajesh Rao derived all the fundamental equations of

neuroscience from scratch during the Computational Neuroscience course much to my shock, awe, and fascination.

Matt Dawson rescued me from social isolation stress at the University of Calgary retreat and fed me the answers to all my pose tracking and behavioral classification questions. Along with indispensable advice from Nastacia Goodwin, this chance encounter allowed me to process and analyze enough free dyad social interaction video data in the ten days prior to my dissertation defense and job talk to give an ‘interesting and enjoyable’ presentation on the influence of social isolation on behavior and the neural dynamics of spontaneous social interaction across neuromodulatory, cortical, and subcortical neural populations.

My mom helped me develop an appreciation of the music of the 80s and a grounded grip on reality. She said ‘sure’ when while walking to our car in the Goose Creek Publix parking lot I asked her to sell our house so that I could go to the Charleston County School of the Arts for high shcool and become a violin virtuoso superstar. This led to chance encounters with two scientists and educators, Dr. Veronica Short and Mr. Kevin Short, and one United States history teacher, Mr. Michael Donnellon, who together inspired me to pursue a career in science. My grandmother reminded me to keep in mind that ‘I like nice things’ and that life is both mysterious and full of wonder. My grandfather paved the way for my dreams of becoming a neuroscientist to come true.

My music teachers taught me how to take up space on a stage and ride the waves of adrenaline in the moment. This has been indispensable in effectively and creatively communicating my research findings and interests.

I thank Su-Yee, Lili, Todd, Ellen, Raphael, Angel, Tafari, Nico, Michael, Sidney, Flo, Levi, Rew, Jeremy, D’Marcus, Elias, Clay, and Clay for the memories.

## Dedication

To my music teachers who helped me appreciate the beauty in the spaces between the notes and forge an inner world of calm and refuge.

To all the homies who never got the chance to stick it to big dopamine. This one’s for you.

## Chapter 1

## Introduction

To survive and thrive animals must obtain access to primary reinforcers. Learning information about and maintaining motivation to pursue these goals are crucial functions of nervous systems. The evolutionarily ancient neural system involving dopamine-producing cells of the substantia nigra and ventral tegmental area (VTA) is critical for both movement and for reward association and motivational processes across phyla (Pérez-Fernández et al, 2021). However, it remains unclear how information about reward-related stimuli and motivation during reward-seeking behavior is encoded across specific VTA subpopulations and whether distinct intrinsic neurophysiological and circuit connectivity properties define these populations. Here we use fiber photometry and optogenetics during behavior to examine the neural correlates and functional significance of VTA dopamine populations and the VTA GABAergic population in reward-related associative learning and reward-driven motivational processes. Furthermore, we use electrophysiology, targeted optogenetics, and whole-brain input mapping to assess heterogeneity among these VTA subpopulations. In this section, we review prior work in the field to provide context and motivation.

### *1.1 The dopamine ascending modulatory system*

Ascending modulatory systems involve relatively small groups of neurons that synthesize monoamines and typically innervate vast swaths of forebrain resulting in powerful modulation of neocortical neural circuits and behavior. But how do these systems exert control mechanistically? Neuromodulatory neuron types including dopamine, serotonin, and norepinephrine-producing cells release monoamines via both synaptic ‘wiring’ transmission and volume transmission, a form of nonsynaptic diffusion transmission in which monoamine release can lead to the activation of receptors located up to 100 µm from individual release sites. Neuromodulators including dopamine act on G-protein coupled receptors which are widely distributed and localized to neuronal membranes across the brain and mediate diverse downstream cellular adaptations. Neuromodulatory systems regulate distinct behaviors in part due the specific distribution of their synaptic release sites across the whole brain. In terms of their behavioral relevance, neuromodulatory neurons are greatly activated by surprising or salient events. These systems are critical

for attention, learning, motivation, and for generating adaptive behavioral responses. The dopamine neuromodulatory system is strongly implicated in reinforcement learning and motivational processes. Dopamine-dependent plasticity of cortico-striatal synapses provides a potential mechanism through which actions and stimuli that are associated with unexpected reward are more likely to be repeated or pursued. In general the activity of VTA DA neurons is regulated by inputs from numerous brain regions as well as by local GABAergic neurons, which make up about 30% neurons in the VTA. VTA GABA themselves neurons are also the target of diverse inhibitory inputs, suggesting that both inhibition and disinhibition both play a role in control of VTA dopamine neuron function

*1.2 Models of mesolimbic dopamine function in motivated behavior*

Classical models of learning and motivational processes implicate a role for mesolimbic dopamine in multiple facets of reinforcement learning and motivation. Phasic dopamine neuron activity encodes prediction-error signals which support value-based learning processes (Schultz et al., 1997; O'Doherty et al., 2017). Moreover, mesolimbic dopamine provides an incentive salience signal to modulate the strength and persistence of motivated responding (Berridge and Robinson, 1998; Bromberg-Martin et al., 2010; Niv et al., 2007; Salamone, 1999). Significant effort has been directed towards understanding how the brain supports reinforcement learning and led to the idea that the dopaminergic modulatory input reaching the striatum serves contains a reward prediction error signal or a representation of the computation of the difference between expected and received rewards (Schultz 1997; Doya 2000). Dopamine cell bodies in the ventral tegmental area of the midbrain and their synaptic projections to the nucleus accumbens (NAc) form the mesolimbic pathway. NAc spiny projection neurons integrate dopaminergic signals with cognitive information about environmental stimuli encoded by sensory and limbic inputs (Gruber 2009). This integration plays a key role in driving behaviors such as action selection, motivated approach, and the invigoration of reward-seeking behaviors (Floresco 2015; Castro 2019; Berridge 2016; Kelley 1999). Importantly, anatomically and functionally, there is strong evidence for a dissociation in reward learning and motivation in the VTA dopamine projections to NAc subregions (Di Chiari 2002; Floresco 2015; Saddoris 2013; Saunders 2018).

The prediction error model emerged from the fields of computational and system neuroscience fields. The seminal discovery that individual dopamine neuron activity tracks unexpected rewards and unexpected reward omissions cemented this conceptualization in the field, for better or worse. The hypothesis that dopamine neurons compute and broadcast error signals for prediction remains among the most successful instances of a theoretical model being mapped onto neural substrates. Anatomically, ascending modulatory systems in general and especially the midbrain dopamine system is a good candidate for this hypothesis. A relatively small number of individual dopamine neurons in the ventral tegmental area and substantia nigra innervate large areas of the forebrain and individual dopamine neurons branch extensively to innervate large areas of striatum.

Another long-standing conceptualization of the midbrain dopamine system proposes that dopamine signaling provides the link between the hedonic perception of rewards and the assignment of value to stimuli and actions associated with them. Findings situated in the fields of behavioral neuroscience and psychology led to the incentive salience model of dopamine function. Animals will exert enormous amounts of effort to activate their dopamine system. And dopamine depletion abolishes the drive to seek out rewards but does not change how much animals consume or appear to enjoy them. Thus, this dopamine-dependent value binding process instantiates motivational drive for specific goal-directed actions.

*1.3 Emerging patterns of anatomical and functional heterogeneity in the mesolimbic dopamine system*

When animals behave in complex tasks and naturalistic environments dopamine neurons display heterogeneous and multiplexed responses (Engelhard et al., 2019). In addition to encoding of prediction-error and incentive salience signals, dopamine neurons have been implicated in diverse processes including unconstrained, self-motivated spontaneous behavior (Markowitz et al., 2023), exploratory behavior (Harris et al., 2022), decision-making (O'Doherty et al., 2017; Cox and Witten, 2019; Saddoris et al., 2015), working memory (Adcock et al., 2006; Choi et al., 2020), sleep-wake behaviors (Eban-Rothschild et al., 2016), and social interaction (Gunaydin et al., 2014, Torquet et al., 2018; Solié et al., 2022). Further, dopamine neuron activity can encode movement and accuracy behavioral variables (Engelhard et al., 2019; Bakhurin et al., 2023), track ingestive information (Grove et al., 2022), represent

information about salient and noxious stimuli (Horvitz, 2000; Brischoux et al., 2009; Lammel et al., 2011), and mediate fear association (Jo et al., 2018) and fear extinction (Salinas-Hernández et al., 2018; Cai et al., 2020). Consistent with this pattern of heterogeneity in regulating diverse behavioral functions, VTA dopamine neurons are heterogeneous in their afferent and efferent connectivity and intrinsic neurophysiological properties (Morales and Margolis, 2017; Lammel et al., 2012; Poulin et al., 2018).

But how can we reconcile such heterogeneity within the VTA dopamine system with existing evidence for the RPE and incentive salience models? To better understand how heterogeneity in the mesolimbic dopamine system contributes to motivated behavior, recent studies have emphasized the role of local control of dopamine release via postsynaptic mechanisms in the striatum for the motivational functions of VTA dopamine (Mohebi et al., 2020). Others focused on projection-specific dopamine populations and demonstrated that different regions of the striatum receive distinct dopamine signals (Cox and Witten, 2019; O'Doherty et al., 2004; Balleine et al., 2007; van Elzelingen et al., 2022), and that distinct mesolimbic dopamine pathways encode value and prediction-error information (de Jong et al., 2024). Recent work has identified differential functional roles for dopamine projections to the NAc core and NAc shell in mediating Pavlovian association (Saunders et al., 2018; Heymann et al., 2020) and appetitive and aversive motivation, respectively (Heymann et al., 2020; de Jong et al., 2019). These findings and others have been integrated into an updated model in which, rather than uniformly reflecting homogenous teaching and motivation signals, heterogeneous midbrain dopamine neurons have nuanced roles in reward-related learning and motivated behaviors (Collins and Saunders, 2020). Previous results have established differential patterns of necessity and sufficiency of NAc core and NAc shell dopamine projection populations in reward-related associative learning and motivated responding (Saunders et al., 2018; Heymann et al., 2020). However, the functional role of their endogenous activity dynamics during behavior and intrinsic neurophysiological and circuit properties remains unclear.

In addition to heterogeneous afferent and efferent connectivity, distinct dopamine projection populations have distinct electrophysiological properties (Lammel et al., 2008; Lammel et al., 2011; Poulin et al., 2018; Heymann et al., 2020), and ion channel expression patterns (Juarez et al., 2023; Simon et al., 2023), factors that likely contribute to their distinct functional properties.

The VTA contains multiple types of neurons including dopaminergic, GABAergic, glutamatergic, and combinatorial populations many of which co-release neurotransmitters and neuropeptides (Morales and Margolis, 2017, Nair-Roberts et al., 2008; Parker et al., 2019). Importantly, VTA GABA neurons comprise roughly one-third of all VTA neurons (Nair-Roberts et al., 2008), regulate VTA dopamine neuron excitability through direct inhibition (Jhou et al., 2009; Johnson et al., 1992; Tan et al., 2012; Van Zessen et al., 2012), mediate ongoing motivated behavior (Van Zessen 2012), and modulate VTA dopamine neuron prediction-error responses (Eshel et al., 2015). Although VTA GABA neurons have been implicated in motivated behavior, integrating these findings with an updated understanding of heterogeneous projection-defined dopamine populations has presented a challenge.

## Chapter 2

## Projection-defined VTA dopamine subpopulations and the VTA GABA population contribute to reward association and motivation through distinct mechanisms

### 2.1 Introduction

Theoretical models of learning in the brain propose that the dopaminergic modulatory input reaching the striatum contains a prediction-error signal to support reinforcement learning (Schultz, 1997; Doya 2000). Another foundational model suggests that prediction-error signaling cannot fully account for the function of midbrain dopamine in supporting goal-directed behavior. The incentive-sensitization hypothesis proposes that dopamine signaling in the striatum provides the link between the hedonic valuation of rewards and the assignment of value to stimuli and actions associated with them (Berridge and Robinson, 1998). Thus, prevailing hypotheses suggest that midbrain dopamine plays dual roles in both invigorating ongoing behavior (motivation) and guiding future behavior (learning) (Salamone and Correa, 2012). It has been proposed that dopamine release in the NAc core mediates value-based learning whereas dopamine release in the shell mediates motivational salience (Kelley 1999; Saddoris 2015). Consistent with this hypothesis, our previous results showed that dopamine neurons with projections to NAc core or shell subregions differentially regulate the acquisition, extinction, and maintenance of instrumental responding (Heymann et al., 2020). In addition, recent studies have demonstrated that VTA GABA neurons respond to rewarding and aversive stimuli and constrain the activity of VTA dopamine neurons during motivated behavior (Bouarab et al., 2019; Van Zessen et al., 2012; Eshel et al., 2015). However, few studies have directly compared the endogenous activity dynamics of VTA GABA neurons with VTA dopamine neurons. Our findings extend those of previous studies by revealing how the neural activity dynamics of projection-defined VTA dopamine subpopulations and the VTA GABA inhibitory population contribute to learning and motivation.

### 2.2 Results

#### *2.2.1 VTA subpopulations display distinct response profiles during instrumental conditioning*

Subpopulations of dopamine neurons that differentially regulate reward association and motivation can be isolated in mice using genetic methods (Heymann et al., 2020). Using this approach, we sought to resolve

how and when these VTA dopaminergic subpopulations encode task-related features during an appetitive instrumental conditioning task. To achieve this, we monitored neural activity in subpopulations of dopamine neurons that have been shown to differentially innervate the NAc core (*Crhr1*$_{VTA}$ cells) or NAc shell (*Cck*$_{VTA}$ cells) (Heymann et al., 2020) during a cued reinstatement paradigm (**Figure 1A-1B**; Nugent et al., 2017; Soden et al., 2022). We also monitored neural activity dynamics in VTA dopamine neurons as a whole (DAT$_{VTA}$) and in VTA GABAergic neurons (Vgat$_{VTA}$). *Slc6a3*(DAT)-*Cre, Cck*-Cre, *Crhr1*-Cre, and *Slc32a1*(Vgat)-Cre mice were injected with an AAV expressing a Cre-dependent GCaMP6m in the VTA and implanted with an optical fiber above the VTA for fiber photometry recording of time-varying bulk GCaMP fluorescence (**Figure 1D-1O**; **Figure 6A-6D**). During acquisition sessions, a trial is initiated with an active lever-press (trial-initiation press). After a 3-s delay, the chamber house light is turned off and a compound tone-light stimulus (CS) is presented for 3-s to indicate an upcoming sucrose pellet reward. Following a 12.5-s intertrial interval (ITI) the chamber house light is illuminated indicating the availability of a new trial (**Figure 1B, left**). Lever-presses during the 3-s delay period, 3-s CS-presentation, and 12.5-s ITI are unrewarded. After acquisition mice underwent extinction sessions, during which no CS-presentations or sucrose rewards were delivered (**Figure 1B, middle**). During a single reinstatement session, five non-contingent CS-presentations are delivered during a 10-min pre-session period. Immediately following the pre-session, both levers are extended and responses on the active lever leads to CS-presentation following a 3-s delay but not sucrose reward delivery (**Figure 1B, right**). Mice increased their responding on the active lever during acquisition, decreased responding during extinction, and increased responding during reinstatement (**Figure 1B**).

We next assessed how neural activity in VTA subpopulations correlated with task events (**Figure 1C**). Broadly, the response profile among dopamine populations in response to task-related events was similar but distinct from those observed in Vgat$_{VTA}$ neurons (**Figure 1D-1O**; **Figure 7A-7E**). GCaMP fluorescence was elevated following reward delivery in all four populations, although the latency to peak following reward delivery was greater in the Vgat$_{VTA}$ population (**Figure 1D-1O**; **Figure 7A**). Interestingly, the Vgat$_{VTA}$ populations also displayed prolonged activity after reward delivery (**Figure 1M-1O**). During acquisition, dopamine populations showed increased activity during the trial-initiation press and CS-presentation periods that was significantly different from the pretrial-initiation (Pre-LP) period (**Figure 1D-1L**). In contrast,

GCaMP fluorescence in $Vgat_{VTA}$ neurons during the action and cue periods was not significantly different from the pretrial-initiation period (**Figure 1M-1O**). While both dopamine subpopulations showed phasic responses to these task events, the *Cck*$_{VTA}$ shell-projecting population showed a sustained elevation of GCaMP fluorescence during the full action-cue-outcome period following trial initiation (**Figure 1G-1I**; **Figure 7F**). A comparison between the two dopamine populations revealed a statistically significant difference in the mean response during the action-cue-outcome period across the two populations (**Figure 7F**). In addition, we found *Cck*$_{VTA}$ population activity increased several seconds before mice initiate a trial early in training (**Figure 7G**). By contrast, the *Crhr1*$_{VTA}$ population showed a decrease in activity prior to trial initiation early in training (**Figure 7G**). During extinction, dopamine populations showed modest responses to the lever-press and port-entry bout onsets, while $Vgat_{VTA}$ showed a phasic activation during unrewarded port-entry bout onset (**Figure 1D-1O**). During reinstatement, dopamine populations responded to non-contingent presentations of the cue, but the $Vgat_{VTA}$ population did not (**Figure 1D-1O**). During the contingent phase of reinstatement, dopamine populations showed increased fluorescence to the action and cue responses similar to their response profiles to these periods during acquisition (**Figure 1D-1L**). $Vgat_{VTA}$ neurons showed a sustained decrease in activity during the action and cue periods in contrast to their activity profile during acquisition (**Figure 1M-1O**). During the trial outcome period, the *Cck*$_{VTA}$ population showed a greater latency to decay following omission compared to the *Crhr1*$_{VTA}$ population (**Figure 7H**). Finally, we compared baseline calcium transients during periods of sustained task-related behavioral inactivity during the last extinction session (day 10) across VTA subpopulations (**Figure 6E-6H**). Consistent with the observed pattern of temporal dynamics during behavioral epochs, the number of transients per minute was significantly greater in the *Crhr1*$_{VTA}$ population (**Figure 6E**) whereas the transient width and amplitude were significantly greater in the *Cck*$_{VTA}$ population (**Figure 6G-6H**). These results demonstrate that VTA GABA population activity dynamics are largely distinct from those of VTA dopamine subpopulations. Further, dopamine subpopulations show similar neural activity profiles during an instrumental cued reinstatement task, though they display subtle differences in their temporal dynamics during motivated behavior and at baseline.

*2.2.2 Differential encoding of prediction-error and behavioral variables by VTA subpopulations*

Our results raise an important question: what do VTA subpopulation responses encode? They may uniformly or preferentially reflect prediction-error and task-related action, cue, and outcome events. Prior work has established that lateral VTA dopamine neurons uniformly encode prediction-errors (Eshel et al., 2016), but how this function is organized across projection-specific VTA subpopulations remains unclear. To test this, we recorded GCaMP fluorescence while mice performed a modified version of the acquisition task in which we introduced random unpredictable reward omissions and reduced the overall reward probability following cue presentation to 50% (**Figure 2A-2B**). Mice showed a significantly shorter latency to initiate a new trial following an unrewarded trial compared to rewarded trials (**Figure 2C**). VTA dopamine populations and the $Vgat_{VTA}$ population showed different responses to reward and omission trials with greater activity following sucrose reward (**Figure 2D-2K**). The VTA dopamine populations show an increase in GCaMP fluorescence following rewarded trial port entries and a decrease in fluorescence following unrewarded port entries (**Figure 2D-2I**). However, latency to the minimum GCaMP response following unrewarded trial port entry was significantly shorter in the $Crhr1_{VTA}$ population relative to the $Cck_{VTA}$ population (**Figure 8A-8B**). Additionally, the increase in GCaMP fluorescence following port entry in rewarded trials was greater in the $Cck_{VTA}$ neurons relative to the $Crhr1_{VTA}$ neurons (**Figure 9C-9D**). In contrast, the $Vgat_{VTA}$ population shows an increase in fluorescence following both rewarded and unrewarded trial outcomes (**Figure 2J-2K**), consistent with its role in modulating reward prediction in VTA dopamine neurons (Eshel et al., 2015).

An essential feature of prediction-error encoding by dopamine neurons is the modulation of reward outcome responses by expectation (Schultz et al., 1997). However, whether prediction-error encoding is uniform across dopamine subpopulations is unknown. First, to compare expectation-dependent modulation of reward-outcome responses among VTA subpopulations, we examined how GCaMP fluorescence correlated with rewarded and unrewarded trial outcomes according to the type of outcome on the preceding trial (**Figure 2L-2O**; **Figure 8E-8H**). In $DAT_{VTA}$ and $Crhr1_{VTA}$ populations we observed greater reductions in the GCaMP signal when a reward-omission trial was preceded by a rewarded trial compared to an unrewarded trial (**Figure 2L; Figure 2N**). However, we did not observe a change in reward-omission response between previous trial outcome conditions in $Cck_{VTA}$ neurons (**Figure 2M**). Responses to reward omissions in $Vgat_{VTA}$ neurons were also unaffected by the previous trial outcome (**Figure 2O**). We found

that and *Cck*$_{VTA}$ and Vgat$_{VTA}$ populations showed greater increases in GCaMP fluorescence when a rewarded trial was preceded by an unrewarded trial compared to a rewarded trial (**Figure 7E-7F**). Next, to compare prediction-error encoding in VTA dopamine populations, we fit a linear regression model to predict VTA population trial outcome activity using the current and previous five trial-outcome identities as predictors (**Figure 2P**; adapted from Bayer and Glimcher, 2005). All dopamine populations showed a decay in the influence of previous trial outcomes on their activity (**Figure 2Q-2S**). However, only the DAT$_{VTA}$ and *Crhr1*$_{VTA}$ populations showed the distinctive prediction-error-like combination of a positive modulation by the current trial outcome and a negative modulation by the previous trial outcome (**Figure 2Q; Figure 2S**). This result suggests that the *Cck*$_{VTA}$ population preferentially reflects information about current trials whereas the *Crhr1*$_{VTA}$ neurons are modulated by reward history. This is consistent with previous observations that the *Crhr1*$_{VTA}$ population is preferentially involved in reward-related associative learning processes (Heymann et al., 2020).

To test the idea that VTA subpopulations encode distinct information about actions, stimuli, and rewards, we compared the relative contribution of task events (lever-press, cues, outcomes, port entry) to the neural activity in distinct VTA subpopulations. We focused our analysis on the *Cck*$_{VTA}$ and *Crhr1*$_{VTA}$ dopamine subpopulations and the Vgat$_{VTA}$ GABAergic population. To this end, we fit the GCaMP signal of each mouse with a linear encoding model, in which task event type variables are used to predict neural activity (**Figure 3A-3B**; adapted from Engelhard et al., 2019; Parker et al., 2022). To characterize the relative contribution of different task event types in predicting GCaMP fluorescence, we quantified the decrease in explained variance when a given task predictor variable was excluded from the encoding model (**Figure 3C-3H**). Using this approach, we found that the task variable associated with cues showed the greatest relative contribution to the predicted GCaMP signal in the dopamine subpopulations during the action-cue period (**Figure 3C-3D**). Additionally, the *Crhr1*$_{VTA}$ population showed preferential encoding of the cues compared to the trial initiation press (Trial LP) (**Figure 3D**). By contrast, the *Cck*$_{VTA}$ population did not show a significant difference in the relative encoding of cues and the Trial LP (**Figure 3C**). Extraneous lever-press responses that did not initiate a trial reflected in the active (Active LP) and inactive lever-press (Inactive LP) task variables showed smaller relative contributions to predicted neural activity in both dopamine subpopulations (**Figure 3C-3D**). However, the *Cck*$_{VTA}$ population showed preferential encoding of the Trial

LP relative to the extraneous active lever-press on the same lever (Active LP) whereas the *Crhr1*$_{VTA}$ population did not show a significant difference in the relative encoding of Trial LP and Active LP task variables (**Figure 3C-3D**). By contrast, none of the task predictor variables had a significantly different relative contribution to neural activity during the action-cue period in the Vgat$_{VTA}$ population (**Figure 3E**). During the trial-outcome period, reward contributed most strongly to the predicted response followed by reward retrieval in both dopamine subpopulations (**Figure 3F-3G**). However, the Vgat$_{VTA}$ population most strongly encoded reward retrieval, followed by reward (**Figure 3H**). Thus, *Cck*$_{VTA}$ and *Crhr1*$_{VTA}$ dopamine subpopulations are distinct in their representation of reward-seeking actions and reward-predictive stimuli but relatively uniform in their encoding of reward outcomes. Further, as a population Vgat$_{VTA}$ neurons do not encode unique information about reward-predictive actions or cue information but strongly encode information about reward receipt. These results indicate that *Cck*$_{VTA}$, *Crhr1*$_{VTA}$, and Vgat$_{VTA}$ dopamine subpopulations encode distinct behavioral variables across action-cue and trial-outcome epochs.

*2.2.3 VTA populations differentially encode reward anticipation*

The above results demonstrate how VTA subpopulations respond when rewards are readily attainable and the response requirement is fixed. However, VTA dopamine neuron activity is correlated with effort exertion and dopamine release in the NAc is thought to invigorate ongoing motivated behaviors (Salamone and Correa, 2012; Gan et al., 2010). How dynamic changes in effort and reward availability are represented across VTA dopamine subpopulations and the VTA GABA population remains unknown. To address this question, we recorded GCaMP fluorescence while mice underwent a progressive ratio test, in which the number of lever-presses required to earn a reward is increased systematically following each reward throughout the session (**Figure 4A**). This task also measures the breakpoint, or the maximum level of effort an animal is willing to exert before they stop responding (Hodos, 1961). Mice tracked this increasing response requirement, reflected in the high number of cumulative lever-press responses across mice (**Figure 4B-4C**). The increasing response requirement allowed us to measure responses reflective of relative levels of effort exertion and reward anticipation across decreasing periods of reward availability.

Across the entire session, we found that activity in both dopamine subpopulations is transiently increased at the onset of bouts of lever-pressing (**Figure 4D-4G**). In addition, the *Cck*$_{VTA}$ population showed a sustained elevation in activity during the 10-s following lever-press bout onset (**Figure 4D-4E**). By contrast,

the $Vgat_{VTA}$ population was not engaged at lever-press bout onset (**Figure 4H-4I**). During unrewarded port entry bout onset all VTA populations showed a small increase in activity prior to bout onset followed by a decrease to baseline during the duration of the bout (**Figure 4D-4I**). During rewarded port entries activity in both dopamine subpopulations ramped up prior to reward retrieval and shows sustained activity during reward consumption (**Figure 4D-4G**). $Vgat_{VTA}$ neurons showed a relatively modest increase in activity prior to reward retrieval, in contrast to VTA dopamine populations (**Figure 4H-4I**).

To determine how the response profiles of VTA subpopulations evolve across increasing effort requirements and decreasing reward availability, we examined neural activity as a function of the breakpoint of each mouse. We found that *Crhr1*$_{VTA}$ and *Cck*$_{VTA}$ populations showed distinct activity profiles in response to decreasing reward availability. *Cck*$_{VTA}$ population activity at lever-press bout onset was initially high and sustained during the entire bout earlier in the session with lower lever-press response requirements (**Figure 4J**). However, *Cck*$_{VTA}$ population activity during lever-press bout onset was decreased later in the session as rewards required more effort exertion to obtain them (**Figure 4J**). By contrast, the *Crhr1*$_{VTA}$ population responded similarly at lever-press bout onset regardless of response requirements (**Figure 4K**). Thus, the *Cck*$_{VTA}$ population is preferentially engaged with sustained activity during ongoing motivated responding when rewards are more readily attainable. Further, we found that decreased reward availability was associated with less activity in the *Cck*$_{VTA}$ population during lever-press bouts across the entire session but not in the *Crhr1*$_{VTA}$ or $Vgat_{VTA}$ population (**Figure 4M-4O**). A statistical comparison of the correlation between percent of breakpoint and GCaMP response during LP bout onset across mice revealed a significant difference between the *Cck*$_{VTA}$ and *Crhr1*$_{VTA}$ populations (**Figure 4P**). Taken together, these results suggest that *Cck*$_{VTA}$ dopamine population activity reflects a reward anticipation signal during goal-directed actions that tracks reward availability, whereas the *Crhr1*$_{VTA}$ dopamine population does not encode this type of motivational information. This is consistent with the previous observation that the *Cck*$_{VTA}$ population is preferentially involved in reward-driven motivated responding (Heymann et al., 2020).

*2.2.4 Differential contribution of dopamine subpopulations to cued reinstatement of reward-seeking behavior*

*Crhr1*$_{VTA}$ and *Cck*$_{VTA}$ dopamine subpopulations differentially regulate the acquisition and extinction of an instrumental response (Heymann et al., 2020). Further, it has been shown that phasic activation of VTA

dopamine neurons is sufficient to reactivate a previously extinguished instrumental behavior in the absence of reward-predictive stimuli (Tsai et al., 2009; Adamantidis et al., 2011; Witten et al., 2011). However, how distinct VTA dopamine subpopulations mediate the reactivation of cue-driven instrumental responding following extinction remains unclear. To determine if reward-predictive, cue-related neural activity in dopamine subpopulations is sufficient to modulate the reactivation of cue-driven instrumental responding, we photostimulated both populations during CS-presentation throughout the reinstatement session. *Cck*-Cre, and *Crhr1*-Cre mice were injected with an AAV expressing a Cre-dependent ChR2 or GFP in the VTA and implanted with an optical fiber above the VTA (**Figure 5A**; **Figure 9A-9B**). Mice were trained on the acquisition and extinction phases of the cued reinstatement task without photostimulation (**Figure 5B-5C**; **Figure 9C-9D**). Extinction-resistant mice were excluded from the analysis which resulted in the exclusion of 1 of 17 controls, 1 of 22 *Crhr1*-Cre, and 2 of 18 *Cck-Cre* mice. To rule out the possible confound of reinforcement of lever-pressing by photostimulation in the absence of CS-presentation, we photostimulated each population 3-s (20 Hz, 5-ms pulse width, 3-s duration) following an active lever-press during an additional extinction session (Stim) prior to the reinstatement session (Stim + CS) (**Figure 5B**). Photostimulation of either population 3-s following an active lever-press in the absence of CS-presentation did not affect operant responding (**Figure 5D**). We next asked whether photostimulation of these neurons during CS-presentation is sufficient to alter reinstatement behavior (Stim + CS) (**Figure 5B**). CS-presentation paired with photostimulation of $Crhr1_{VTA}$ but not $Cck_{VTA}$ neurons during cued reinstatement significantly increased the number of active lever-presses during the entire session (**Figure 5D-5E**) but did not alter the total number of trials completed (**Figure 5F**) or the number of inactive lever-presses (**Figure 9E**).

To determine if the activity observed in dopamine subpopulations during CS-presentation causally contributes to cued reinstatement behavior, we photoinhibited both populations during CS-presentation throughout the reinstatement session (**Figure 5H**). *Cck*-Cre and *Crhr1*-Cre mice were injected bilaterally with an AAV carrying Cre-dependent inhibitory JAWS or GFP in the VTA and implanted with bilateral optical fibers above the VTA (**Figure 5G**; **Figure 9F-9G**). Mice performed the acquisition and extinction phases of the cued reinstatement task without photoinhibition (**Figure 5H-5I**; **Figure 9H-9J**). No mice met exclusion criteria for extinction resistance. VTA subpopulations were photoinhibited 3-s (2-s constant square pulse

terminated with a 1-s linear ramp-down to avoid rebound excitation, Jo et al., 2018) during the CS-presentation throughout the cued reinstatement session (Light + CS) (**Figure 5H**). Photoinhibition of *Crhr1*$_{VTA}$ but not *Cck*$_{VTA}$ neurons reduced the total number of lever-presses in the reinstatement session (Light + CS) (**Figure 5J-5K**) and reduced the total number of trials completed (**Figure 5L**). Photoinhibition did not alter the number of inactive lever-presses (**Figure 9J**). Taken together, these findings indicate that the contribution of *Crhr1*$_{VTA}$ neurons to cued reinstatement is distinct from that of *Cck*$_{VTA}$ neurons.

**2.3 Discussion**

Here we tested and extended the hypothesis that reward-related associative learning is mediated by *Crhr1*$_{VTA}$ neurons whereas *Cck*$_{VTA}$ dopamine neurons are more involved in ongoing motivated responding. First, we found that the response profiles of projection-defined dopamine populations are broadly similar during a cued reinstatement task. This is consistent with existing evidence that dopamine neurons respond relatively uniformly (similar response profile to action, cue, and outcomes) during simple instrumental conditioning tasks (Engelhard et al.; 2019, Heymann et al., 2020; Schultz, 1998), although the temporal resolution of fiber photometry recording of GCaMP6m fluorescence may be insufficient for detecting task-relevant neural activity dynamics on subsecond timescales. Our recordings revealed patterns of brief, time-locked increases in activity in VTA dopamine populations during action, cue, and outcome periods. By contrast, activity in all VTA populations was sustained long after reward delivery. We additionally observed patterns of sustained activity on long timescales (10-s) prior to reward delivery preferentially in the *Cck*$_{VTA}$ population. Gradual increases in dopamine neuron activity and dopamine release as animals perform goal-directed behaviors and approach rewards has been reported (Hamid et al., 2015; Wassum et al., 2012; Howe et al., 2013; Collins and Saunders, 2020; Farrell et al., 2022). Whether this pattern of activity reflects reward expectation, prediction-errors, sustained effort, motivational engagement, or a combination remains unclear. The sustained increase in activity we observed in the *Cck*$_{VTA}$ population during the action-cue period prior to reward across acquisition sessions could reflect a reward anticipation signal or an overall increased level of motivational engagement at trial onset.

When reward probability or reward effort were dynamically varied during learning and motivation tasks we found heterogeneous responses with non-uniform encoding of prediction-error, behavioral variables, and reward anticipation across NAc core and NAc shell-projecting subpopulations. We found a striking

difference in how VTA dopamine populations encode prediction-error and action-cue behavioral variables. During a random reward-omission instrumental task, *Crhr1*$_{VTA}$ activity reflected a prediction-error-like signal, while *Cck*$_{VTA}$ activity reflected a salience signal. Further, *Crhr1*$_{VTA}$ neurons preferentially encoded cues whereas the *Cck*$_{VTA}$ population similarly encoded both actions and cues. The observed positive modulation of dopamine neuron activity by current trial outcome and negative modulation by previous trial outcome support the notion that *Crhr1*$_{VTA}$ neurons are more involved in prediction-error encoding compared to *Cck*$_{VTA}$ neurons. By contrast, the *Cck*$_{VTA}$ population preferentially encoded the trial initiation lever-press action compared to the non-trial active lever-press action, whereas the *Crhr1*$_{VTA}$ population similarly encoded both the trial initiation action and non-trial action. Taken together, these results suggests that *Crhr1*$_{VTA}$ neurons strongly encode reward-associated stimuli and integrate predictive information over time to drive future behavior, whereas *Cck*$_{VTA}$ neurons strongly encode goal-directed actions and provide a salience signal to drive ongoing behavior.

We found that the VTA dopamine populations have striking differences in how they respond to increasing levels of effort during bouts of lever-pressing throughout a progressive ratio task. Previous studies showed that VTA dopamine activity is negatively correlated with effort and reward attainability (Gan et al., 2010; Hamid et al., 2015); however, whether this effect is uniform across distinct dopamine subpopulations remains unclear. Our observation that *Cck*$_{VTA}$ neurons display sustained elevation in activity during lever-pressing early in progressive ratio sequences when rewards are more attainable but not later suggests that sustained activity in this population, but not in *Crhr1*$_{VTA}$ neurons, reflects reward anticipation during ongoing motivated behavior. Together, these findings suggest that prediction-error-encoding, action-cue encoding, and reward-anticipation encoding involve dopamine projections to distinct subregions of the NAc. In contrast to previous studies (Mohebi et al., 2019), our results suggest that sustained cell body activity in a distinct subpopulation of VTA dopamine neurons during behavior contributes to ongoing motivated responding. Further, consistent with our observed pattern of functional heterogeneity across VTA dopamine subpopulations, it was recently demonstrated that dopamine neurons in the medial VTA display sustained activity patterns during behavior and encode behavioral state, whereas anatomically distinct lateral VTA dopamine neurons display transient activity and encode behavioral rate-of-change (de Jong et al., 2024).

In addition to examining how projection-defined dopamine populations contribute to reward association and motivation, we further sought to directly compare the endogenous activity dynamics of VTA dopaminergic and GABAergic populations. The most prominent difference in activity dynamics among VTA subpopulations was found in the VTA GABA neurons, which encoded reward retrieval much more strongly than VTA dopamine populations. While dopamine populations showed transient and sustained responses during instrumental responses and cues, the $Vgat_{VTA}$ population responded selectively during reward outcome periods. When reward was available, $Vgat_{VTA}$ responses were sustained throughout reward consumption. Unrewarded port entries, however, evoked smaller, brief increases in $Vgat_{VTA}$ activity. Further, the $Vgat_{VTA}$ population preferentially encoded rewarded port entry compared to unrewarded port entry but showed no preferential encoding of behavioral variables during the action-cue period. This reward outcome-dependent difference in activity is consistent with findings that $Vgat_{VTA}$ neurons causally contribute to reward expectation-driven decreases in VTA dopamine neuron activity (Eshel et al., 2015). Taken together, these results suggest that VTA GABA neurons reflect reward outcome information and may suppress VTA dopamine activity during reward consumption. Given the observed distinct activity dynamics among VTA dopamine populations during periods of high VTA GABA activity, VTA dopamine subpopulations likely have distinct connectivity patterns with VTA GABA neurons and may receive inhibitory input from distinct subpopulations of VTA GABA neurons.

Our previous work showed that *Crhr1*$_{VTA}$ and *Cck*$_{VTA}$ neurons differentially facilitate the acquisition and extinction of a goal-directed instrumental response (Heymann et al., 2020). Additionally, recent work showed that NAc core and NAc shell-projecting dopamine populations differentially contribute to Pavlovian cue conditioning (Saunders et al., 2018). Given this, we hypothesized that these populations differentially contribute to cued reinstatement. In contrast to the similarity in activity dynamics observed during cued reinstatement across dopamine subpopulations, their causal roles in reinstatement behavior were distinctive. We found that the effect of cue-paired activation on cued reinstatement behavior depended on which dopamine subpopulation was targeted. Consistent with the idea that reward-predictive cues drive motivated behavior through *Crhr1*$_{VTA}$ neurons, activation of *Crhr1*$_{VTA}$ neurons during cue presentations robustly increased cued reinstatement. Given the observed activity dynamics of *Crhr1*$_{VTA}$ and *Cck*$_{VTA}$ neurons during cued reinstatement, we hypothesized that either or both of these populations contribute

causally to cued reinstatement behavior. Indeed, we found that cue-paired inhibition of *Crhr1*$_{VTA}$ neurons reduced cued reinstatement behavior. In contrast, inhibition of *Cck*$_{VTA}$ neurons did not affect cued reinstatement. While photostimulation generated robust effects on behavior, photoinhibition had a more modest impact on reinstatement. This could be due to incomplete inhibition, but it is likely that local control of dopamine release and other inputs to the NAc including the prefrontal cortex, thalamus, hippocampus, and amygdala contribute to cued reinstatement. Additionally, a modest reduction in reinstatement could reflect a floor effect since mice continue to respond habitually following extinction. Further, modifying the timing of optical manipulation relative to action, cue, and reward could reveal more nuanced contributions of dopamine subpopulations to cued reinstatement.

Together, these results support the idea that similar patterns of dopamine neuron activity contribute to distinct aspects of behavior depending on NAc subregion target. One possible interpretation of these results is that NAc core-projecting *Crhr1*$_{VTA}$ neurons are selectively involved in encoding the motivational value of reward-predictive stimuli to drive future behavior whereas the NAc shell-projecting *Cck*$_{VTA}$ neurons are preferentially involved in encoding goal-directed actions and reward anticipation during ongoing motivated behavior (Kelley, 1999; Saunders et al., 2018).

### 2.4 Methods

#### Surgery

Mice (6-8 weeks) were anesthetized with isoflurane (1.5 – 4%) and head-fixed for stereotaxic (David Kopf Instruments) survival surgery. Stereotactic coordinates were standardized relative to Bregma and Lambda distance and an injection syringe was used to inject 0.5 µL of virus at a rate of 0.25 µL/min. Mice recovered from surgery for at least two weeks prior to behavioral testing.

#### *Fiber photometry*

For fiber photometry behavior experiments, 0.5 µL of AAV1-DIO-GCaMP6m was injected unilaterally into the VTA (A/P: -3.25 mm, M/L: -0.5 mm, D/V: -4.5 mm). Following the virus injection, a fiber optic cannula (400 µm) was implanted 0.5 mm above the VTA.

#### *Optogenetics*

For photostimulation behavior experiments, 0.5 µL of AAV1-DIO-ChR2-YFP was injected unilaterally into the VTA (A/P: -3.25 mm, M/L: -0.5 mm, D/V: -4.5 mm). Following the virus injection, a fiber optic cannula (200 µm) was implanted 0.5 mm above the VTA.

For photoinhibition behavior experiments, 0.5 µL of AAV1-DIO-JAWS-GFP was injected bilaterally into the VTA (A/P: -3.25 mm, M/L: ±0.5 mm, D/V: -4.5 mm). Following the virus injection, fiber optic cannulae (200 µm) were implanted 0.5 mm above the VTA bilaterally. The fiber optic cannula was implanted at an angle of 10 degrees on one side.

**Fiber photometry**

GCaMP6m fluorescence was recorded through an implanted optic fiber connected to a patch cord (Doric Lenses) while mice performed behavioral tasks. An LED driver (Doric Lenses) was used to control two LEDs for excitation of GCaMP6m. A 465-nm LED (light intensity: 30-40 µW, sinusoidal frequency modulation: 531 Hz) was used to excite GCaMP6m for calcium-dependent fluorescence. A 405-nm LED (light intensity: 30-40 µW, sinusoidal frequency modulation: 211 Hz) was used to excite GCaMP6m for calcium-independent fluorescence. Light intensity was measured at the optic fiber tip. GCaMP6m fluorescence was collected through the same optic fiber using a photoreceiver (Doric Lenses) and recorded using a Tucker Davis Technologies (TDT) real-time processor (RZ5 BioAmp) at 1017.25 Hz sampling frequency. Task event timestamps were simultaneously registered as TTL pulses by the MedAssociates system and synchronously delivered to the TDT system through a custom interface.

**Fiber photometry preprocessing**

The 405-nm and 465-nm signals were demodulated and downsampled to 50 Hz using a moving average. The downsampled 405-nm control signal was fit to the 465-nm GCaMP6m signal using the ‘np.polyfit’ function in Python with a degree of 1 to obtain a fitted control signal. The fitted control signal was subtracted from the downsampled 465-nm GCaMP6m signal to correct for calcium-independent fluorescence changes. Then, an exponential curve was fit to the corrected 465-nm signal and subtracted to correct for slow baseline drift due to photobleaching. The baseline-corrected 465-nm GCaMP6m signal for the entire recording session ($\Delta F/F$) was z-scored relative to the mean and standard deviation of the entire session trace to allow for comparison across individual recording sessions and individual mice. The session z-score

was defined as ΔF/F(t) - mean(ΔF/F(t)) / std(ΔF/F(t)). The preprocessed photometry signal was aligned to task events and mean z-score ± SEM was calculated for behavioral epochs of interest. Lever pressing and port entry bouts were classified in either 10-s or 30-s windows aligned to session event times and the first event time per bout (bout onset) was aligned to the photometry signal. Baseline calcium transient analysis was restricted to time periods in which no behavioral event timestamps (lever-press, port entry) were recorded for at least 60-s during the final extinction session of the cued reinstatement task. This resulted in ~20-30-min of baseline recording time per mouse. Transients were identified using the Python 'scipy.signal.find_peaks' function.

**Optogenetics**

For behavioral experiments with optogenetics, mice underwent the pretraining, acquisition, and extinction phases of the cued reinstatement task without laser stimulation. For photostimulation experiments, mice received blue light (3-s, 20 Hz, 5-ms pulse width, ~10 mW light power) unilaterally in the VTA 3-s following active lever press throughout the control stimulation session following the last extinction session. Throughout the cued reinstatement session, mice received blue light (3-s, 20 Hz, 5-ms pulse width, ~10 mW) unilaterally in the VTA during cue presentation. For photoinhibition experiments, mice received red light (2-s constant square pulse terminated with a 1-s linear ramp-down, ~5-10 mW light power) unilaterally in the VTA during cue presentation throughout the cued reinstatement session.

For photostimulation of VTA GABAergic neurons in the VTA, mice were placed in an operant box and received red light (1-s or 3-s, 5 - 40 Hz, 5-ms pulse width, ~10 mW light power) every 60-s for 80 trials across two sessions. Red light was delivered through the same optic fiber used for fiber photometry recording.

For stimulation of LH or Nac medial shell GABAergic neurons, mice received red light (1-s or 3-s, 5 - 40 Hz, 5-ms pulse width, ~10 mW light power) every 60-s for 80 trials across two sessions. Red light was delivered through an optic fiber above the LH or Nac medial shell.

**Linear Encoding Model**

To quantify the relative contribution of task variables to neural activity, we used a linear encoding model (adapted from Engelhard et al., 2019 and Parker et al., 2022). Multiple linear regression was used to predict

the photometry signal for a given mouse using task behavioral variables as predictors. The task predictor set consisted of a matrix of 10 behavior event types (event times of trial initiation lever press, non-trial active lever press, non-trial inactive lever press, cue onset, reward outcome, omission outcome, rewarded port entry, unrewarded port entry, non-trial port entry, trial-reset house light cue). Each event type time series was convolved with a set of cubic splines that span several seconds after the event and three seconds before an action event type. A longer set of cubic splines was used for rewarded and unrewarded trial outcome events to reflect the longer trial outcome neural responses. The encoding model is expressed as $y = \beta X + \varepsilon$, where y is the GCaMP6m fluorescence for a given mouse during the random reward-omission task, X is the set of event predictors generated from the convolution of event times with the cubic spline set, and β is the set of weights learned from the regression.

We first fit the full version of the encoding model using the 'fitglm' function in MATLAB with threefold cross-validation to generate $R^2$ for the full model. We then compared the model fit when each of the task predictors were removed to that of the full model to quantify the relative contribution of individual behavioral variables. An individual task predictor contribution was defined as the reduction in explained variance $\Delta R^2$ when that task predictor was removed from the model (1 - $R^2$ partial/ $R^2$ full). The relative contribution of an individual task predictor was defined as a fraction of the predictor contribution over the full model predictor contributions.

**Reward Outcome History RPE Analysis**

We used linear regression to predict neural activity following trial outcome using trial outcome information from the current and five previous trials (adapted from Bayer and Glimcher, 2005). The z-scored GCaMP6m signal during a 2-s time bin prior to trial initiation was subtracted from the z-scored GCaMP6m signal from 0 to 20-s following trial outcome for each trial during the random reward-omission task. Current and previous trial outcomes were labeled 0 for omission and 1 for reward. Multiple linear regression was used to generate weights corresponding to the contribution of each of the current and five previous trial outcomes to the neural activity following the current trial outcome. The model is expressed as $y(t) = \beta_0 + \beta_1 T_{out}(t) + \beta_2 T_{out}(t-1) + \ldots + \beta_6 T_{out}(t-5)$, where y(t) is the mean z-scored GCaMP6m signal from 0 to 20-s on trial t, $T_{out}(t)$ is the trial outcome, and $\beta_i$ is the regression coefficient for trial $T_{out}(t-n)$. The regression coefficients for each trial

lag were generated with the ‘OLS’ function from the ‘linear_model’ module in the Python ‘statsmodels’ package.

### 2.5 Quantification and statistical analysis

All data are expressed as mean ± SEM. Statistical analyses were performed using GraphPad Prism, Python, and MATLAB. All statistical tests were two-tailed. Sample sizes were not predetermined using statistical methods. For data from two groups, the paired *t*-test, unpaired *t*-test, and Mann-Whitney *U* test were used where appropriate. For data from three or more groups, one-way ANOVA and one-way repeated-measures ANOVA followed by multiple-comparisons tests (Tukey's multiple comparisons test, Bonferroni's multiple comparisons test, two-stage linear step-up procedure of Bejamini, Krieger and Yekutieli) were used to determine any statistically significant differences between groups. For data from three or more groups and across multiple conditions, two-way ANOVA and two-way repeated-measures ANOVA followed by multiple-comparisons tests (Šídák's multiple comparisons test, two-stage linear step-up procedure of Bejamini, Krieger and Yekutieli) were used where appropriate. For correlation analysis, the Pearson correlation coefficient was used. For all tests, a significance threshold of 0.05 was used. See supplementary Table 1 for detailed statistical results.

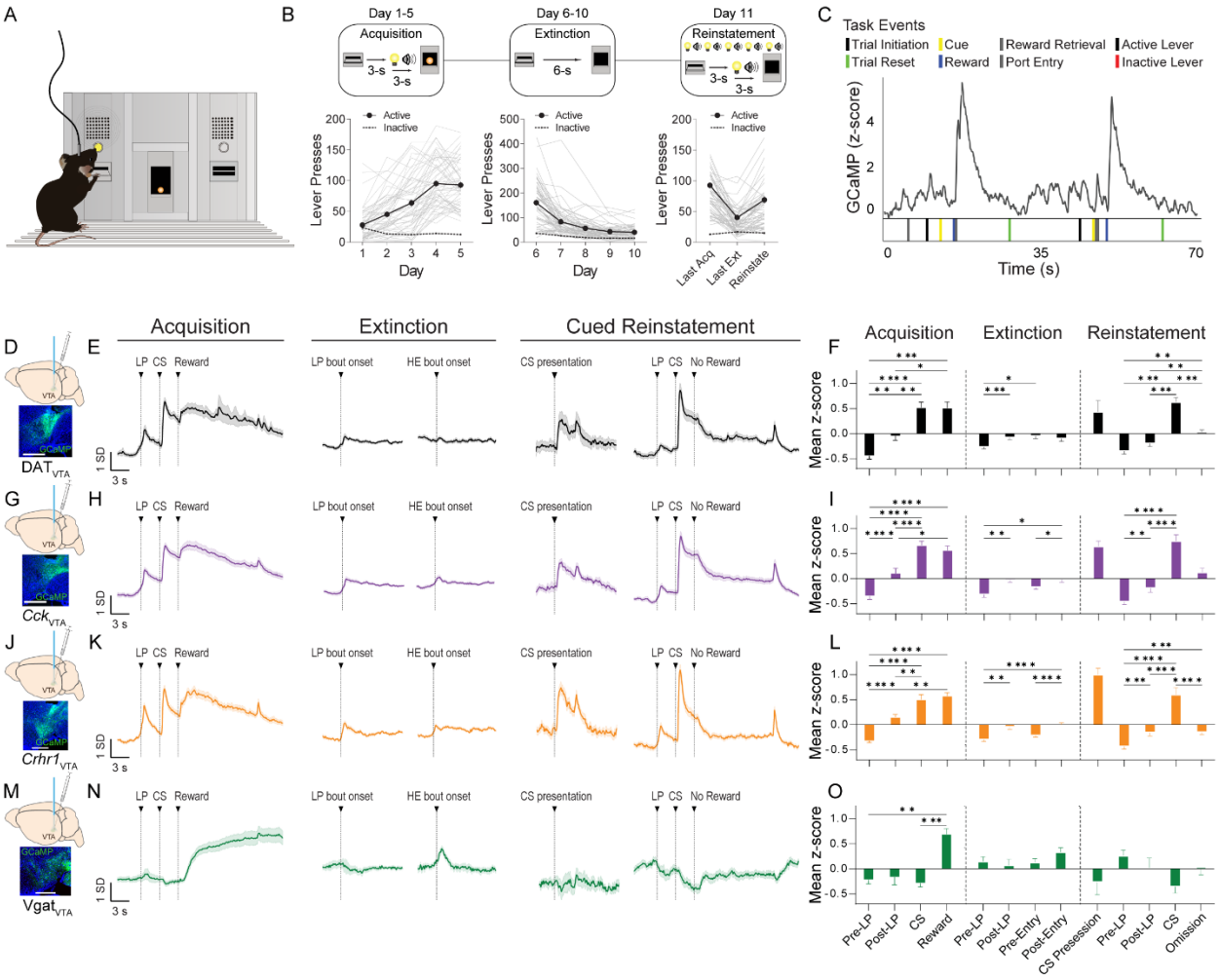


**Figure 1. Fiber photometry recordings of VTA subpopulations while mice perform a cued reinstatement task**

(A) Schematic of a fiber photometry recording session during the cued reinstatement instrumental conditioning task.
(B) Schematic depicting training phases and behavioral performance of mice on acquisition, extinction, and reinstatement task phases (n = 57 mice; solid lines indicate mean across mice and gray lines indicate individual replicates).
(C) Example recording trace during acquisition task showing GCaMP fluorescence (top) aligned to event timestamps (bottom).
(D) Schematic of viral injection and optic fiber implant and example histology image from the VTA showing staining for GCaMP6 (green) in the DAT$_{VTA}$ group. Scale bar: 500 µm.
(E) Z-scored GCaMP fluorescence from DAT$_{VTA}$ population recordings aligned to task events during acquisition, extinction, and reinstatement (n = 9 mice, 63 sessions). Data from all trials during the first, third, and last acquisition and extinction training sessions and from all trials during the reinstatement session.
(F) Average z-scored GCaMP fluorescence from DAT$_{VTA}$ population recordings during LP, CS, reward, port entry, and omission periods (n = 9 mice, 63 sessions, bars and error bars indicate mean ± SEM across mice, see Supplementary Table 1 for statistical values).
(G) Same as in (D) but for *Cck*$_{VTA}$ population recordings. Scale bar: 500 µm.
(H) Same as in (E) but for *Cck*$_{VTA}$ population recordings (n = 16 mice, 112 sessions).
(I) Same as in (F) but for *Cck*$_{VTA}$ population recordings (n = 16 mice, 112 sessions).

(J) Same as in (D) but for *Crhr1*$_{VTA}$ population recordings. Scale bar: 500 µm.
(K) Same as in (E) but for *Crhr1*$_{VTA}$ population recordings (n = 13 mice, 91 sessions).
(L) Same as in (F) but for *Crhr1*$_{VTA}$ population recordings (n = 13 mice, 91 sessions).
(M) Same as in (D) but for Vgat$_{VTA}$ population recordings. Scale bar: 500 µm.
(N) Same as in (E) but for Vgat$_{VTA}$ population recordings (n = 8 mice, 56 sessions).
(O) Same as in (F) but for Vgat$_{VTA}$ population recordings (n = 8 mice, 56 sessions).

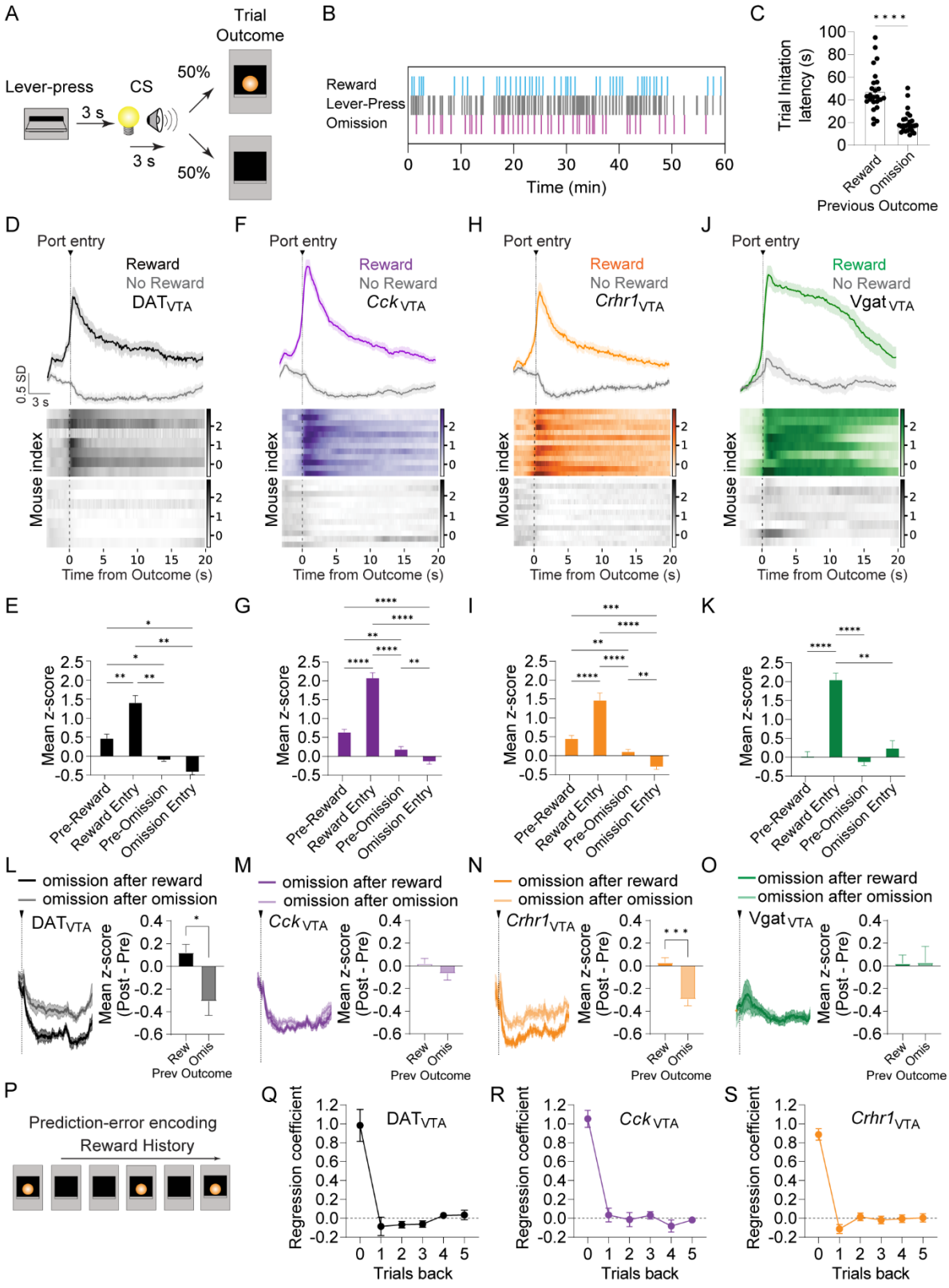


**Figure 2. Time-locked activation of VTA subpopulations during random reward omission**

(A) Schematic of the random reward-omission task. An active lever-press triggered a 6-s delay-cue period and the probability of reward was 50%.
(B) Example behavioral session showing lever-press, reward, and omission times.
(C) Trial initiation latency following the intertrial interval period (n = 25 mice, bars and error bars indicate mean ± SEM across mice).
(D) Z-scored GCaMP fluorescence and heatmaps aligned to reward (color) or reward omission (gray) task events from the $DAT_{VTA}$ group (n = 7 mice).
(E) Average z-scored GCaMP fluorescence during reward, omission, and port entry periods for the $DAT_{VTA}$ (n = 7 mice) group.
(F) Same as in (D) but for the *Cck*$_{VTA}$ (n = 12 mice) group.
(G) Same as in (E) but for the *Cck*$_{VTA}$ (n = 12 mice) group.
(H) Same as in (D) but for the *Crhr1*$_{VTA}$ (n = 13 mice) group.
(I) Same as in (E) but for the *Crhr1*$_{VTA}$ (n = 13 mice) group.
(J) Same as in (D) but for the $Vgat_{VTA}$ (n = 8 mice) group.
(K) Same as in (E) but for the $Vgat_{VTA}$ (n = 8 mice) group.
(L) Z-scored GCaMP fluorescence (left) and average z-scored GCaMP fluorescence (right) during reward omission periods shaded according to previous trial outcome type for the $DAT_{VTA}$ group (n = 7 mice).
(M) Same as in (L) but for the *Cck*$_{VTA}$ group (n = 12 mice).
(N) Same as in (L) but for the *Crhr1*$_{VTA}$ group (n = 13 mice).
(O) Same as in (L) but for the $Vgat_{VTA}$ group (n = 8 mice).
(P) Schematic of outcome history regression model approach. The current previous five trial outcomes were used with a multiple linear regression to predict the GCaMP signal during the current trial outcome.
(Q) Average regression coefficients across mice for the outcome history linear regression for $DAT_{VTA}$ (n = 7 mice), *Cck*$_{VTA}$ neurons (left) (n = 12 mice) and *Crhr1*$_{VTA}$ neurons (right) (n = 13 mice, see Supplementary Table 1 for statistical values).
(R) Same as in (Q) but for the *Cck*$_{VTA}$ group (n = 12 mice).
(S) Same as in (Q) but for the *Crhr1*$_{VTA}$ group (n = 13 mice).

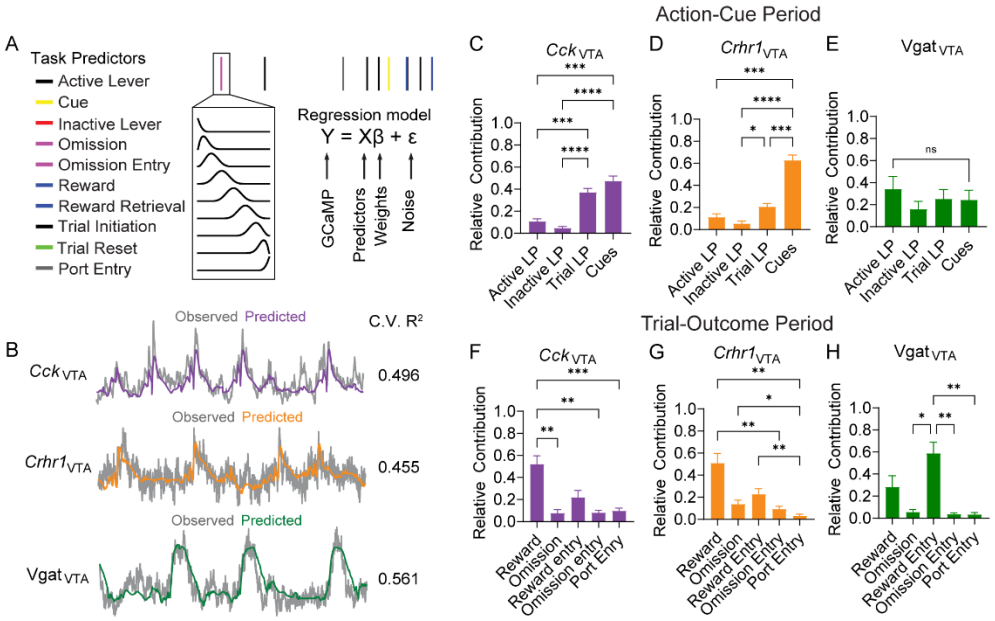


**Figure 3. VTA subpopulations differentially encode task relevant behavioral variables during random reward-omission**

(A) Schematic of the linear encoding model. Task event timestamps were convolved with a set of cubic splines to generate a predictor set of ten behavior event types. The GCaMP signal was predicted based on task events.

(B) Example observed (gray) and predicted (color) GCaMP traces from *Cck*$_{VTA}$ (top), *Crhr1*$_{VTA}$ (middle), and Vgat$_{VTA}$ (bottom) groups.

(C) Relative contribution of each task event type to the explained variance of the GCaMP signal during the action-cue period, averaged across mice for the *Cck*$_{VTA}$ group (n = 12 mice) (see Supplementary Table 1 for statistical values).

(D) Same as in (C) but for the *Crhr1*$_{VTA}$ group (n = 11 mice).

(E) Same as in (C) but for the Vgat$_{VTA}$ group (n = 8 mice).

(F) Relative contribution of each task event type to the explained variance of the GCaMP signal during the trial outcome period, averaged across mice for the *Cck*$_{VTA}$ group (n = 12 mice).

(G) Same as in (F) but for the *Crhr1*$_{VTA}$ group (n = 11 mice).

(H) Same as in (F) but for the Vgat$_{VTA}$ group (n = 8 mice).

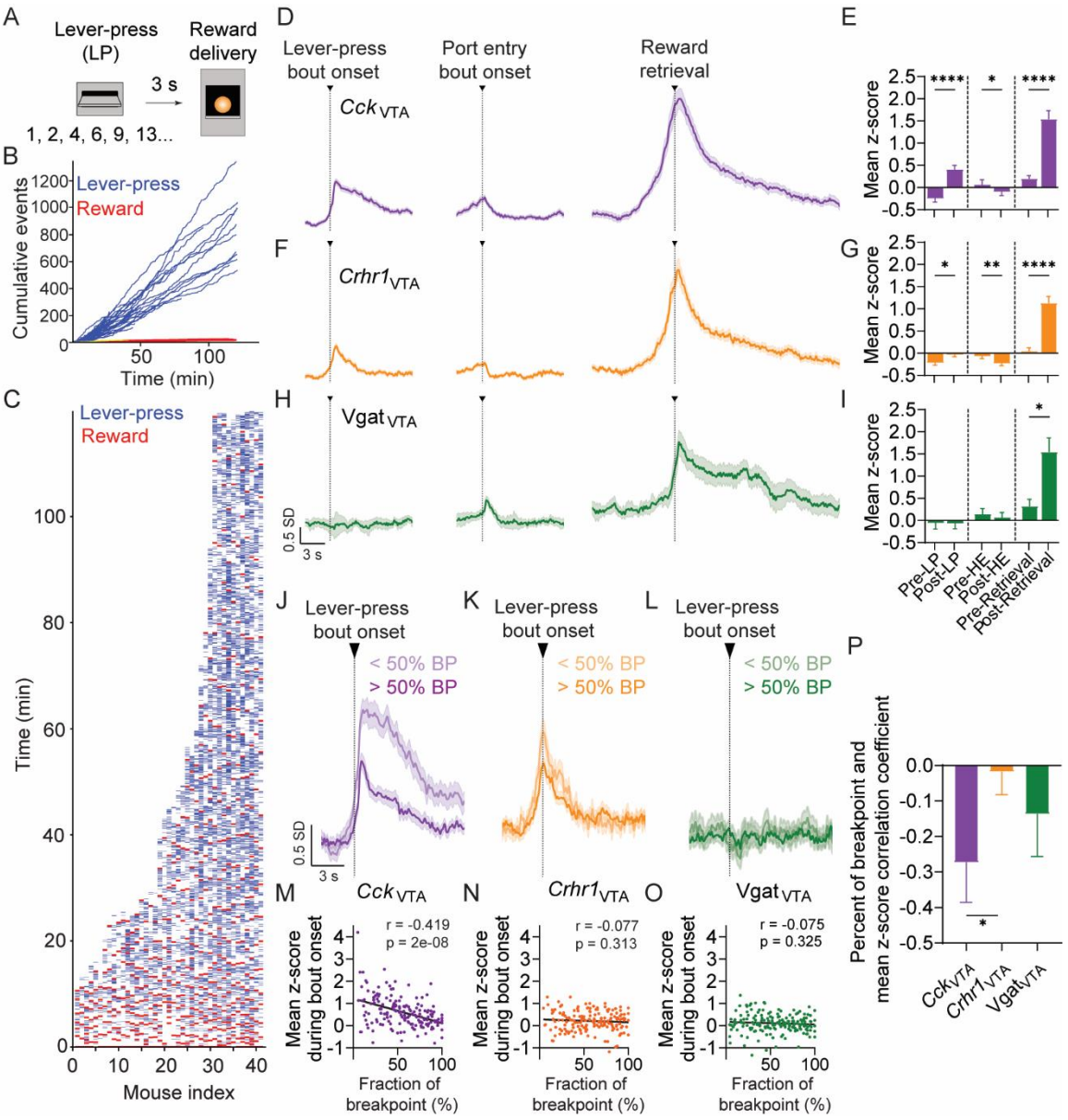


**Figure 4. VTA subpopulations differentially encode reward anticipation during progressive ratio**

(A) Schematic of the progressive ratio (PR) task. The number of lever-presses required for a reward increased systematically following each reward throughout the session.

(B) Cumulative lever-presses (blue) and rewards (red) during PR sessions. Lines indicate individual mice (n = 42 mice).

(C) Lever-press (blue) and reward (red) event times shown for all sessions (n = 42 mice).

(D) Z-scored GCaMP fluorescence from photometry recordings aligned to lever-press bout onset, port entry bout onset, and reward retrieval for *Cck*$_{VTA}$ group (n = 17 mice).

(E) Average z-scored GCaMP fluorescence during lever-press bout onset, port entry bout onset, and reward retrieval periods for the *Cck*$_{VTA}$ group (n = 17 mice). Bars and error bars indicate mean ± SEM across mice.

(F) Same as in (D) but for the *Crhr1*$_{VTA}$ group (n = 17 mice).

(G) Same as in (E) but for the *Crhr1*$_{VTA}$ group (n = 17 mice).

(H) Same as in (D) but for the Vgat$_{VTA}$ group (n = 8 mice).

(I) Same as in (E) but for the Vgat$_{VTA}$ group (n = 8 mice).

(J) Z-scored GCaMP fluorescence from recordings aligned to lever-press bout onset, separated by bouts occurring prior to (lighter shade) and after (darker shade) 50% of all completed reinforcement ratios for the *Cck*$_{VTA}$ group (n = 17 mice).
(K) Same as in (J) but for the *Crhr1*$_{VTA}$ group (n = 17 mice).
(L) Same as in (J) but for the Vgat$_{VTA}$ group (n = 8 mice).
(M) Correlations across bouts between percent of breakpoint and mean z-scored GCaMP signal during bout onset for the *Cck*$_{VTA}$ group (n = 165 bouts). Correlation coefficient (r) and p-values on the top right of the plot.
(N) Same as in (M) but for the *Crhr1*$_{VTA}$ group (n = 172 bouts).
(O) Same as in (M) but for the Vgat$_{VTA}$ group (n = 172 bouts).
(P) Pearson's correlation coefficient per mouse between percent breakpoint and mean z-scored GCaMP signal for *Cck*$_{VTA}$ (n = 17 mice), *Crhr1*$_{VTA}$ (n = 17 mice), and Vgat$_{VTA}$ (n = 8 mice) groups (see Supplementary Table 1 for statistical values).

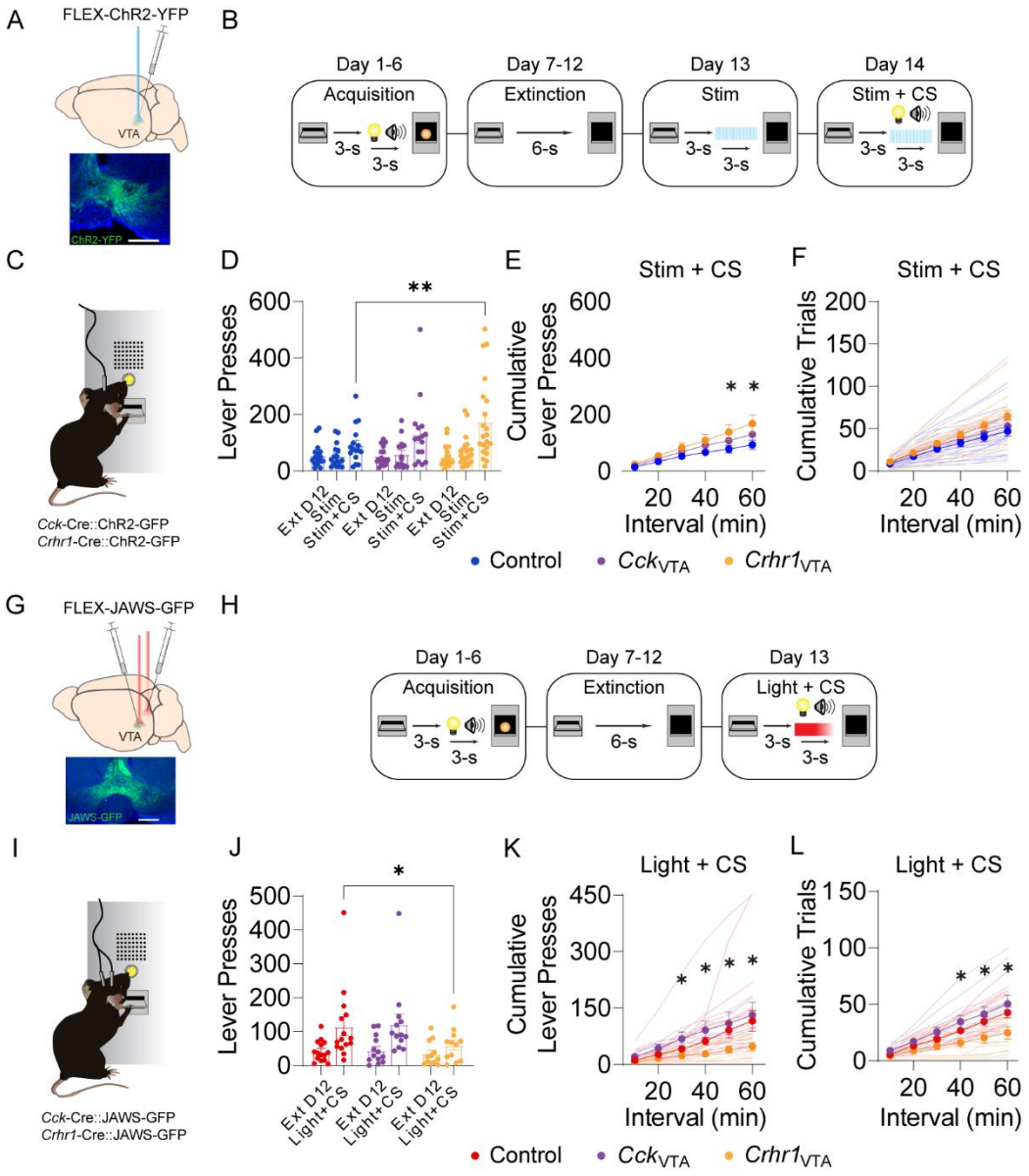


**Figure 5. Photostimulation and photoinhibition of *Crhr1*$_{VTA}$ and *Cck*$_{VTA}$ neurons during cued reinstatement**

(A) Schematic of viral injection and optic fiber implant and example histology image from the VTA showing staining for ChR2-YFP (green) in VTA subpopulations.

(B) Schematic of the training phases of the optogenetic cued reinstatement task. On day 13 an active lever-press triggered a 3 s delay followed by blue light stimulation. On day 14 an active lever-press triggered a 3 s delay followed by blue light stimulation paired with CS presentation.

(C) Schematic of an optogenetic cued reinstatement session with channelrhodopsin (ChR2) stimulation.

(D) Mean number of lever-presses across mice during acquisition and extinction sessions in control, *Cck*$_{VTA}$, and *Crhr1*$_{VTA}$ groups (n = 11-21 mice, error bars represent SEM).

(E) Mean number of cumulative lever-presses on day 14 (Stim + CS) with optogenetic activation, or in control mice without opsin expression (n = 11-21 mice, error bars indicate SEM).

(F) Mean number of cumulative trials completed on day 14 (Stim + CS) with optogenetic activation, or in control mice without opsin expression (n = 11-21 mice, error bars indicate SEM).

(G) Schematic of viral injection and optic fiber implant and example histology image from the VTA showing staining for JAWS-GFP (green) in VTA subpopulations.

(H) Schematic of the training phases of the optogenetic cued reinstatement task. On day 13 an active lever-press triggered a 3 s delay followed by red light stimulation paired with CS presentation.
(I) Schematic of an optogenetic cued reinstatement session with JAWS-GFP (JAWS) stimulation.
(J) Mean number of lever-presses on day 12 (Ext D12), and day 13 (Light + CS) with optogenetic inhibition, or in control mice without opsin expression (n = 12-14 mice, error bars indicate SEM).
(K) Mean number of cumulative lever-presses on day 13 (Light + CS) with optogenetic inhibition, or in control mice without opsin expression (n = 12-14 mice, error bars indicate SEM).
(L) Mean number of cumulative trials completed on day 13 (Light + CS) with optogenetic inhibition, or in control mice without opsin expression (n = 12-14 mice, error bars indicate SEM, see Supplementary Table 1 for statistical values).

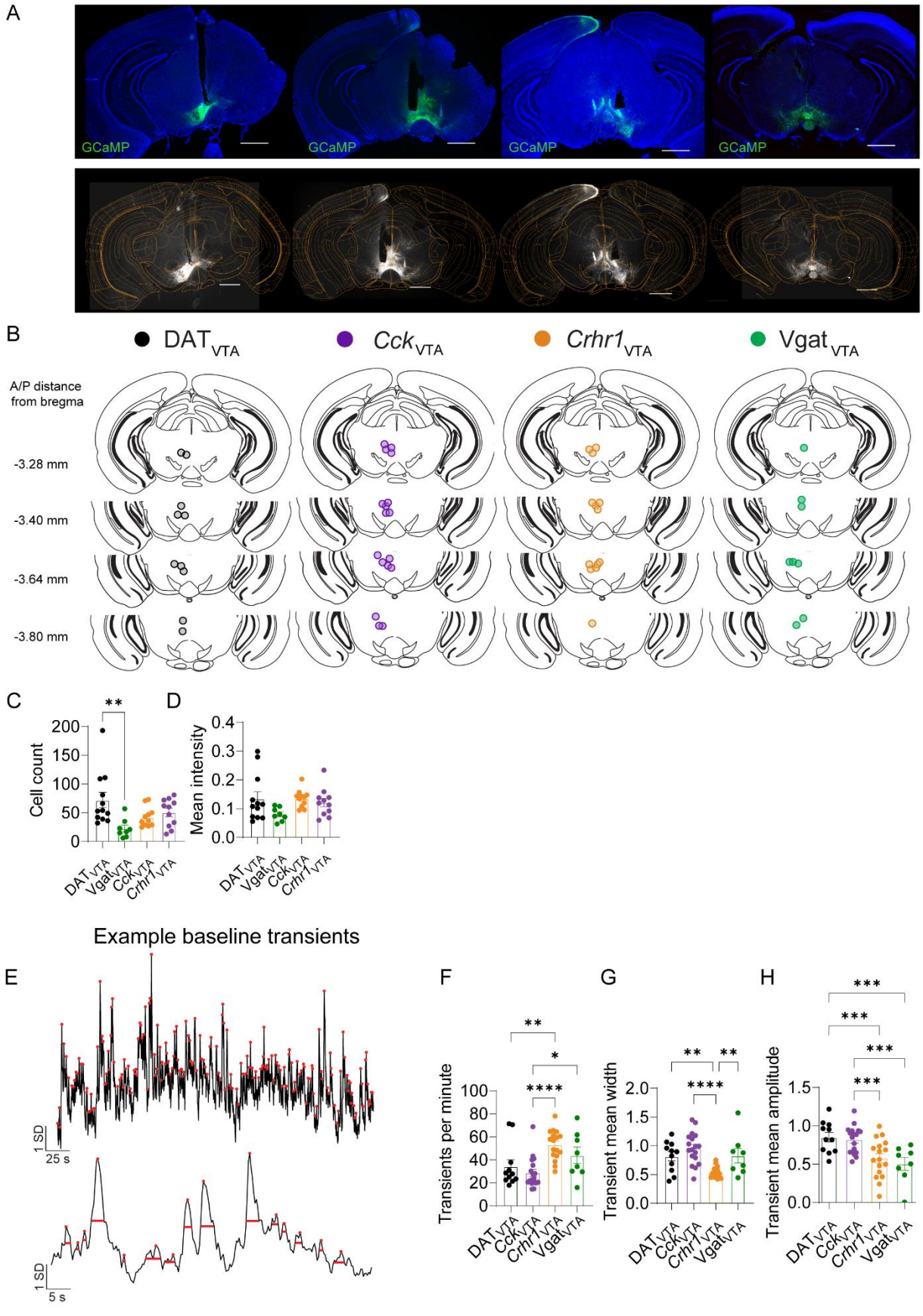
A
GCaMP
GCaMP
GCaMP
GCaMP
B
DAT VTA
Cck VTA
Crhr1 VTA
Vgat VTA
A/P distance from bregma
-3.28 mm
-3.40 mm
-3.64 mm
-3.80 mm
C
Cell count
200
150
100
50
0
**
DAT VTA
Vgat VTA
Cck VTA
Crhr1 VTA
D
Mean intensity
0.4
0.3
0.2
0.1
0.0
DAT VTA
Vgat VTA
Cck VTA
Crhr1 VTA
Example baseline transients
E
1 SD
25 s
1 SD
5 s
F
Transients per minute
100
80
60
40
20
0
**
*
****
DAT VTA
Cck VTA
Crhr1 VTA
Vgat VTA
G
Transient mean width
2.0
1.5
1.0
0.5
0.0
**
**
****
DAT VTA
Cck VTA
Crhr1 VTA
Vgat VTA
H
Transient mean amplitude
1.5
1.0
0.5
0.0
***
***
***
***
DAT VTA
Cck VTA
Crhr1 VTA
Vgat VTA

**Figure 6. Summary of optic fiber tip locations for fiber photometry recordings, GCaMP-labeled cell counts and intensity measurements, baseline calcium transient analysis related to Figures 1-4**

(A) Example histology images from the VTA showing GCaMP expression and recording fiber tip locations (top). Example histology images with brain sections registered to the Allen Brain Atlas (bottom). Scale bar: 500 µm.

(B) Photometry recording fiber locations for DATVTA (n = 10 mice), *Cck*$_{VTA}$ (n = 17 mice), *Crhr1*$_{VTA}$ (n = 13 mice), and Vgat$_{VTA}$ (n = 8 mice). Circles indicate the fiber tip location from individual mice.

(C) Mean number of GFP-positive cells in the VTA in the histology section containing the optic fiber tip location for DATVTA (n = 10 mice), *Cck*$_{VTA}$ (n = 17 mice), *Crhr1*$_{VTA}$ (n = 13 mice), and Vgat$_{VTA}$ (n = 8 mice).

(D) Mean GFP fluorescence intensity in the VTA in the histology section containing the optic fiber tip location for DATVTA (n = 10 mice), *Cck*$_{VTA}$ (n = 17 mice), *Crhr1*$_{VTA}$ (n = 13 mice), and Vgat$_{VTA}$ (n = 8 mice).

(E) Example z-scored GCaMP fluorescence trace showing transient peak classifications (red circles) and transient width measurements (red bars) during baseline photometry recordings.

(F) Mean transients per minute for *Cck*$_{VTA}$ (n = 18 mice), *Crhr1*$_{VTA}$ (n = 17 mice), DATVTA (n = 11 mice), Vgat$_{VTA}$ (n = 8 mice) groups.

(G) Mean transient width for *Cck*$_{VTA}$ (n = 18 mice), *Crhr1*$_{VTA}$ (n = 17 mice), DATVTA (n = 11 mice), Vgat$_{VTA}$ (n = 8 mice) groups.

(H) Mean transient amplitude for *Cck*$_{VTA}$ (n = 18 mice), *Crhr1*$_{VTA}$ (n = 17 mice), DATVTA (n = 11 mice), VgatVTA (n = 8 mice) groups. Bars and error bars indicate mean ± SEM across mice (see Supplementary Table 1 for statistical values).

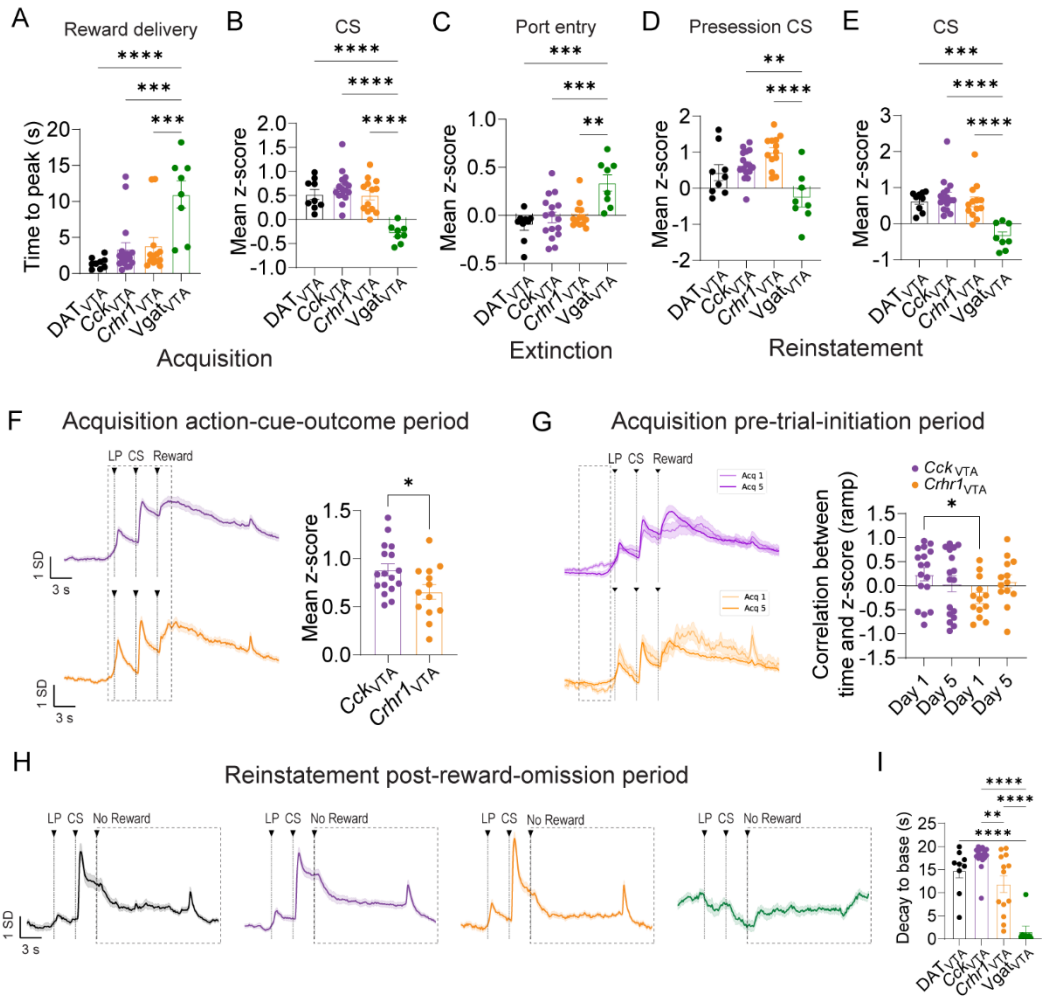


**Figure 7. Further characterization of response profiles, related to Figure 1**

(A) Average latency to peak of z-scored GCaMP fluorescence following reward delivery during acquisition phase of cued reinstatement for $DAT_{VTA}$ (n = 9 mice), *Cck*$_{VTA}$ (n = 16 mice), *Crhr1*$_{VTA}$ (n 13 = mice), $Vgat_{VTA}$ (n = 8 mice) groups.

(B) Average z-scored GCaMP fluorescence during CS presentation period following reward delivery during acquisition phase of cued reinstatement for $DAT_{VTA}$ (n = 9 mice), *Cck*$_{VTA}$ (n = 16 mice), *Crhr1*$_{VTA}$ (n 13 = mice), $Vgat_{VTA}$ (n = 8 mice) groups.

(C) Average z-scored GCaMP fluorescence during port entry period during extinction phase of cued reinstatement for $DAT_{VTA}$ (n = 9 mice), *Cck*$_{VTA}$ (n = 16 mice), *Crhr1*$_{VTA}$ (n 13 = mice), $Vgat_{VTA}$ (n = 8 mice) groups.

(D) Average z-scored GCaMP fluorescence during CS presentation periods during reinstatement presession for $DAT_{VTA}$ (n = 9 mice), *Cck*$_{VTA}$ (n = 16 mice), *Crhr1*$_{VTA}$ (n 13 = mice), $Vgat_{VTA}$ (n = 8 mice) groups.

(E) Average z-scored GCaMP fluorescence during CS presentation periods during reinstatement session for $DAT_{VTA}$ (n = 9 mice), *Cck*$_{VTA}$ (n = 16 mice), *Crhr1*$_{VTA}$ (n 13 = mice), $Vgat_{VTA}$ (n = 8 mice) groups.

(F) Z-scored GCaMP fluorescence aligned to action-cue period during acquisition phase of cued reinstatement in *Cck*$_{VTA}$ (n = 16 mice) and *Crhr1*$_{VTA}$ (n = 13 mice) groups. Dotted rectangle indicates mean z-score analysis epoch.

(G) Z-scored GCaMP fluorescence aligned to trial initiation LP on the first (lighter shade) and last (darker shade) session of acquisition in *Cck*$_{VTA}$ (n = 16 mice) and *Crhr1*$_{VTA}$ (n = 13 mice) groups (left). Pearson's correlation coefficient per mouse between time and z-scored GCaMP signal during the time period prior to trial initiation LP on the first and last session of acquisition for *Cck*$_{VTA}$ (n = 16 mice) and *Crhr1*$_{VTA}$ (n

= 13 mice) groups (right). Dotted rectangle indicates analysis epoch. Bars and error bars indicate mean ± SEM across mice.

(H) Z-scored GCaMP fluorescence aligned to reward omission period during reinstatement phase of cued reinstatement in *Cck*$_{VTA}$ (n = 16 mice) and *Crhr1*$_{VTA}$ (n = 13 mice) groups. Dotted rectangle indicates mean z-score analysis epoch.

(I) Average latency to minimum GCaMP fluorescence during reward omission period during reinstatement session for *Cck*$_{VTA}$ (n = 16 mice) and *Crhr1*$_{VTA}$ (n = 13 mice) groups. Bars and error bars indicate mean ± SEM across mice (see Supplementary Table 1 for statistical values).

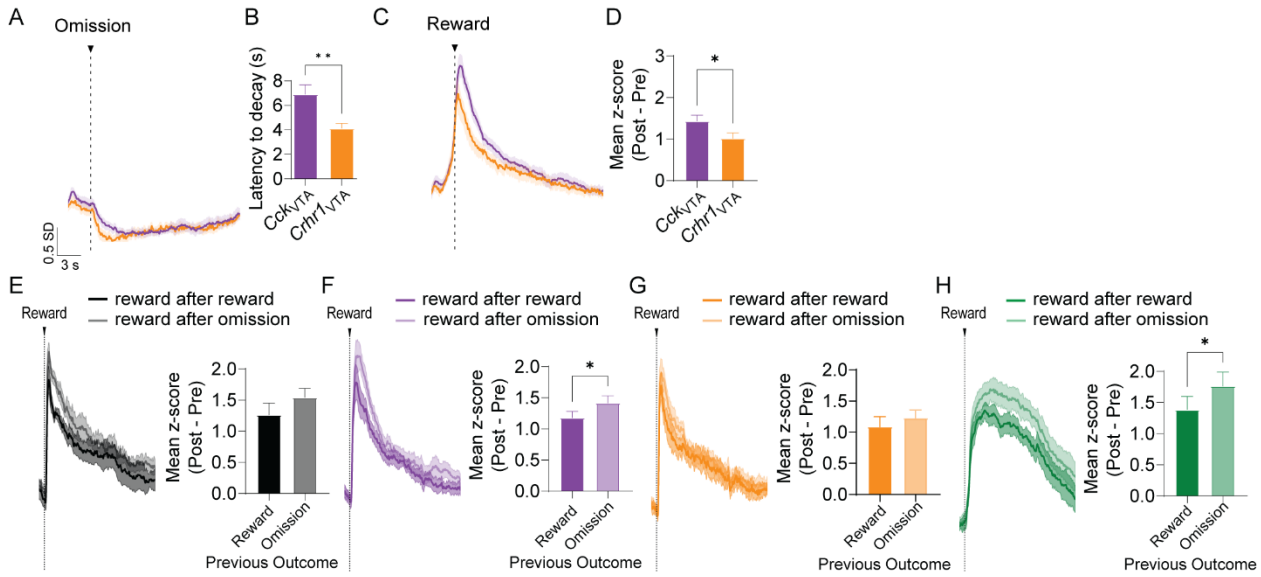


**Figure 8. Further characterization of response profiles, related to Figure 2**

(A) Z-scored GCaMP fluorescence following reward omission during random reward omission for $DAT_{VTA}$ (n = 7 mice), *Cck*$_{VTA}$ (n = 12 mice), and *Crhr1*$_{VTA}$ (n = 13 mice), and $Vgat_{VTA}$ (n = 8 mice) groups.

(B) Average latency to trough of z-scored GCaMP fluorescence following reward during random reward omission for $DAT_{VTA}$ (n = 7 mice), *Cck*$_{VTA}$ (n = 12 mice), and *Crhr1*$_{VTA}$ (n = 13 mice), and $Vgat_{VTA}$ (n = 8 mice) groups.

(C) Z-scored GCaMP fluorescence and average z-scored GCaMP fluorescence during reward omission periods shaded according to previous trial outcome type for $DAT_{VTA}$ (n = 7 mice), *Cck*$_{VTA}$ (n = 12 mice), and *Crhr1*$_{VTA}$ (n = 13 mice), and $Vgat_{VTA}$ groups (n = 8 mice).

(D) Average baselin-subtracted z-scored GCaMP fluorescence following reward during random reward omission for $DAT_{VTA}$ (n = 7 mice), *Cck*$_{VTA}$ (n = 12 mice), and *Crhr1*$_{VTA}$ (n = 13 mice), and $Vgat_{VTA}$ (n = 8 mice) groups.

(E) Z-scored GCaMP fluorescence and average z-scored GCaMP fluorescence during reward omission periods shaded according to previous trial outcome type for $DAT_{VTA}$ (n = 7 mice), see Supplementary Table 1 for statistical values.

(F) Same as in (E) but for the *Cck*$_{VTA}$ group (n = 12 mice).

(G) Same as in (E) but for the *Crhr1*$_{VTA}$ group (n = 13 mice).

(H) Same as in (E) but for the $Vgat_{VTA}$ group (n = 8 mice).

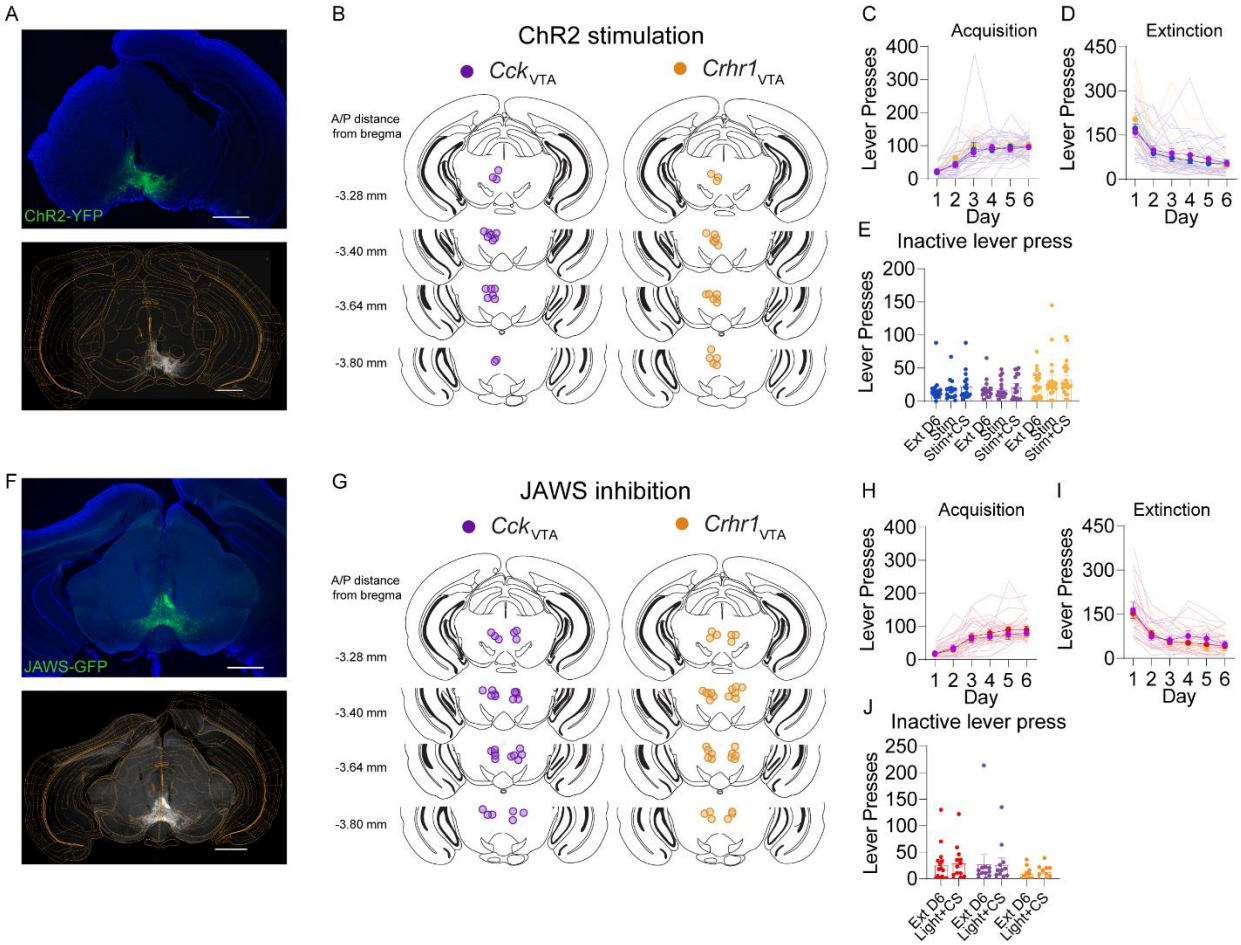


**Figure 9. Summary of optic fiber tip locations for optogenetic manipulations, behavioral performance of mice during optogenetic cued reinstatement task, related to Figure 5**

(A) Example histology image from the VTA showing ChR2-YFP expression and optical fiber tip locations (top). Example histology image with brain section registered to the Allen Brain Atlas (bottom). Scale bar: 500 µm.

(B) Optic fiber tip locations in *Cck*$_{VTA}$ (n = 15 mice) and *Crhr1*$_{VTA}$ (n = 21 mice) groups for the ChR2 stimulation experiment. Circles indicate the fiber tip location from individual mice.

(C) Mean number of active lever-presses across mice during acquisition sessions in control, *Cck*$_{VTA}$, and *Crhr1*$_{VTA}$ groups (n = 11-21 mice, error bars represent SEM).

(D) Mean number of active lever-presses across mice during extinction sessions in control, *Cck*$_{VTA}$, and *Crhr1*$_{VTA}$ groups (n = 11-21 mice, error bars represent SEM).

(E) Mean number of inactive lever-presses across mice during final extinction session, Stim session, and Stim + CS session in control, *Cck*$_{VTA}$, and *Crhr1*$_{VTA}$ groups (n = 11-21 mice, error bars represent SEM).

(F) Example histology image from the VTA showing JAWS-GFP expression and optical fiber tip locations (top). Example histology image with brain section registered to the Allen Brain Atlas (bottom). Scale bar: 500 µm.

(G) *Cck*$_{VTA}$ optic fiber locations in *Cck*$_{VTA}$ (n = 13 mice) and *Crhr1*$_{VTA}$ (n = 14 mice) groups for the JAWS inhibition experiment. Circles indicate the fiber tip location from individual mice.

(H) Mean number of active lever-presses across mice during acquisition sessions in control, *Cck*$_{VTA}$, and *Crhr1*$_{VTA}$ groups (n = 12-14 mice, error bars represent SEM).

(I) Mean number of active lever-presses across mice during extinction sessions in control, *Cck*$_{VTA}$, and *Crhr1*$_{VTA}$ groups (n = 12-14 mice, error bars represent SEM).

(J) Mean number of inactive lever-presses across mice during final extinction session, Stim session, and Stim + CS session in control, *Cck*$_{VTA}$, and *Crhr1*$_{VTA}$ groups (n = 12-14 mice, error bars represent SEM, see Supplementary Table 1 for statistical values).

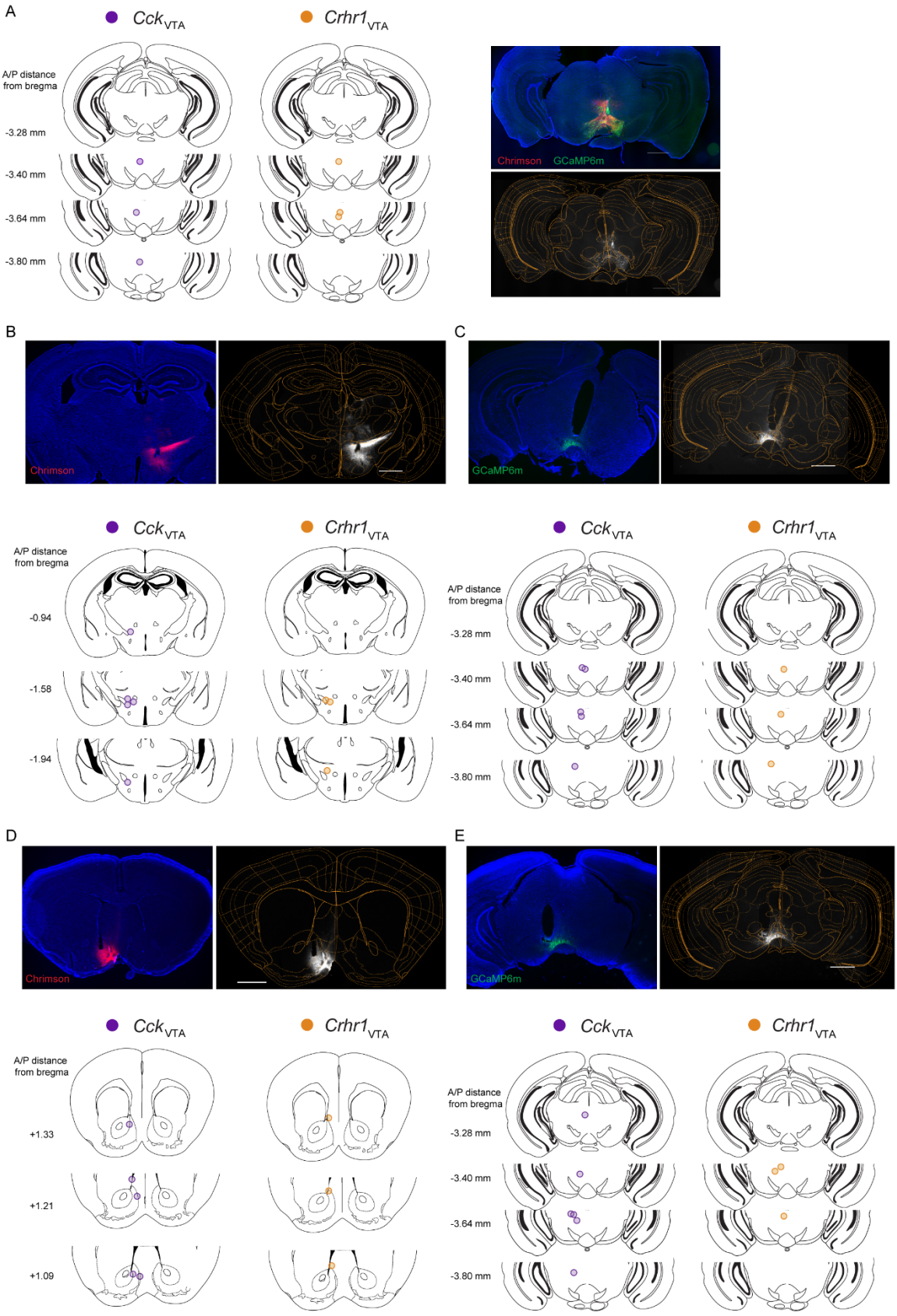
A
Cck VTA
Crhr1 VTA
A/P distance from bregma
-3.28 mm
-3.40 mm
-3.64 mm
-3.80 mm
Chrimson GCaMP6m
B
Chrimson
C
GCaMP6m
Cck VTA
Crhr1 VTA
A/P distance from bregma
-0.94
-1.58
-1.94
-3.28 mm
-3.40 mm
-3.64 mm
-3.80 mm
D
Chrimson
E
GCaMP6m
+1.33
+1.21
+1.09

**Figure 10. Summary of optic fiber tip locations for dual optogenetic stimulation and fiber photometry recordings**

(A) Optic fiber tip locations in the VTA for *Cck*$_{VTA}$ (n = 3 mice) and *Crhr1*$_{VTA}$ (n = 3 mice) groups for the Vgat$_{VTA}$ stimulation with dual photometry experiment. Circles indicate the fiber tip location from individual mice (right). Example histology image from the VTA showing GCaMP and Chrimson expression and optical fiber tip location (right). Scale bar: 500 µm.

(B) Example histology image from the LH showing Chrimson expression and optical fiber tip location (top). Optic fiber tip locations in the LH for *Cck*$_{VTA}$ (n = 5 mice) and *Crhr1*$_{VTA}$ (n = 3 mice) groups for the LH GABA stimulation with dual photometry experiment (bottom). Scale bar: 500 µm.

(C) Example histology image from the VTA showing GCaMP expression and optical fiber tip location (top). Optic fiber tip locations in the VTA for *Cck*$_{VTA}$ (n = 5 mice) and *Crhr1*$_{VTA}$ (n = 3 mice) groups for the LH GABA stimulation with dual photometry experiment (bottom). Scale bar: 500 µm.

(D) Example histology image from the NAc mshell showing Chrimson expression and optical fiber tip location (top). Optic fiber tip locations in NAc mshell for *Cck*$_{VTA}$ (n = 3 mice) and *Crhr1*$_{VTA}$ (n = 3 mice) groups for the NAc mshell GABA stimulation with dual photometry experiment (bottom). Scale bar: 500 µm.

(E) Example histology image from the VTA showing GCaMP expression and optical fiber tip location (top). Optic fiber tip locations in VTA for *Cck*$_{VTA}$ (n = 3 mice) and *Crhr1*$_{VTA}$ (n = 3 mice) groups for the NAc mshell GABA stimulation with dual photometry experiment (bottom). Scale bar: 500 µm.

## Supplementary Table 1

| Figure | Description | Sample size | Statistical test | Test Statistic | *p Value* | Significance | Multiple comparisons correction | Adjusted *p* Values |
|---|---|---|---|---|---|---|---|---|
| 1F | Difference in mean z-scored fluorescence from DATVTA neurons during LP, CS, reward, port entry, and omission periods | 9 mice | One-way RM ANOVA | F (2.277, 18.22) = 16.64 | <0.0001 | **** | Bonferroni's multiple comparisons test | Pre-LP vs. Post-LP, p = 0.004, Pre-LP vs. CS, p <0.0001, Pre-LP vs. Reward, p = 0.0006, Post-LP vs. CS, p = 0.0014, Post-LP vs. Reward, p = 0.0123, CS vs. Reward, p >0.9999, Pre-LP vs. Post-LP, p = 0.0004, Pre- LP vs. Pre-Entry, p = 0.0237, Pre-LP vs. Post-Entry, p = 0.0845, Post-LP vs. Pre-Entry, p >0.9999, Post-LP vs. Post-Entry, p >0.9999, Pre-Entry vs. Post-Entry, p >0.9999, CS Presentation vs. CS, p >0.9999, Pre-LP vs. Post-LP, p = 0.367, Pre-LP vs. CS, p = 0.0004, Pre-LP vs. Omission, p = 0.0013, Post-LP vs. CS, p = 0.0006, Post-LP vs. Omission, p = 0.009, CS vs. Omission, p = 0.0005 |
| 1F | Difference in mean z-scored fluorescence from CckVTA neurons during LP, CS, reward, port entry, and omission periods | 16 mice | One-way RM ANOVA | F (3.848, 57.72) = 37.38 | <0.0001 | **** | Bonferroni's multiple comparisons test | Pre-LP vs. Post-LP, p <0.0001, Pre-LP vs. CS, p <0.0001, Pre-LP vs. Reward, p <0.0001, Post-LP vs. CS, p <0.0001, Post-LP vs. Reward, p = 0.0152, CS vs. Reward, p >0.9999, Pre-LP vs. Post-LP, p = 0.0017, Pre- LP vs. Pre-Entry, p = 0.7866, Pre-LP vs. Post-Entry, p = 0.0288, Post-LP vs. Pre-Entry, p = 0.6836, Post-LP vs. Post-Entry, p >0.9999, Pre-Entry vs. Post-Entry, p = 0.0223, Presession CS vs. CS, p >0.9999, Pre-LP vs. Post- LP, p = 0.0025, Pre-LP vs. CS, p <0.0001, Pre-LP vs. Omission, p <0.0001, Post-LP vs. CS, p <0.0001, Post-LP vs. Omission, p = 0.0531, CS vs. Omission, p <0.0001 |
| 1F | Difference in mean z-scored fluorescence from Chrr1VTA neurons during LP, CS, reward, port entry, and omission periods | 13 mice | One-way RM ANOVA | F (3.738, 44.86) = 48.96 | <0.0001 | **** | Bonferroni's multiple comparisons test | Pre-LP vs. Post-LP, p <0.0001, Pre-LP vs. CS, p <0.0001, Pre-LP vs. Reward, p <0.0001, Post-LP vs. CS, p = 0.0012, Post-LP vs. Reward, p = 0.0069, CS vs. Reward, p >0.9999, Pre-LP vs. Post-LP, p = 0.0017, Pre- LP vs. Pre-Entry, p = 0.7686, Pre-LP vs. Post-Entry, p <0.0001, Post-LP vs. Pre-Entry, p = 0.2083, Post-LP vs. Post-Entry, p >0.9999, Pre-Entry vs. Post-Entry, p <0.0001, Presession CS vs. CS, p = 0.317, Pre-LP vs. Post- LP, p = 0.0004, Pre-LP vs. CS, p <0.0001, Pre-LP vs. Omission, p = 0.001, Post-LP vs. CS, p <0.0001, Post-LP vs. Omission, p >0.9999, CS vs. Omission, p <0.0001 |
| 1F | Difference in mean z-scored fluorescence from VgatVTA neurons during LP, CS, reward, port entry, and omission periods | 8 mice | One-way RM ANOVA | F (3.110, 21.77) = 7.521 | 0.0011 | ** | Bonferroni's multiple comparisons test | Pre-LP vs. Post-LP, p >0.9999, Pre-LP vs. CS, p >0.9999, Pre-LP vs. Reward, p = 0.007, Post-LP vs. CS, p >0.9999, Post-LP vs. Reward, p = 0.0673, CS vs. Reward, p = 0.0003, Pre-LP vs. Post-LP, p >0.9999, Pre- LP vs. Pre-Entry, p >0.9999, Pre-LP vs. Post-Entry, p >0.9999, Post-LP vs. Pre-Entry, p >0.9999, Post-LP vs. Post-Entry, p = 0.3414, Pre-Entry vs. Post-Entry, p = 0.093, CS Presentation vs. CS, p >0.9999, Pre-LP vs. Post- LP, p >0.9999, Pre-LP vs. CS, p = 0.0995, Pre-LP vs. Omission, p = 0.5874, Post-LP vs. CS, p >0.9999, Post-LP vs. Omission, p >0.9999, CS vs. Omission, p = 0.0658 |
| 2C | Difference in mean trial initation latency across previous outcome conditions | 25 mice | Paired t test | t=7.255, df=24 | <0.0001 | **** | NA | NA |
| 2E | Difference in mean z-scored fluorescence from DATVTA neurons during reward, omission, and port entry periods | 7 mice | One-way RM ANOVA | F (1.307, 7.841) = 42.73 | 0.0001 | *** | Bonferroni's multiple comparisons test | Pre-Reward vs. Reward Entry, p = 0.0016, Pre-Reward vs. Pre-Omission, p = 0.0235, Pre-Reward vs. Omission Entry, p = 0.0194, Reward Entry vs. Pre-Omission, p = 0.0018, Reward Entry vs. Omission Entry, p = 0.0024, Pre-Omission vs. Omission Entry, p = 0.0559 |
| 2E | Difference in mean z-scored fluorescence from CckVTA neurons during reward, omission, and port entry periods | 12 mice | One-way RM ANOVA | F (1.942, 21.36) = 130.5 | <0.0001 | **** | Bonferroni's multiple comparisons test | Pre-Reward vs. Reward Entry, p <0.0001, Pre-Reward vs. Pre-Omission, p = 0.0051, Pre-Reward vs. Omission Entry, p <0.0001, Reward Entry vs. Pre-Omission, p <0.0001, Reward Entry vs. Omission Entry, p <0.0001, Pre-Omission vs. Omission Entry, p = 0.0016 |

| | | | | | | | | |
|---|---|---|---|---|---|---|---|---|
| 2E | Difference in mean z-scored fluorescence from Crhr1VTA neurons during reward, omission, and port entry periods | 13 mice | One-way RM ANOVA | F (1.192, 14.31) = 57.72 | <0.0001 | **** | Bonferroni's multiple comparisons test | Pre-Reward vs. Reward Entry, p <0.0001, Pre-Reward vs. Pre-Omission, p = 0.0031, Pre-Reward vs. Omission Entry, p = 0.0001, Reward Entry vs. Pre-Omission, p <0.0001, Reward Entry vs. Omission Entry, p <0.0001, Pre-Omission vs. Omission Entry, p = 0.001 |
| 2E | Difference in mean z-scored fluorescence from VgatVTA neurons during reward, omission, and port entry periods | 8 mice | One-way RM ANOVA | F (1.259, 8.810) = 54.82 | <0.0001 | **** | Bonferroni's multiple comparisons test | Pre-Reward vs. Reward Entry, p <0.0001, Pre-Reward vs. Pre-Omission, p = 0.7888, Pre-Reward vs. Omission Entry, p >0.9999, Reward Entry vs. Pre-Omission, p <0.0001, Reward Entry vs. Omission Entry, p = 0.0039, Pre-Omission vs. Omission Entry, p = 0.1586 |
| 2F | Difference in baseline subtracted mean z-scored fluorescence from DATVTA neurons during port entry across rewarded and unrewarded trials | 5 mice | Paired t test | t=3.606, df=4 | 0.0226 | * | NA | NA |
| 2F | Difference in baseline subtracted mean z-scored fluorescence from CckVTA neurons during port entry across rewarded and unrewarded trials | 11 mice | Paired t test | t=1.529, df=10 | 0.1572 | ns | NA | NA |
| 2F | Difference in baseline subtracted mean z-scored fluorescence from Crhr1VTA neurons during port entry across rewarded and unrewarded trials | 9 mice | Paired t test | t=5.510, df=8 | 0.0006 | *** | NA | NA |
| 2F | Difference in baseline subtracted mean z-scored fluorescence from VgatVTA neurons during port entry across rewarded and unrewarded trials | 8 mice | Paired t test | t=0.07836, df=7 | 0.9397 | ns | NA | NA |
| 2H | Difference from 0 for mean regression coefficients for the DATVTA group obtained from the outcome history linear regression across outcomes of current and previous five trials | 7 mice | One sample t test | 0 trials back, t=5.792, df=6, 1 trials back, t=0.8894, df=6, 2 trials back, t=1.951, df=6, 3 trials back, t=1.829, df=6, 4 trials back, t=0.9873, df=6, 5 trials back, t=0.6871, df=6 | 0 trials back, p = 0.0012, 1 trials back, p = 0.408, 2 trials back, p = 0.099, 3 trials back, p = 0.1172, 4 trials back, p = 0.3616, 5 trials back, p = 0.5177 | 0 trials back, **, 1 trials back, ns, 2 trials back, ns, 3 trials back, ns, 4 trials back, ns, 5 trials back, ns | NA | NA |
| 2H | Difference from 0 for mean regression coefficients for the CckVTA group obtained from the outcome history linear regression across outcomes of current and previous five trials | 12 mice | One sample t test | 0 trials back, t=11.72, df=11, 1 trials back, t=0.4769, df=11, 2 trials back, t=0.1924, df=11, 3 trials back, t=0.8125, df=11, 4 trials back, t=1.273, df=11, 5 trials back, t=0.6066, df=11 | 0 trials back, p<0.0001, 1 trials back, p = 0.6428, 2 trials back, p = 0.8509, 3 trials back, p = 0.4337, 4 trials back, p = 0.2293, 5 trials back, p = 0.5564 | 0 trials back, ****, 1 trials back, ns, 2 trials back, ns, 3 trials back, ns, 4 trials back, ns, 5 trials back, ns | NA | NA |
| 2H | Difference from 0 for mean regression coefficients for the Crhr1VTA group obtained from the outcome history linear regression across outcomes of current and previous five trials | 13 mice | One sample t test | 0 trials back, t=14.73, df=12, 1 trials back, t=2.410, df=12, 2 trials back, t=0.3809, df=12, 3 trials back, t=0.4576, df=12, 4 trials back, t=0.1065, df=12, 5 trials back, t=0.1201, df=12 | 0 trials back, p<0.0001, 1 trials back, p = 0.0329, 2 trials back, p = 0.71, 3 trials back, p = 0.6554, 4 trials back, p = 0.9169, 5 trials back, p = 0.9064 | 0 trials back, ****, 1 trials back, *, 2 trials back, ns, 3 trials back, ns, 4 trials back, ns, 5 trials back, ns | NA | NA |

| | | | | | | | | |
|---|---|---|---|---|---|---|---|---|
| 3C | Difference in mean relative contribution of task event types to explained variance of the GCaMP signal during action-cue period task events for the CckVTA group | 12 mice | One-way RM ANOVA | F (1.722, 18.95) = 30.65 | <0.0001 | **** | Tukey's multiple comparisons test | Active LP vs. Cues, p = 0.0003, Active LP vs. Inactive LP, p = 0.1106, Active LP vs. Trial LP, p = 0.0009, Cues vs. Inactive LP, p <0.0001, Cues vs. Trial LP, p = 0.5418, Inactive LP vs. Trial LP, p <0.0001 |
| 3C | Difference in mean relative contribution of task event types to explained variance of the GCaMP signal during action-cue period task events for the Crhr1VTA group | 11 mice | One-way RM ANOVA | F (1.995, 19.95) = 43.61 | <0.0001 | **** | Tukey's multiple comparisons test | Active LP vs. Cues, p = 0.0002, Active LP vs. Inactive LP, p = 0.4289, Active LP vs. Trial LP, p = 0.1958, Cues vs. Inactive LP, p <0.0001, Cues vs. Trial LP, p = 0.0005, Inactive LP vs. Trial LP, p = 0.017 |
| 3C | Difference in mean relative contribution of task event types to explained variance of the GCaMP signal during action-cue period task events for the VgatVTA group | 8 mice | One-way RM ANOVA | F (1.995, 19.95) = 43.61 | <0.0001 | **** | Tukey's multiple comparisons test | Active LP vs. Cues, p = 0.9435, Active LP vs. Inactive LP, p = 0.6411, Active LP vs. Trial LP, p = 0.9592, Cues vs. Inactive LP, p = 0.9077, Cues vs. Trial LP, p = 0.9998, Inactive LP vs. Trial LP, p = 0.846 |
| 3D | Difference in mean relative contribution of task event types to explained variance of the GCaMP signal during outcome period task events for the CckVTA group | 12 mice | One-way RM ANOVA | F (1.512, 16.63) = 12.46 | 0.001 | ** | Tukey's multiple comparisons test | Omission vs. Omission entry, p = 0.9984, Omission vs. Reward, p = 0.0058, Omission vs. Reward entry, p = 0.2193, Omission vs. Port Enry, p = 0.992, Omission entry vs. Reward, p = 0.0033, Omission entry vs. Reward entry, p = 0.2163, Omission entry vs. Port Enry, p = 0.9946, Reward vs. Reward entry, p = 0.2253, Reward vs. Port Enry, p = 0.0009, Reward entry vs. Port Enry, p = 0.4274 |
| 3D | Difference in mean relative contribution of task event types to explained variance of the GCaMP signal during outcome period task events for the Crhr1VTA group | 11 mice | One-way RM ANOVA | F (1.324, 13.24) = 11.51 | 0.0029 | ** | Tukey's multiple comparisons test | Omission vs. Omission Entry, p = 0.8526, Omission vs. Reward, p = 0.0593, Omission vs. Reward Entry, p = 0.3044, Omission vs. Port Entry, p = 0.021, Omission Entry vs. Reward, p = 0.01, Omission Entry vs. Reward Entry, p = 0.1653, Omission Entry vs. Port Entry, p = 0.3548, Reward vs. Reward Entry, p = 0.2884, Reward vs. Port Entry, p = 0.0046, Reward Entry vs. Port Entry, p = 0.0083 |
| 3D | Difference in mean relative contribution of task event types to explained variance of the GCaMP signal during outcome period task events for the VgatVTA group | 8 mice | One-way RM ANOVA | F (1.135, 7.947) = 10.90 | 0.0096 | ** | Tukey's multiple comparisons test | Omission vs. Omission Entry, p = 0.8987, Omission vs. Reward, p = 0.2621, Omission vs. Reward Entry, p = 0.0115, Omission vs. Port Entry, p = 0.9514, Omission Entry vs. Reward, p = 0.2221, Omission Entry vs. Reward Entry, p = 0.0063, Omission Entry vs. Port Entry, p = 0.9983, Reward vs. Reward Entry, p = 0.5796, Reward vs. Port Entry, p = 0.2463, Reward Entry vs. Port Entry, p = 0.0051 |
| 4E | Difference in mean z-scored fluorescence from CckVTA neurons during LP, port entry, and reward retrieval periods | 17 mice | One-way RM ANOVA | F (2.352, 37.63) = 46.86 | <0.0001 | **** | Bonferroni's multiple comparisons test | Pre-LP vs. Post-LP, p <0.0001, Pre-HE vs. Post-HE, p = 0.0236, Pre- Retrieval vs. Post-Retrieval, p <0.0001 |
| 4E | Difference in mean z-scored fluorescence from Crhr1VTA neurons during LP, port entry, and reward retrieval periods | 17 mice | One-way RM ANOVA | F (1.686, 26.98) = 47.14 | <0.0001 | **** | Bonferroni's multiple comparisons test | Pre-LP vs. Post-LP, p <0.0001, Pre-HE vs. Post-HE, p = 0.0236, Pre- Retrieval vs. Post-Retrieval, p <0.0001 |
| 4E | Difference in mean z-scored fluorescence from VgatVTA neurons during LP, port entry, and reward retrieval periods | 7 mice | One-way RM ANOVA | F (1.635, 9.807) = 15.96 | 0.0012 | ** | Bonferroni's multiple comparisons test | Pre-LP vs. Post-LP, p >0.9999, Pre-HE vs. Post-HE, p >0.9999, Pre- Retrieval vs. Post-Retrieval, p = , p 0.0465 |

| | | | | | | | | |
|---|---|---|---|---|---|---|---|---|
| 4G | Relationship between fraction of breakpoint and mean z-scored fluorescence during lever press bout onset period across the progressive ratio session for the CckVTA group | 165 bouts | Pearson's correlation | r = -0.4195 | <0.0001 | **** | NA | NA |
| 4G | Relationship between fraction of breakpoint and mean z-scored fluorescence during lever press bout onset period across the progressive ratio session for the Crhr1VTA group | 172 bouts | Pearson's correlation | r = -0.07743 | 0.3127 | ns | NA | NA |
| 4G | Relationship between fraction of breakpoint and mean z-scored fluorescence during lever press bout onset period across the progressive ratio session for the VgatVTA group | 172 bouts | Pearson's correlation | r = -0.07549 | 0.325 | ns | NA | NA |
| 4H | Difference in mean correlation coefficient from the % breakpoint and mean z-scored fluorescence during lever press bout onset correlation between CckVTA, Crhr1VTA, and VgatVTA groups | 17 mice from CckVTA group, 17 mice from Crhr1VTA group, 7 mice from VgatVTA group | Ordinary one-way ANOVA | F (2, 38) = 2.077 | 0.1393 | ns | Two-stage linear step-up procedure of Benjamini, Krieger and Yekutieli | Cck vs. Crhr1, p = 0.0486, Cck vs. Vgat, p = 0.4115, Crhr1 vs. Vgat, p = 0.4725 |
| 5D | Difference in mean lever presses between CckVTA, Crhr1VTA, and control groups across conditioning sessions of ChR2 stimulation experiment | 16 mice from control group, 16 mice from CckVTA group, 21 mice from Crhr1VTA group | Two-way RM ANOVA | F (4, 100) = 2.572 | 0.0423 | * | Bonferroni's multiple comparisons test | Ext D6 Control vs. CckVTA, p >0.9999, Ext D6 Control vs. Crhr1VTA, p >0.9999, Ext D6 CckVTA vs. Crhr1VTA, p >0.9999, Stim Control vs. CckVTA, p >0.9999, Stim Control vs. Crhr1VTA, p >0.9999, Stim CckVTA vs. Crhr1VTA, p >0.9999, Stim+CS Control vs. CckVTA, p = 0.5183, Stim+CS Control vs. Crhr1VTA, p = 0.0085, Stim+CS CckVTA vs. Crhr1VTA, p = 0.3524 |
| 5E | Difference in mean number of cumulative lever presses between CckVTA, Crhr1VTA, and control groups during the reinstatement session of ChR2 stimulation experiment | 16 mice from control group, 16 mice from CckVTA group, 21 mice from Crhr1VTA group | Two-way RM ANOVA | F (10, 255) = 1.839 | 0.0543 | ns | Two-stage linear step-up procedure of Benjamini, Krieger and Yekutieli | 10 CckVTA vs. Control, p = 0.3075, 10 CckVTA vs. Crhr1VTA, p = 0.4786, 10 Control vs. Crhr1VTA, p = 0.0818, 20 CckVTA vs. Control, p = 0.3629, 20 CckVTA vs. Crhr1VTA, p = 0.446, 20 Control vs. Crhr1VTA, p = 0.1197, 30 CckVTA vs. Control, p = 0.3863, 30 CckVTA vs. Crhr1VTA, p = 0.4173, 30 Control vs. Crhr1VTA, p = 0.122, 40 CckVTA vs. Control, p = 0.3185, 40 CckVTA vs. Crhr1VTA, p = 0.4695, 40 Control vs. Crhr1VTA, p = 0.0968, 50 CckVTA vs. Control, p = 0.328, 50 CckVTA vs. Crhr1VTA, p = 0.3547, 50 Control vs. Crhr1VTA, p = 0.0511, 60 CckVTA vs. Control, p = 0.3293, 60 CckVTA vs. Crhr1VTA, p = 0.3127, 60 Control vs. Crhr1VTA, p = 0.0391 |
| 5F | Difference in mean number of trials completed between CckVTA, Crhr1VTA, and control groups during the reinstatement session of ChR2 stimulation experiment | 16 mice from control group, 16 mice from CckVTA group, 21 mice from Crhr1VTA group | Two-way RM ANOVA | F (10, 250) = 1.928 | 0.042 | * | Two-stage linear step-up procedure of Benjamini, Krieger and Yekutieli | 10 CckVTA vs. Control, p = 0.5017, 10 CckVTA vs. Crhr1VTA, p = 0.533, 10 Control vs. Crhr1VTA, p = 0.127, 20 CckVTA vs. Control, p = 0.3328, 20 CckVTA vs. Crhr1VTA, p = 0.8697, 20 Control vs. Crhr1VTA, p = 0.2305, 30 CckVTA vs. Control, p = 0.3973, 30 CckVTA vs. Crhr1VTA, p = 0.6502, 30 Control vs. Crhr1VTA, p = 0.1911, 40 CckVTA vs. Control, p = 0.4409, 40 CckVTA vs. Crhr1VTA, p = 0.5406, 40 Control vs. Crhr1VTA, p = 0.1452, 50 CckVTA vs. Control, p = 0.5814, 50 CckVTA vs. Crhr1VTA, p = 0.2845, 50 Control vs. Crhr1VTA, p = 0.0744, 60 CckVTA vs. Control, p = 0.5462, 60 CckVTA vs. Crhr1VTA, p = 0.2506, 60 Control vs. Crhr1VTA, p = 0.0525 |
| 5J | Difference in mean lever presses between CckVTA, Crhr1VTA, and control groups across conditioning sessions of JAWS inhibition experiment | 15 mice from control group, 11 mice from CckVTA group, 10 mice from Crhr1VTA group | Two-way RM ANOVA | F (2, 33) = 1.387 | 0.264 | ns | Two-stage linear step-up procedure of Benjamini, Krieger and Yekutieli | Ext D6 Control vs. CckVTA, p = 0.7314, Ext D6 Control vs. Crhr1VTA, p = 0.6253, Ext D6 CckVTA vs. Crhr1VTA, p = 0.4431, Light+CS Control vs. CckVTA, p = 0.5853, Light+CS Control vs. Crhr1VTA, p = 0.0236, Light+CS CckVTA vs. Crhr1VTA, p = 0.0097 |

| | | | | | | | | |
|---|---|---|---|---|---|---|---|---|
| 5K | Difference in mean number of cumulative lever presses between CckVTA, Crhr1VTA, and control groups during the reinstatement session of JAWS stimulation experiment | 15 mice from control group, 11 mice from CckVTA group, 10 mice from Crhr1VTA group | Two-way RM ANOVA | F (10, 165) = 1.850 | 0.0557 | ns | Two-stage linear step-up procedure of Benjamini, Krieger and Yekutieli | 10 CckVTA vs. Control, p = 0.1364, 10 CckVTA vs. Crhr1VTA, p = 0.0213, 10 Control vs. Crhr1VTA, p = 0.0979, 20 CckVTA vs. Control, p = 0.2017, 20 CckVTA vs. Crhr1VTA, p = 0.0432, 20 Control vs. Crhr1VTA, p = 0.0667, 30 CckVTA vs. Control, p = 0.2013, 30 CckVTA vs. Crhr1VTA, p = 0.0423, 30 Control vs. Crhr1VTA, p = 0.0493, 40 CckVTA vs. Control, p = 0.3051, 40 CckVTA vs. Crhr1VTA, p = 0.0328, 40 Control vs. Crhr1VTA, p = 0.0112, 50 CckVTA vs. Control, p = 0.6234, 50 CckVTA vs. Crhr1VTA, p = 0.0485, 50 Control vs. Crhr1VTA, p = 0.0322, 60 CckVTA vs. Control, p = 0.7259, 60 CckVTA vs. Crhr1VTA, p = 0.0382, 60 Control vs. Crhr1VTA, p = 0.0362 |
| 5L | Difference in mean number of trials completed between CckVTA, Crhr1VTA, and control groups during the reinstatement session of JAWS stimulation experiment | 15 mice from control group, 11 mice from CckVTA group, 10 mice from Crhr1VTA group | Two-way RM ANOVA | F (10, 165) = 3.317 | 0.0006 | *** | Two-stage linear step-up procedure of Benjamini, Krieger and Yekutieli | 10 CckVTA vs. Control, p = 0.0563, 10 CckVTA vs. Crhr1VTA, p = 0.0212, 10 Control vs. Crhr1VTA, p = 0.363, 20 CckVTA vs. Control, p = 0.2233, 20 CckVTA vs. Crhr1VTA, p = 0.0299, 20 Control vs. Crhr1VTA, p = 0.1233, 30 CckVTA vs. Control, p = 0.2071, 30 CckVTA vs. Crhr1VTA, p = 0.0313, 30 Control vs. Crhr1VTA, p = 0.1304, 40 CckVTA vs. Control, p = 0.2319, 40 CckVTA vs. Crhr1VTA, p = 0.0152, 40 Control vs. Crhr1VTA, p = 0.0481, 50 CckVTA vs. Control, p = 0.4144, 50 CckVTA vs. Crhr1VTA, p = 0.0206, 50 Control vs. Crhr1VTA, p = 0.0319, 60 CckVTA vs. Control, p = 0.4217, 60 CckVTA vs. Crhr1VTA, p = 0.0163, 60 Control vs. Crhr1VTA, p = 0.0247 |

## Chapter 3

## Ventral tegmental area dopamine subpopulations are heterogeneous in their intrinsic properties and brain-wide monosynaptic input

### 3.1 Introduction

Monosynaptic tracing studies have revealed that projection-defined VTA dopamine neurons receive inputs from a diverse array of brain regions (Watabe-Uchida et al., 2012; Tian et al., 2016, Beier et al., 2015; Lammel et al., 2012) many of which carry mixed information related to reward prediction (Tian et al., 2016). Among the numerous inputs to VTA neurons, many are inhibitory and synapse onto VTA GABAergic neurons (Soden et al., 2020), resulting in disinhibition of VTA dopamine neurons (Johnson et al., 1992; Jhou et al., 2009; Nieh et al., 2016; Yang et al., 2018). In addition to heterogeneous afferent and efferent connectivity, distinct dopamine projection populations have distinct electrophysiological properties (Lammel et al., 2008; Lammel et al., 2011; Poulin et al., 2018; Heymann et al., 2020), and ion channel expression patterns (Juarez et al., 2023; Simon et al., 2023), factors that likely contribute to their distinct functional properties. Here, we use electrophysiology, targeted optogenetics, and whole-brain input mapping to assess heterogeneity among these VTA subpopulations.

### 3.2 Results

#### *3.2.1 Baseline electrophysiological properties of Crhr1$_{VTA}$ and Cck$_{VTA}$ populations*

We examined whether intrinsic electrophysiological properties could underlie the differential response profiles of *Cck*$_{VTA}$ and *Crhr1*$_{VTA}$ neurons during behavior. To label neurons for recording, we injected *Cck*-Cre and *Crhr1*-Cre mice with an AAV carrying Cre-dependent eYFP in the VTA (**Figure 11A**). We performed whole-cell, voltage and current-clamp recording *ex vivo* and found distinct properties of excitability and inhibitory transmission in *Cck*$_{VTA}$ and *Crhr1*$_{VTA}$ neurons (**Figure 11B-11J**). To examine the intrinsic excitability of Crhr1$_{VTA}$ and Cck$_{VTA}$ subpopulations, we recorded action potential firing from eYFP-labeled cells in response to increasing steps of current injection (**Figure 11B-11D**). *Cck*$_{VTA}$ and *Crhr1*$_{VTA}$ neurons continued to increase firing with increasing current injections (**Figure 11C**). However, *Cck*$_{VTA}$ neurons fired a greater number of action potentials in response to depolarizing steps of current and showed a shorter latency to spike following current injection compared to *Crhr1*$_{VTA}$ neurons (**Figure 11C-11D**). These results

revealed an increased excitability of *Cck*$_{VTA}$ neurons which could contribute to their sustained activity profiles during behavior.

We then performed voltage-clamp recordings and recorded spontaneous inhibitory postsynaptic currents (sIPSCs), which reflect spontaneous neurotransmitter release (**Figure 11E**). *Cck*$_{VTA}$ and *Crhr1*$_{VTA}$ neurons did not differ in sIPSC frequency (**Figure 11F**), suggesting that these subpopulations share similar mechanisms of presynaptic inhibitory transmission. However, compared with *Crhr1*$_{VTA}$ neurons, *Cck*$_{VTA}$ neurons showed greater sIPSC amplitude (**Figure 11G**), indicating that these subpopulations differ in their postsynaptic mechanisms of inhibitory synaptic transmission. Finally, we asked if there is a difference in rebound spiking following injection of a hyperpolarizing current between *Cck*$_{VTA}$ and *Crhr1*$_{VTA}$ neurons. *Cck*$_{VTA}$ neurons showed a shorter latency to spike and a faster membrane potential rise time following the offset of a hyperpolarizing step compared to *Crhr1*$_{VTA}$ neurons (**Figure 11H-11J**). Taken together, these results establish distinct intrinsic membrane properties of *Cck*$_{VTA}$ and *Crhr1*$_{VTA}$ neurons, which could contribute to their distinct activity patterns *in vivo*.

### *3.2.2 Functional optogenetic characterization of inhibitory and disinhibitory inputs to CckVTA and Crhr1VTA populations*

Diverse inhibitory and disinhibitory connections play important roles in the regulation of VTA dopamine neuron activity and motivated behavior (Morales and Margolis, 2017). Previous work has established that VTA GABA neurons directly control VTA dopamine neuron excitability and ongoing motivated behavior (Van Zessen et al., 2012). Additionally, two prominent GABAergic inputs to the VTA from the lateral hypothalamus (LH) and nucleus accumbens medial shell (NAc mshell) form disinhibitory connections with VTA dopamine neurons via the VTA GABA population and differentially regulate dopamine neuron activity, immediate early gene activation, and motivated behavior (Nieh et al., 2016; Yang et al., 2018; Soden et al., 2020; Simon et al., 2023). However, how VTA GABAergic neurons and GABAergic inputs to the VTA regulate the activity of distinct dopamine subpopulations remains unresolved.

We hypothesized that activation of VTA GABA neurons, LH GABA neurons, or NAc mshell GABA neurons would drive distinct response profiles in *Cck*$_{VTA}$ and *Crhr1*$_{VTA}$ dopamine neurons. To test this possibility, we photostimulated either Vgat$_{VTA}$ neurons, LH GABA neurons, or NAc mshell GABA neurons while recording the neural activity of VTA dopamine subpopulations. First, we injected *Cck*-Cre::*Vgat*-Flp or *Crhr1*-

Cre::*Vgat*-Flp mice with an AAV carrying Flp-dependent ChrimsonR-tdTomato in $Vgat_{VTA}$ neurons and an AAV carrying Cre-dependent GCaMP6m in either $Cck_{VTA}$ and $Crhr1_{VTA}$ neurons in the VTA and implanted an optic fiber for dual recording and stimulation above the VTA (**Figure 12A**; **Figure 10A**). In freely moving mice, we photostimulated the $Vgat_{VTA}$ population with red light (20 Hz or 40 Hz, 3-s duration) and observed a significant decrease in GCaMP fluorescence relative to the pre-stimulation period in both $Cck_{VTA}$ and $Crhr1_{VTA}$ populations (**Figure 12B**). However, compared to the $Cck_{VTA}$ population, the $Crhr1_{VTA}$ population showed a larger amplitude inhibitory response (**Figure 12B**). This suggests that local inhibition may control the activity of $Crhr1_{VTA}$ neurons more strongly *in vivo*.

We next examined how stimulation of the LH GABA or NAc mshell GABA population drives activity in VTA dopamine subpopulations. Using a similar strategy, we expressed Flp-dependent ChrimsonR-tdTomato in either LH GABA neurons or NAc mshell GABA neurons and GCaMP6m in either $Cck_{VTA}$ or $Crhr1_{VTA}$ neurons and implanted an optic fiber for stimulation above the LH or NAc mshell and an optic fiber for recording above the VTA (**Figure 12C**; **Figure 12E**; **Figure 10B-10E**). We found that photostimulation of LH GABA strongly activated both VTA dopamine populations (**Figure 12D**). In contrast, photostimulation of NAc mshell GABA evoked a sustained activation only in the $Cck_{VTA}$ population at both stimulation frequencies (**Figure 12F**). Thus, $Cck_{VTA}$ and $Crhr1_{VTA}$ populations respond differentially to stimulation of inhibitory VTA GABAergic and disinhibitory NAc mshell-VTA GABAergic inputs. Taken together, these findings support a model in which differential inhibitory connectivity among dopamine subpopulations contributes to heterogeneous response profiles *in vivo*.

*3.2.3 Mapping brain-wide monosynaptic inputs to VTA dopamine subpopulations*

VTA dopamine neurons receive synaptic input from numerous brain regions (Watabe-Uchida et al., 2012; Ogawa et al., 2014; Faget et al., 2016; Chung et al., 2017) and distinct VTA dopamine projection populations are differentially regulated by multiple upstream regions (Lammel et al., 2012, Beier et al., 2015). We hypothesized that $Cck_{VTA}$ neurons and $Crhr1_{VTA}$ neurons receive distinct patterns of monosynaptic input across the whole brain. To test this, we compared the relative density of brain-wide monosynaptic inputs to $Cck_{VTA}$ and $Crhr1_{VTA}$ populations using rabies virus-based transsynaptic retrograde tracing (Sun et al., 2014) paired with tissue clearing and light sheet fluorescent microscopy (LSFM). AAV-syn-DIO-TC66T-2A-eGFP-2A-oG was injected into the VTA of *Cck*-Cre or *Crhr1*-Cre mice followed by

injection of EnvA-SADΔG-RV-DsRed 14 days later (**Figure 13A**). After 9 days, intact brains were optically cleared and imaged using LSFM (**Figure 13A**). Starter cell populations in the VTA were identified based on eGFP and DsRed coexpression (**Figure 14A**). Transsynaptically labeled neurons were identified based on DsRed-only expression (**Figure 14B**). To quantify the anatomical distribution of input cells, we used a modified ClearMap pipeline (Renier et al., 2016; Madangopal et al., 2022) for brain atlas registration and automated cell detection. For both *Cck*$_{VTA}$ and *Crhr1*$_{VTA}$ starter cell populations, DsRed-positive input cells were found across the brain (**Figure 13B-13D**; **Figure 14B**; **Figure 14D**; **Figure 15A-15C**). While the total number input cells varied across mice, the number of starter cells and input cells was roughly proportional (**Figure 14E**). Cell counts across all brain regions were normalized to the total number of input cells for each mouse to account for variability in the total number of labeled neurons.

We visualized the brain-wide cellular inputs of *Cck*$_{VTA}$ and *Crhr1*$_{VTA}$ populations by assessing the mean cell density per voxel (**Figure 13C, first and third panels**), and their significant group differences (**Figure 13C, second and fourth panels**). An orthogonal analysis was also conducted on brain atlas-segmented counts with group mean statistical comparisons made on a region-by-region basis (**Figure 13D-13E**). The overall anatomy of identified input regions were largely consistent with previous input-mapping studies of VTA dopamine neurons (Watabe-Uchida 2012). For example, both dopamine populations received large proportions of their total input from the LH, periaqueductal gray (PAG), superior colliculus (SC), and dorsal raphe (DR) (**Figure 13C-8E**). However, we found significant differences in input density from multiple regions in the striatum, pallidum, amygdala, hippocampus, hypothalamus, midbrain, and hindbrain (**Figure 13C-8E**; Supplementary Table 1). In the striatum, the NAc shell predominantly contained *Cck*$_{VTA}$ input neurons, whereas dorsal striatum predominantly contained *Crhr1*$_{VTA}$ input neurons (**Figure 13C-13E**). Thus, *Cck*$_{VTA}$ neurons have reciprocal connections with their NAc projection target, whereas *Crhr1*$_{VTA}$ neurons do not. In pallidal areas, the ventral pallidum (VP) was primarily a source of *Cck*$_{VTA}$ input neurons, whereas dorsal globus pallidus conversely contained inputs prefrentially to *Crhr1*$_{VTA}$ neurons (**Figure 13C-13E**). In more posterior regions, we found that the central amygdala (CeA) predominantly contained *Crhr1*$_{VTA}$ input neurons, whereas the hippocampus connected predominantly to *Cck*$_{VTA}$ neurons (**Figure 13C-13E**). A variety of septal regions including the medial septal nucleus (MS), diagonal band (DB) and hypothalamic regions including medial preoptic (MPO) and lateral preoptic (LPO) areas, LH and posterior

hypothalamic nuclei contained significantly more *Cck*$_{VTA}$ input neurons (**Figure 13C-13E**). *Crhr1*$_{VTA}$ neurons received significantly more input from zona incerta (ZI), and multiple midbrain and hindbrain regions (e.g., medial reticular formation (MRF), SC, PAG, substantia nigra pars reticular part, pontine reticular nucleus, and cuneiform nucleus) (**Figure 13C-13E**).

We additionally clustered brain-wide input differences between *Cck*$_{VTA}$ and *Crhr1*$_{VTA}$ neurons into canonical functional networks (Xu et al., 2022), and found that many were implicated in sensory and motor processing, sensory-motor integration, motivation and action, cognitive processing, and affective processing (**Figure 13E**; see **Methods**). Interestingly, we found that *Cck*$_{VTA}$ neurons received preferential inputs from brain regions involved in motivation and action selection (**Figure 13E**), whereas *Crhr1*$_{VTA}$ neurons received preferential inputs from brain regions involved in sensory-motor integration and affect (**Figure 13E**). Thus, the distinct input patterns of *Cck*$_{VTA}$ and *Crhr1*$_{VTA}$ subpopulations are anatomically widespread with functional relevance inherent across multiple brain systems. Taken together, these results suggest that *Cck*$_{VTA}$ and *Crhr1*$_{VTA}$ subpopulations integrate distinct types of information from upstream inputs and reveal a potential mechanism for a larger diversification of anatomically and functionally specialized inputs to VTA subpopulations.

### 3.3 Discussion

The endogenous phasic responses of VTA dopamine neurons during behavior are likely largely driven by excitatory VTA inputs (Chergui et al., 1993; Zweifel et al., 2009). Consistent with the differences we observed in baseline neural activity during periods of task-related behavioral inactivity between *Cck*$_{VTA}$ and *Crhr1*$_{VTA}$ populations, our *ex vivo* electrophysiological results reveled that these dopamine subpopulations displayed distinct intrinsic properties that may regulate their endogenous activity. Specifically, the increased baseline excitability of *Cck*$_{VTA}$ neurons could contribute to their sustained increase in activity observed during multiple behaviors and increased baseline calcium transient width and amplitude. Additionally, we observed a greater level of spontaneous postsynaptic inhibitory transmission in *Cck*$_{VTA}$ neurons. The amplitude of spontaneous inhibitory postsynaptic currents is correlated with the strength of inhibitory synapses onto the postsynaptic neuron (Segal, 2010; Glasgow et al., 2019). This could be due to multiple mechanisms including differences in the number, location, or subunit composition of GABA receptors

(Farrant et al., 2007; Dixon et al., 2014). Distinct inhibitory synaptic transmission mechanisms in dopamine subpopulations may underlie specific aspects of their different response profiles *in vivo*.

A prominent finding of our study is that $Vgat_{VTA}$ neuron activation suppressed the activity of $Crhr1_{VTA}$ neurons more strongly than that of $Cck_{VTA}$ neurons. This finding is consistent with the observation that $Cck_{VTA}$ and $Crhr1_{VTA}$ neurons display distinct intrinsic properties. Previous input mapping studies have revealed that VTA dopamine and VTA GABA neurons receive inhibitory input from many of the same brain regions including LH, NAc, PAG, and DRN (Morales and Margolis, 2017; Yang et al., 2018). Recent studies have shown that specific GABAergic projections from the LH and NAc are important for behavioral activation and motivation, respectively (Lammel et al., 2012; Yang et al., 2018; Nieh et al., 2016). Interestingly, our functional optogenetic experiments revealed that NAc shell GABA activation disinhibits $Cck_{VTA}$ neurons selectively. This dedicated NAc shell GABA-VTA GABA-$Cck_{VTA}$ dopamine disinhibitory pathway could provide a mechanism by which information about motivational salience reflected in NAc shell MSN activity drives activity in $Cck_{VTA}$ neurons during goal-directed actions. The observation that LH GABA provides a similarly strong disinhibitory drive onto both $Cck_{VTA}$ and $Crhr1_{VTA}$ neurons is consistent with previous findings that the LH GABA-VTA GABA-VTA dopamine circuit plays a broader role in positive reinforcement and behavioral activation across a wide range of motivated behaviors (Nieh et al., 2016). Further, these results are consistent with the hypothesis that VTA GABA neurons are heterogeneous in their afferent connectivity and in their synaptic connectivity with VTA dopamine subpopulations. Taken together, these findings support a model in which dopamine subpopulations are embedded in distinct inhibitory and disinhibitory circuits which contributes to their distinct response profiles *in vivo*.

Given the observed heterogeneous activity dynamics and functional roles of $Crhr1_{VTA}$ and $Cck_{VTA}$ neurons during motivated behavior, we hypothesized that these populations receive distinct upstream monosynaptic inputs. Consistent with previous input mapping studies of VTA dopamine neurons, we identified ~100 brain regions connected to $Crhr1_{VTA}$ and $Cck_{VTA}$ neurons, the majority of which were common to both cell types. Interestingly, $Crhr1_{VTA}$ neurons receive a preferential density of inputs from brain regions involved in sensory-motor integration including dorsal striatum, globus pallidus, zona incerta, and superior colliculus. By contrast, $Cck_{VTA}$ neurons receive a higher density of inputs from brain regions linked to motivation and action including NAc shell, ventral pallidum, and LH. Prior work has

demonstrated that information about reward outcome, expectation, and prediction is distributed across VTA input neurons in regions such as the LH, dorsal and ventral striatum, rostromedial tegmental nucleus, and ventral pallidum among others (Tian e al., 2016). Further, activity in NAc shell projection neurons has been shown to reflect motivation during behavior (Castro et al., 2019; Floresco, 2015). Our results indicating differential monosynaptic input density from these regions to *Crhr1*$_{VTA}$ and *Cck*$_{VTA}$ populations suggest that non-uniform integration of reward-related information contributes to their distinct roles in learning and motivation.

### 3.4 Methods

#### Surgery

Mice (6-8 weeks) were anesthetized with isoflurane (1.5 – 4%) and head-fixed for stereotaxic (David Kopf Instruments) survival surgery. Stereotactic coordinates were standardized relative to Bregma and Lambda distance and an injection syringe was used to inject 0.5 µL of virus at a rate of 0.25 µL/min. Mice recovered from surgery for at least two weeks prior to behavioral testing.

#### *Dual optogenetic stimulation and fiber photometry recording*

For dual stimulation and recording experiments of VTA GABA neurons and VTA dopamine subpopulations, 0.5 µL of equal parts AAV1-CAG-FlpX-ChrimsonR-tdTomato and AAV1-DIO-GCaMP6m was injected unilaterally in to the VTA (A/P: -3.25 mm, M/L: -0.5 mm, D/V: -4.5 mm). Following the virus injection, a fiber optic cannula (400 µm) was implanted 0.5 mm above the VTA.

For dual stimulation and recording experiments of LH GABA neurons and VTA dopamine subpopulations, 0.5 µL of AAV1-CAG-FlpX-ChrimsonR-tdTomato was injected unilaterally in to the LH (A/P: -1.35 mm, M/L: -1.0 mm, D/V: -5.0 mm) and AAV1-DIO-GCaMP6m was injected unilaterally in the VTA (A/P: -3.25 mm, M/L: ±0.5 mm, D/V: -4.5 mm). Following the virus injection, a fiber optic cannula (200 µm) was implanted 0.5 mm above the LH at an angle of 5 degrees and a fiber optic cannula (400 µm) was implanted above the VTA.

For dual stimulation and recording experiments of NAc medial shell GABA neurons and VTA dopamine subpopulations, 0.5 µL of AAV1-CAG-FlpX-ChrimsonR-tdTomato was injected unilaterally in to the NAc

medial shell (A/P: 1.25 mm, M/L: -0.6 mm, D/V: -4.6 mm) and AAV1-DIO-GCaMP6m was injected unilaterally in the VTA (A/P: -3.25 mm, M/L: ±0.5 mm, D/V: -4.5 mm). Following the virus injection, a fiber optic cannula (200 µm) was implanted 0.5 mm above the NAc medial shell and a fiber optic cannula (400 µm) was implanted above the VTA.

***Ex vivo slice electrophysiology***

For electrophysiology experiments, 0.5 µL of AAV1-DIO-YFP was injected bilaterally into the VTA (A/P: -3.25 mm, M/L: -0.5 mm, D/V: -4.5 mm).

***Rabies retrograde tracing***

For the retrograde tracing experiment, 0.5 µL of AAV-syn-DIO-TC66T-2A-eGFP-2A-oG was injected bilaterally into the VTA (A/P: -3.45 mm, M/L: ±0.5 mm, D/V: -4.5 mm). 14 days later, 0.5 µL of EnvA-SADΔG-RV-DsRed was injected bilaterally into the VTA (A/P: -3.45 mm, M/L: ± 0.5 mm, D/V: -4.5 mm).

**Ex vivo electrophysiology**

Horizontal VTA sections (200 µm) were prepared in a NMDG cutting solution (92 NMDG mM, 2.5 KCl mM, 1.25 $NaH_2PO_4$ mM, 30 $NaHCO_3$ mM, 20 HEPES mM, 25 glucose mM, 2 thiourea mM, 5 Na-ascorbate mM, 3 Na-pyruvate mM, 0.5 $CaCl_2$ mM, 10 $MgSO_4$ mM, pH 7.3–7.4). Then, sections were incubated for ~12 min in the same solution at 32°C in a water bath. Slices were then transferred to a HEPES-aCSF solution (92 NaCl mM, 2.5 KCl mM, 1.25 mM $NaH_2PO_4$ mM, 30 $NaHCO_3$ mM, 20 HEPES mM, 25 glucose mM, 2 thiourea mM, 5 Na-ascorbate mM, 3 Na-pyruvate mM, 2 $CaCl_2$ mM, 2 $MgSO_4$ mM) at room temperature. Slices recovered for an additional 60 min.

Whole-cell, patch-clamp recordings were acquired using the Axopatch 700B amplifier (Molecular Devices) at a sampling frequency of 10 kHz and filtering at 1 kHz. eYFP-positive cells were visualized using fluorescence for recording with electrodes at 3–5 MΩ. Excitability recordings were made in an aCSF solution (126 NaCl mM, 2.5 KCl mM, 1.2 $NaH_2PO_4$ mM, 1.2 $MgCl_2$ mM, 11 D-glucose mM, 18 $NaHCO_3$ mM, 2.4 $CaCl_2$ mM) at 32°C and for sIPSC recordings the solution was supplemented with 2mM of kynurenic acid. The aCSF solution was perfused over slices at ~2 ml/min.

To determine excitability, cells were patched with electrodes were filled with an internal solution (in mM: 130 potassium gluconate, 10 HEPES, 5 NaCl, 1 EGTA, 5 Mg-ATP, 0.5 Na-GTP, pH 7.3, 280 mOsm). Current-voltage curves were generated by recording in current-clamp mode and injecting steps of current (0-80-pA, 10-pA steps, 1-s) (both at resting membrane potential and at -60 mV). For sIPSCs, cells were patched with electrodes were filled with an internal solution (in mM: 135 KCl, 12 NaCl, 0.5 EGTA, 10 HEPES, 2.5 Mg-ATP, 0.25 sodium GTP, pH 7.3, 280 mOsm) and held at -60 mV. Recordings were analyzed using Clampfit (Molecular Devices). Excitability was calculated as the total number of events during each current step detected using the Event Detection function in Clampfit (50-ms before and 150-ms after action potential peak). The first action potential evoked from a 20-pA current injection while holding at -60mV were detected using the Event Detection threshold function in Clampfit. Hyperpolarization-induced rebound activity was assessed by injecting a hyperpolarizing step of current (-120-pA, 1-s). sIPSCS were detected using the Event Detection template function in Clampfit to determine frequency and amplitude.

**Retrograde tracing**

Mice were perfused and brains were collected for imaging (see Immunohistochemistry) nine days following rabies virus injection (see Surgery). Then we optically cleared whole-brain samples using the SmartClear full active pipeline protocol (LifeCanvas Technologies, v5.05) for aqueous-based brain clearing and mounting as described recently (Szelenyi et al, 2023). Native fluorescent signals from aqueous-based cleared brains were imaged horizontally using the SmartSPIM LSFM (LifeCanvas Technologies) at 4 µm near-isotropic pixel resolution in 2 channels: 488-nm for registration signal and helper virus-infected cells, and 563-nm for rabies virus-infected inputs cells. Laser power and acquisition settings were held constant for all genetic groups and their individuals. Cleared whole-brain samples were then placed in phosphate-buffered saline (PBS) for at least two 24 hour washes at room temperature. Whole-brain samples were then mounted in 4% agarose and sectioned into 50 µm sections using a vibratome for posthoc immunostaining of free-floating sections (see Immunohistochemistry and image analysis).

**Whole-brain image processing and quantification**

We used ImageJ software to crop whole-brain image stacks, transform from the horizontal to coronal plane, and export images as TIFF files for whole-brain analysis. Brains were registered to the Unified brain atlas and segmented DsRed cell counts were partitioned into regions with Unified atlas labels (Chon et al., 2019). For brain atlas registration and automated cell detection a previously described and modified ClearMap analysis pipeline (Renier et al., 2016; Madangopal et al., 2022) was used with minor adjustments. Accordingly, cell segmentation was automated using the Spot Detection function. The number of DsRed-positive input neurons per brain region was normalized to the total volume of the brain region from the reference atlas to calculate cell density per region (cells/$mm^3$). 3D renders of input cell location in atlas space were generated using the 'Wholebrain' (Furth et al., 2018) and 'SMART' (Jin et al., 2022) packages in R.

### 3.4.1 Quantification and statistical analysis

GraphPad Prism, Python, and MATLAB. All statistical tests were two-tailed. Sample sizes were not predetermined using statistical methods. For data from two groups, the paired *t*-test, unpaired *t*-test, and Mann-Whitney *U* test were used where appropriate. For data from three or more groups, one-way ANOVA and one-way repeated-measures ANOVA followed by multiple-comparisons tests (Tukey's multiple comparisons test, Bonferroni's multiple comparisons test, two-stage linear step-up procedure of Bejamini, Krieger and Yekutieli) were used to determine any statistically significant differences between groups. For data from three or more groups and across multiple conditions, two-way ANOVA and two-way repeated-measures ANOVA followed by multiple-comparisons tests (Šídák's multiple comparisons test, two-stage linear step-up procedure of Bejamini, Krieger and Yekutieli) were used where appropriate. For correlation analysis, the Pearson correlation coefficient was used. For all tests, a significance threshold of 0.05 was used. See supplementary Table 1 for detailed statistical results.

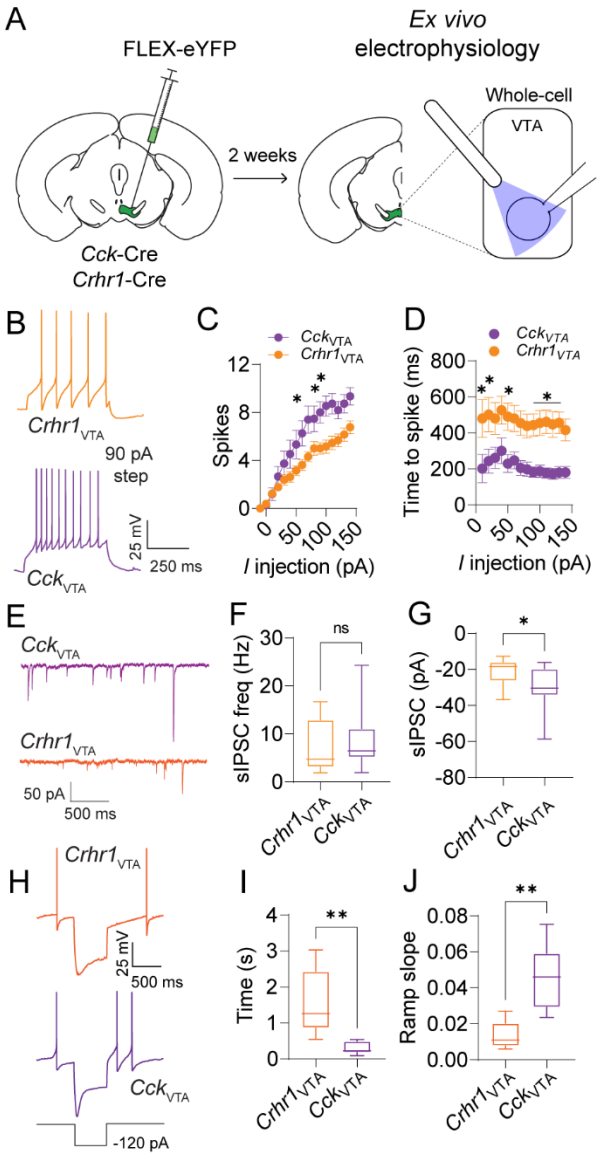


**Figure 11. Baseline neurophysiological properties *Crhr1*$_{VTA}$ and *Cck*$_{VTA}$ neurons**

(A) Schematic of the viral injection strategy and *ex vivo* electrophysiology recordings.

(B) Representative evoked excitability traces from *Crhr1*$_{VTA}$ (orange) or *Cck*$_{VTA}$ (magenta) neurons (90 pA current injection).

(C) Current-voltage plot for *Crhr1*$_{VTA}$ (orange) and *Cck*$_{VTA}$ (magenta) neurons (n = 13-15 cells) showing mean number of evoked spikes per current injection level. Bars and error bars indicate mean ± SEM across cells.

(D) Mean spike latency following current injection for *Crhr1*$_{VTA}$ (orange) and *Cck*$_{VTA}$ (magenta) neurons (n = 13-15). Bars and error bars indicate mean ± SEM across cells.

(E) Representative spontaneous inhibitory postsynaptic current (sIPSC) traces from *Crhr1*$_{VTA}$ (orange) or *Cck*$_{VTA}$ (magenta) neurons.

(F) Mean sIPSC frequency for *Crhr1*$_{VTA}$ (orange) and *Cck*$_{VTA}$ (magenta) neurons (n = 13-15 cells).

(G) Mean sIPSC amplitude for *Crhr1*$_{VTA}$ (orange) and *Cck*$_{VTA}$ (magenta) neurons (n = 13-15 cells).

(H) Representative traces of rebound spiking from *Crhr1*$_{VTA}$ (orange) or *Cck*$_{VTA}$ (magenta) neurons following injection of a -120 pA hyperpolarizing current.

(I) Mean time to first spike following hyperpolarization for *Crhr1*$_{VTA}$ (orange) and *Cck*$_{VTA}$ (magenta) neurons (n = 5-6 cell)

Mean ramp slope prior to first spike following hyperpolarization for *Crhr1*$_{VTA}$ (orange) and *Cck*$_{VTA}$ (magenta) neurons (n = 5-6 cells, see Supplementary Table 1 for statistical values).

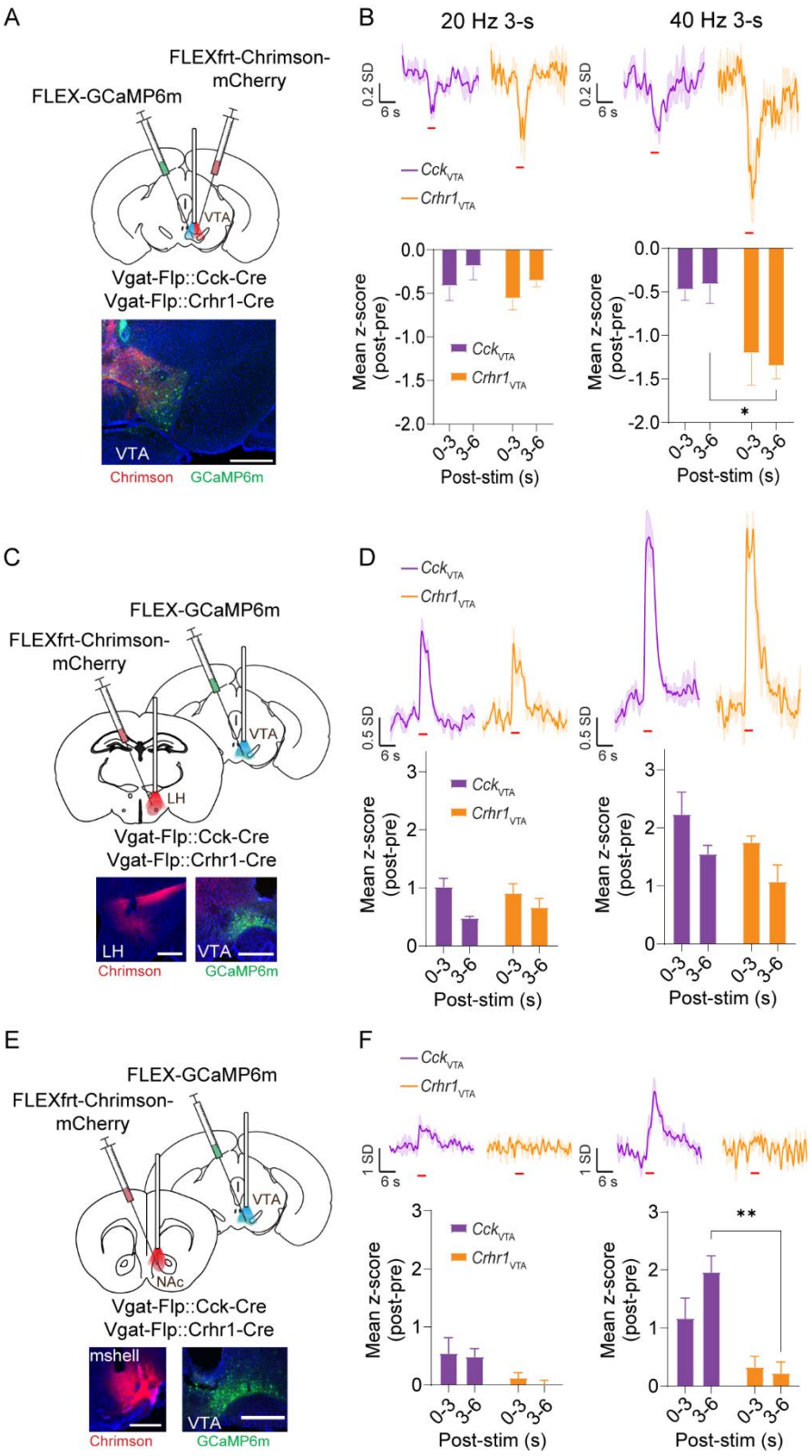


**Figure 12. Functional optogenetic characterization of inhibitory and disinhibitory inputs to *Crhr1*$_{VTA}$ and *Cck*$_{VTA}$ populations**

(A) Schematic of viral injection strategy. Vgat-Flp::*Cck*-Cre or Vgat-Flp::*Crhr1*-Cre mice were injected with Flp-dependent Chrimson and Cre-dependent GCaMP into the VTA. An optical fiber for dual stimulation and recording was implanted above VTA. Scale bar: 500 µm.

(B) Z-scored GCaMP fluorescence aligned to $Vgat_{VTA}$ stimulation in $Cck_{VTA}$ (n = 3 mice, 6 sessions) and $Crhr1_{VTA}$ (n = 3 mice, 6 sessions) groups (top). Average z-scored GCaMP fluorescence during stimulation and post-stimulation periods for $Cck_{VTA}$ (n = 3 mice, 10 sessions) and $Crhr1_{VTA}$ (n = 3 mice, 6 sessions) groups (bottom). Bars and error bars indicate mean ± SEM across mice.

(C) Schematic of viral injection strategy. Vgat-Flp::*Cck*-Cre or Vgat-Flp::*Crhr1*-Cre mice were injected with Flp-dependent Chrimson into the LH and Cre-dependent GCaMP into the VTA. Stimulation and recording fibers were implanted above the LH and VTA, respectively. Scale bar: 500 µm.

(D) Z-scored GCaMP fluorescence aligned to LH GABA stimulation in $Cck_{VTA}$ (n = 5 mice, 10 sessions) and $Crhr1_{VTA}$ (n = 3 mice, 6 sessions) groups (top). Average z-scored GCaMP fluorescence during stimulation and post-stimulation periods for $Cck_{VTA}$ (n = 5 mice, 10 sessions) and $Crhr1_{VTA}$ (n = 3 mice, 6 sessions) groups (bottom). Bars and error bars indicate mean ± SEM across mice.

(E) Schematic of viral injection strategy. Vgat-Flp::*Cck*-Cre or Vgat-Flp::*Crhr1*-Cre mice were injected with Flp-dependent Chrimson into the NAc mshell and Cre-dependent GCaMP into the VTA. Stimulation and recording fibers were implanted above the NAc mshell and VTA, respectively. Scale bar: 500 µm.

(F) Z-scored GCaMP fluorescence aligned to NAc shell stimulation in $Cck_{VTA}$ (n = 3 mice, 6 sessions) and $Crhr1_{VTA}$ (n = 3 mice, 6 sessions) groups (top). Average z-scored GCaMP fluorescence during stimulation and post-stimulation periods for $Cck_{VTA}$ (n = 3 mice, 6 sessions) and $Crhr1_{VTA}$ (n = 3 mice, 6 sessions) groups (bottom). Bars and error bars indicate mean ± SEM across mice (see Supplementary Table 1 for statistical values).

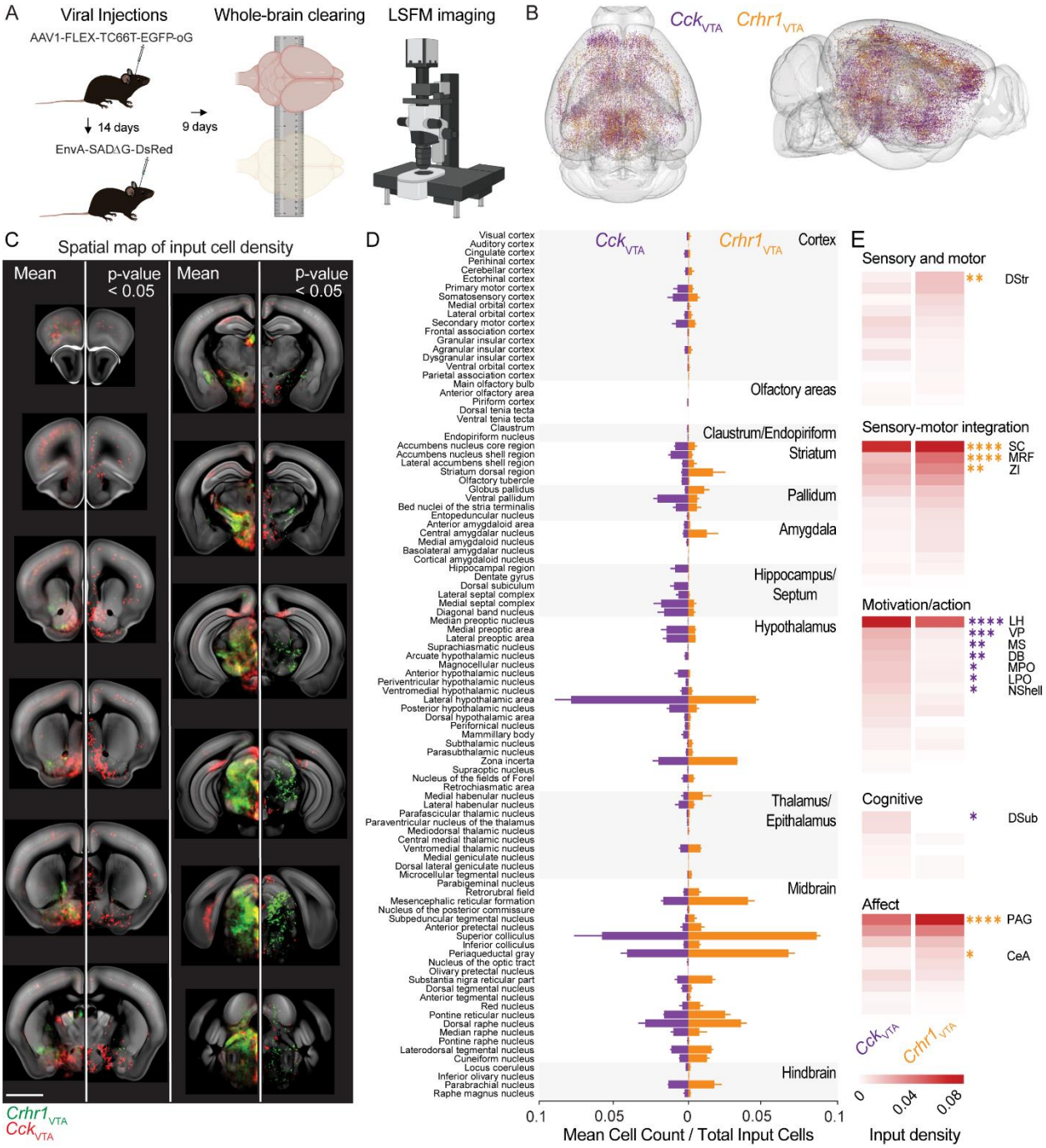


**Figure 13. Whole-brain mapping of inputs to *Crhr1*$_{VTA}$ and *Cck*$_{VTA}$ neurons**

(A) Schematic of viral injection strategy, whole-brain clearing, and light sheet fluorescence microscopy (LSFM). Cre-dependent helper virus (AAV-syn-DIO-TC66T-2A-eGFP-2A-oG) was injected into the VTA of *Cck*-Cre or *Crhr1*-Cre mice. Two weeks later, rabies virus (EnvA-SADΔG-RV-DsRed) was injected in to the VTA. Nine days later, intact brains were cleared and imaged.

(B) Location of input cells to *Cck*$_{VTA}$ and *Crhr1*$_{VTA}$ neurons in example mice.

(C) Voxelized heatmap of input cell density in coronal sections across the whole-brain. Mean density of DsRed-positive cells per mm$^3$ across mice (left panels). Voxelized results of group one-way ANOVA pairwise comparison (right panels) (n = 3 mice). Scale bar: 2 mm.

(D) Mean number of input cells normalized to total number of input cells for all input regions for *Cck*$_{VTA}$ (left) and *Crhr1*$_{VTA}$ (right) groups (n = 3 mice).
(E) Heatmap of group pairwise comparison one-way ANOVA results for clustered input regions for *Cck*$_{VTA}$ (left) and *Crhr1*$_{VTA}$ (right) groups (see Supplementary Table 1 for statistical values).

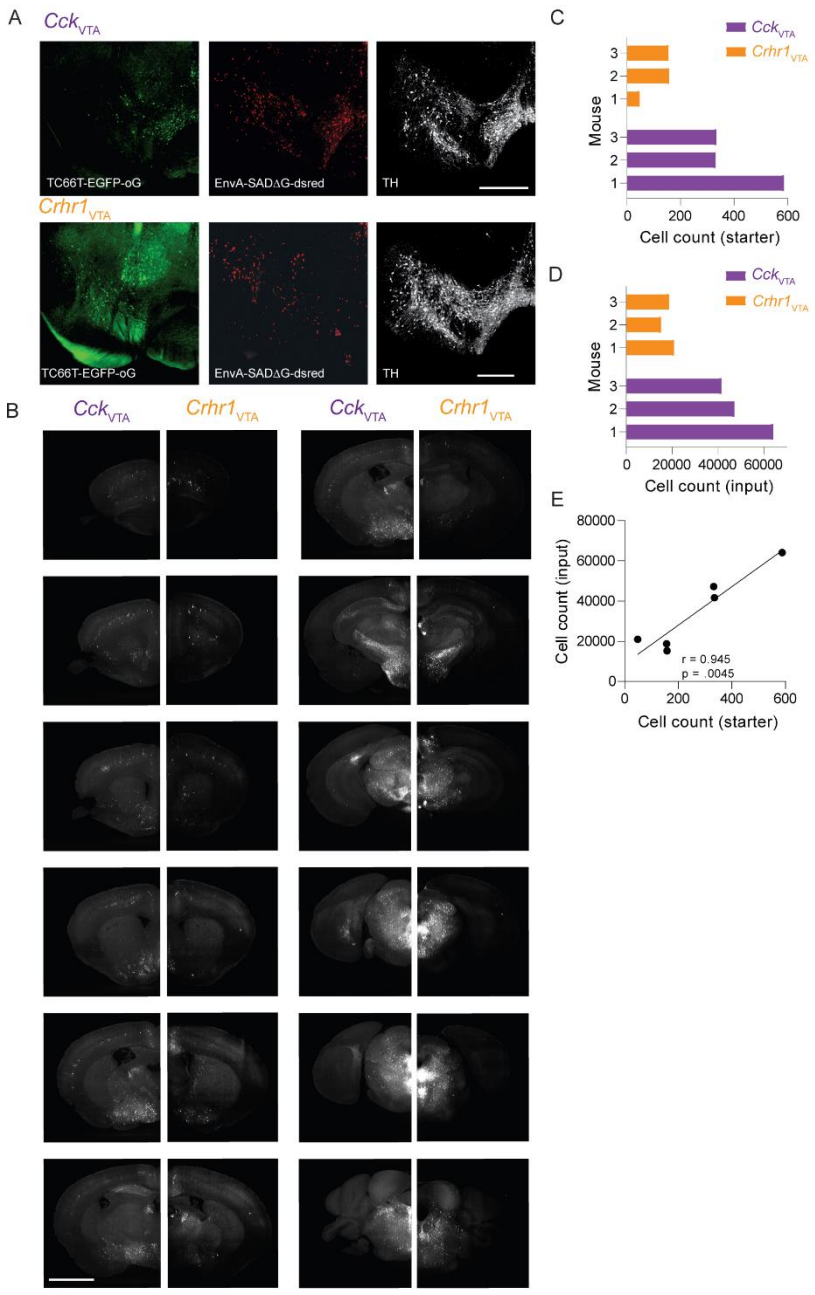


**Figure 14. Further characterization of whole-brain input mapping to *Crhr1*$_{VTA}$ and *Cck*$_{VTA}$ neurons, related to Figure 8**

(A) Representative images of *Cck*$_{VTA}$ (top) and *Crhr1*$_{VTA}$ (bottom) starter cell populations. Example histology images from the VTA showing staining for helper virus (AAV-syn-DIO-TC66T-2A-eGFP-2A-oG) (green), rabies virus (EnvA-SADΔG-RV-DsRed) (red), and tyrosine hydroxylase (white). Scale bar: 500 µm.

(B) Representative images of *Cck*$_{VTA}$ (left) and *Crhr1*$_{VTA}$ (right) input cells. Scale bar: 2 mm.

(C) Number of starter cells per mouse.

(D) Number of labeled input neurons per mouse.

(E) Relationship between numbers of starter and input neurons. Correlation coefficient (r) and p-value on the bottom right of the plot (see Supplementary Table 1 for statistical values).

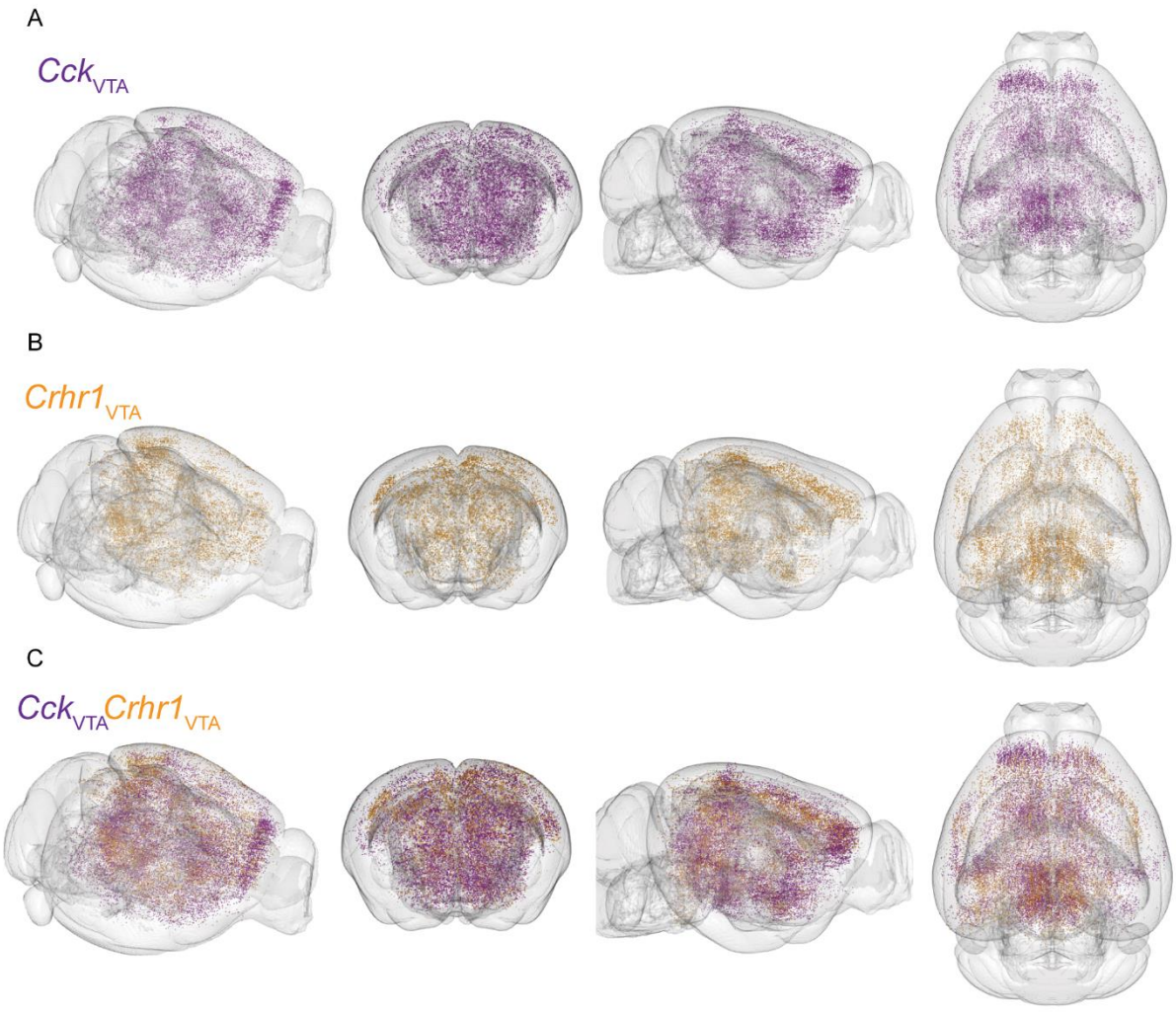


**Figure 15. Further characterization of whole-brain input mapping to *Crhr1*$_{VTA}$ and *Cck*$_{VTA}$ neurons, related to Figure 8**

(A) Location of input cells to *Cck*$_{VTA}$ neurons in example mice.
(B) Location of input cells to *Crhr1*$_{VTA}$ neurons in example mice.
(C) Location of input cells to *Cck*$_{VTA}$ and *Crhr1*$_{VTA}$ neurons in example mice.

## Supplementary Table 2

| Figure | Description | Sample size | Statistical test | Test Statistic | *p Value* | Significance | Multiple comparisons correction | Adjusted *p* Values |
|---|---|---|---|---|---|---|---|---|
| 6C | Difference in mean number of spikes between CckVTA and Crhr1VTA groups across different current injections | 13 cells from Crhr1VTA group, 15 cells from CckVTA group | Two-way RM ANOVA | F (15, 390) = 3.054 | 0.0001 | *** | Šídák's multiple comparisons test | -10, p >0.9999, 0, p >0.9999, 10, p >0.9999, 20, p = 0.9996, 30, p = 0.9668, 40, p = 0.6507, 50, p = 0.4361, 60, p = 0.1553, 70, p = 0.045, 80, p = 0.2425, 90, p = 0.0594, 100, p = 0.018, 110, p = 0.0257, 120, p = 0.2206, 130, p = 0.1857, 140, p = 0.1928 |
| 6D | Difference in mean latency to spike between CckVTA and Crhr1VTA groups across different current injections | 13 cells from Crhr1VTA group, 15 cells from CckVTA group | Two-way RM ANOVA | F (13, 338) = 0.1485 | 0.9998 | ns | Šídák's multiple comparisons test | 10, p = 0.0222, 20, p = 0.0463, 30, p = 0.1642, 40, p = 0.1347, 50, p = 0.0425, 60, p = 0.1044, 70, p = 0.0641, 80, p = 0.0816, 90, p = 0.0408, 100, p = 0.0322, 110, p = 0.0168, 120, p = 0.0249, 130, p = 0.0228, 140, p = 0.0991 |
| 6F | Difference in mean sIPSC frequency between CckVTA and Crhr1VTA groups | 10 cells from Crhr1VTA group, 13 cells from CckVTA group | Mann Whitney test | NA | 0.4458 | ns | NA | NA |
| 6G | Difference in mean sIPSC amplitude between CckVTA and Crhr1VTA groups | 10 cells from Crhr1VTA group, 13 cells from CckVTA group | Mann Whitney test | NA | 0.0422 | * | NA | NA |
| 6I | Difference in mean latency to first spike following hyperpolarizing current injection between CckVTA and Crhr1VTA groups across different current injections | 5 cells from Crhr1VTA group, 6 cells from CckVTA group | Mann Whitney test | NA | 0.0043 | ** | NA | NA |
| 6J | Difference in mean ramp slope prior to first spike following hyperpolarizing current injection between CckVTA and Crhr1VTA groups across different current injections | 5 cells from Crhr1VTA group, 6 cells from CckVTA group | Mann Whitney test | NA | 0.0087 | ** | NA | NA |
| 7B | Difference in baseline subtracted mean z-scored fluorescence from DATVTA neurons during 20 Hz photostimulation of VgatVTA neurons | 3 mice from the CckVTA group, 3 mice from the Crhr1VTA group | Two-way ANOVA | F (1, 4) = 0.04479 | 0.8427 | ns | Two-stage linear step-up procedure of Benjamini, Krieger and Yekutieli | CckVTA - Crhr1VTA: 0 - 3, p = 0.4684, 3 - 6, p = 0.4019 |
| 7B | Difference in baseline subtracted mean z-scored fluorescence from DATVTA neurons during 40 Hz photostimulation of VgatVTA neurons | 3 mice from the CckVTA group, 3 mice from the Crhr1VTA group | Two-way ANOVA | F (1, 4) = 0.5564 | 0.4972 | ns | Two-stage linear step-up procedure of Benjamini, Krieger and Yekutieli | CckVTA - Crhr1VTA: 0 - 3, p = 0.056, 3 - 6, p = 0.0207 |

| | | | | | | | | |
|---|---|---|---|---|---|---|---|---|
| 7D | Difference in baseline subtracted mean z-scored fluorescence from DATVTA neurons during 20 Hz photostimulation of LH GABA neurons | 5 mice from the CckVTA group, 3 mice from the Crhr1VTA group | Two-way ANOVA | F (1, 6) = 1.112 | 0.3322 | ns | Two-stage linear step-up procedure of Benjamini, Krieger and Yekutieli | CckVTA - Crhr1VTA: 0 - 3, p = 0.5567, 3 - 6, p = 0.3245 |
| 7D | Difference in baseline subtracted mean z-scored fluorescence from DATVTA neurons during 40 Hz photostimulation of LH GABA neurons | 5 mice from the CckVTA group, 3 mice from the Crhr1VTA group | Two-way ANOVA | F (1, 6) = 1.830e-005 | 0.9967 | ns | Two-stage linear step-up procedure of Benjamini, Krieger and Yekutieli | CckVTA - Crhr1VTA: 0 - 3, p = 0.6873, 3 - 6, p = 0.6843 |
| 7F | Difference in baseline subtracted mean z-scored fluorescence from DATVTA neurons during 20 Hz photostimulation of NAc mshell GABA neurons | 3 mice from the CckVTA group, 3 mice from the Crhr1VTA group | Two-way ANOVA | F (1, 4) = 0.03460 | 0.8615 | ns | Two-stage linear step-up procedure of Benjamini, Krieger and Yekutieli | CckVTA - Crhr1VTA: 0 - 3, p = 0.101, 3 - 6, p = 0.0675 |
| 7F | Difference in baseline subtracted mean z-scored fluorescence from DATVTA neurons during 40 Hz photostimulation of NAc mshell GABA neurons | 3 mice from the CckVTA group, 3 mice from the Crhr1VTA group | Two-way ANOVA | F (1, 4) = 5.456 | 0.0797 | ns | Two-stage linear step-up procedure of Benjamini, Krieger and Yekutieli | CckVTA - Crhr1VTA: 0 - 3, p = 0.0511, 3 - 6, p = 0.0015 |
| 8E | Difference in mean voxelized density of DsRed-positive cells in sensory and motor regions between CckVTA and Crhr1VTA groups | 3 mice from the CckVTA group, 3 mice from the Crhr1VTA group | Two-way ANOVA | F (53, 216) = 4.935 | <0.0001 | **** | Two-stage linear step-up procedure of Benjamini, Krieger and Yekutieli | Striatum dorsal region, p = 0.0064, Substantia nigra reticular part, p = 0.0545, Globus pallidus, p = 0.0666, Ventromedial thalamic nucleus, p = 0.5332, Somatosensory cortex, p = 0.3216, Secondary motor cortex, p = 0.3842, Nucleus of the fields of Forel, p = 0.9555, Primary motor cortex, p = 0.3073, Parasubthalamic nucleus, p = 0.809, Subthalamic nucleus, p = 0.6988, Cerebellar cortex, p = 0.9533, Cingulate cortex, p = 0.7488 |
| 8E | Difference in mean voxelized density of DsRed-positive cells in sensory-motor integration regions between CckVTA and Crhr1VTA groups | 3 mice from the CckVTA group, 3 mice from the Crhr1VTA group | Two-way ANOVA | F (53, 216) = 4.935 | <0.0001 | **** | Two-stage linear step-up procedure of Benjamini, Krieger and Yekutieli | Superior colliculus, p <0.0001, Mesencephalic reticular formation, p <0.0001, Zona incerta, p = 0.0044, Pontine reticular nucleus, p = 0.0602, Laterodorsal tegmental nucleus, p = 0.3798, Cuneiform nucleus, p = 0.141, Anterior pretectal nucleus, p = 0.2909, Red nucleus, p = 0.41, Inferior colliculus, p = 0.3376, Retrorubral field, p = 0.3632, Subpeduncular tegmental nucleus, p = 0.6621, Nucleus of the fields of Forel, p = 0.9555, Parafascicular thalamic nucleus, p = 0.9576 |
| 8E | Difference in mean voxelized density of DsRed-positive cells in motivation/action regions between CckVTA and Crhr1VTA groups | 3 mice from the CckVTA group, 3 mice from the Crhr1VTA group | Two-way ANOVA | F (53, 216) = 4.935 | <0.0001 | **** | Two-stage linear step-up procedure of Benjamini, Krieger and Yekutieli | Lateral hypothalamic area, p <0.0001, Ventral pallidum, p = 0.0009, Medial septal complex, p = 0.0013, Diagonal band nucleus, p = 0.0051, Medial preoptic area, p = 0.0233, Lateral preoptic area, p = 0.027, Accumbens nucleus shell region, p = 0.036, Accumbens nucleus core region, p = 0.3156, Bed nuclei of the stria terminalis, p = 0.5318, Lateral septal complex, p = 0.1867, Ventromedial hypothalamic nucleus, p = 0.6495, Lateral accumbens shell region, p = 0.9561, Perifornical nucleus, p = 0.7836, Periventricular hypothalamic nucleus, p = 0.7284 |
| 8E | Difference in mean voxelized density of DsRed-positive cells in cognitive regions between CckVTA and Crhr1VTA groups | 3 mice from the CckVTA group, 3 mice from the Crhr1VTA group | Two-way ANOVA | F (53, 216) = 4.935 | <0.0001 | **** | Two-stage linear step-up procedure of Benjamini, Krieger and Yekutieli | Dorsal subiculum, p = 0.0325, Hippocampal region, p = 0.0529, Dorsal tegmental nucleus, p = 0.6232, Mammillary body, p = 0.5268, Lateral orbital cortex, p = 0.9182, Agranular insular cortex, p = 0.9034 |
| 8E | Difference in mean voxelized density of DsRed-positive cells in affect regions between CckVTA and Crhr1VTA groups | 3 mice from the CckVTA group, 3 mice from the Crhr1VTA group | Two-way ANOVA | F (53, 216) = 4.935 | <0.0001 | **** | Two-stage linear step-up procedure of Benjamini, Krieger and Yekutieli | Periaqueductal gray, p <0.0001, Dorsal raphe nucleus, p = 0.1537, Parabrachial nucleus, p = 0.3899, Central amygdalar nucleus, p = 0.0458, Medial habenular nucleus, p = 0.1598, Median raphe nucleus, p = 0.5268, Lateral habenular nucleus, p = 0.5158, Raphe magnus nucleus, p = 0.8147, Anterior amygdaloid area, p = 0.7043 |

| | | | | | | | | |
|---|---|---|---|---|---|---|---|---|
| S1B | Difference in mean number of GFP-positive cells in stained VTA histology section with photometry recording fiber tract between DATVTA, CckVTA, Crhr1VTA, and VgatVTA groups | 12 mice from DATVTA group, 8 mice from VgatVTA group, 11 mice from CckVTA group, 11 mice from Crhr1VTA group | Ordinary one-way ANOVA | F (3, 38) = 4.590 | 0.0077 | ** | Tukey's multiple comparisons test | DATVTA vs. VgatVTA, p = 0.0049, DATVTA vs. CckVTA, p = 0.0976, DATVTA vs. Crhr1VTA, p = 0.3257, VgatVTA vs. CckVTA, p = 0.5124, VgatVTA vs. Crhr1VTA, p = 0.212, CckVTA vs. Crhr1VTA, p = 0.9165 |
| S1C | Difference in mean fluorescence of GFP-positive cells in stained VTA histology section with photometry recording fiber tract between DATVTA, CckVTA, Crhr1VTA, and VgatVTA groups | 12 mice from DATVTA group, 8 mice from VgatVTA group, 11 mice from CckVTA group, 11 mice from Crhr1VTA group | Ordinary one-way ANOVA | F (3, 38) = 2.020 | 0.1274 | ns | Tukey's multiple comparisons test | DATVTA vs. VgatVTA, p = 0.1407, DATVTA vs. CckVTA, p >0.9999, DATVTA vs. Crhr1VTA, p = 0.9282, VgatVTA vs. CckVTA, p = 0.1455, VgatVTA vs. Crhr1VTA, p = 0.382, CckVTA vs. Crhr1VTA, p = 0.9247 |
| S1E | Difference in mean transients per minute during baseline photometry recording periods between DATVTA, CckVTA, Crhr1VTA, and VgatVTA groups | 10 mice from DATVTA group, 8 mice from VgatVTA group, 18 mice from CckVTA group, 17 mice from Crhr1VTA group | Ordinary one-way ANOVA | F (3, 50) = 7.981 | 0.0002 | *** | Two-stage linear step-up procedure of Benjamini, Krieger and Yekutieli | CckVTA vs. Crhr1VTA, p <0.0001, CckVTA vs. DATVTA, p = 0.3371, CckVTA vs. VgatVTA, p = 0.0239, Crhr1VTA vs. DATVTA, p = 0.0029, Crhr1VTA vs. VgatVTA, p = 0.1719, DATVTA vs. VgatVTA, p = 0.189 |
| S1F | Difference in mean transient width during baseline photometry recording periods between DATVTA, CckVTA, Crhr1VTA, and VgatVTA groups | 10 mice from DATVTA group, 8 mice from VgatVTA group, 18 mice from CckVTA group, 17 mice from Crhr1VTA group | Ordinary one-way ANOVA | F (3, 50) = 8.855 | <0.0001 | **** | Two-stage linear step-up procedure of Benjamini, Krieger and Yekutieli | CckVTA vs. Crhr1VTA, p <0.0001, CckVTA vs. DATVTA, p = 0.1359, CckVTA vs. VgatVTA, p = 0.2115, Crhr1VTA vs. DATVTA, p = 0.0051, Crhr1VTA vs. VgatVTA, p = 0.0085, DATVTA vs. VgatVTA, p = 0.9279 |
| S1G | Difference in mean transient amplitude during baseline photometry recording periods between DATVTA, CckVTA, Crhr1VTA, and VgatVTA groups | 10 mice from DATVTA group, 8 mice from VgatVTA group, 18 mice from CckVTA group, 17 mice from Crhr1VTA group | Ordinary one-way ANOVA | F (3, 50) = 7.588 | 0.0003 | *** | Two-stage linear step-up procedure of Benjamini, Krieger and Yekutieli | CckVTA vs. Crhr1VTA, p = 0.0019, CckVTA vs. DATVTA, p = 0.6626, CckVTA vs. VgatVTA, p = 0.0014, Crhr1VTA vs. DATVTA, p = 0.0018, Crhr1VTA vs. VgatVTA, p = 0.4414, DATVTA vs. VgatVTA, p = 0.0011 |
| S2A | Difference in latency to peak during reward delivery between DATVTA, CckVTA, Crhr1VTA, and VgatVTA groups | 9 mice from DATVTA group, 8 mice from VgatVTA group, 17 mice from CckVTA group, 13 mice from Crhr1VTA group | Ordinary one-way ANOVA | F (3, 43) = 9.990 | <0.0001 | **** | Bonferroni's multiple comparisons test | CckVTA vs. Crhr1VTA, p >0.9999, CckVTA vs. DATVTA, p >0.9999, CckVTA vs. VgatVTA, p = 0.0002, Crhr1VTA vs. DATVTA, p = 0.9809, Crhr1VTA vs. VgatVTA, p = 0.001, DATVTA vs. VgatVTA, p <0.0001 |
| S2B | Difference in mean z-scored fluorescence during CS period between DATVTA, CckVTA, Crhr1VTA, and VgatVTA groups | 9 mice from DATVTA group, 8 mice from VgatVTA group, 17 mice from CckVTA group, 13 mice from Crhr1VTA group | Ordinary one-way ANOVA | F (3, 42) = 17.92 | <0.0001 | **** | Bonferroni's multiple comparisons test | CckVTA vs. Crhr1VTA, p >0.9999, CckVTA vs. DATVTA, p >0.9999, CckVTA vs. VgatVTA, p <0.0001, Crhr1VTA vs. DATVTA, p >0.9999, Crhr1VTA vs. VgatVTA, p <0.0001, DATVTA vs. VgatVTA, p <0.0001 |
| S2C | Difference in mean z-scored fluorescence during unrewarded port entry period between DATVTA, CckVTA, Crhr1VTA, and VgatVTA groups | 9 mice from DATVTA group, 8 mice from VgatVTA group, 17 mice from CckVTA group, 13 mice from Crhr1VTA group | Ordinary one-way ANOVA | F (3, 42) = 8.768 | 0.0001 | *** | Bonferroni's multiple comparisons test | CckVTA vs. Crhr1VTA, p >0.9999, CckVTA vs. DATVTA, p >0.9999, CckVTA vs. VgatVTA, p = 0.0006, Crhr1VTA vs. DATVTA, p >0.9999, Crhr1VTA vs. VgatVTA, p = 0.002, DATVTA vs. VgatVTA, p = 0.0002 |
| S2D | Difference in mean z-scored fluorescence during CS period between DATVTA, CckVTA, Crhr1VTA, and VgatVTA groups | 9 mice from DATVTA group, 8 mice from VgatVTA group, 17 mice from CckVTA group, 13 mice from Crhr1VTA group | Ordinary one-way ANOVA | F (3, 42) = 9.676 | <0.0001 | **** | Bonferroni's multiple comparisons test | CckVTA vs. Crhr1VTA, p = 0.4956, CckVTA vs. DATVTA, p >0.9999, CckVTA vs. VgatVTA, p = 0.0017, Crhr1VTA vs. DATVTA, p = 0.114, Crhr1VTA vs. VgatVTA, p <0.0001, DATVTA vs. VgatVTA, p = 0.057 |

| | | | | | | | | |
|---|---|---|---|---|---|---|---|---|
| S2E | Difference in mean z-scored fluorescence during CS period between DATVTA, CckVTA, Crhr1VTA, and VgatVTA groups | 9 mice from DATVTA group, 8 mice from VgatVTA group, 17 mice from CckVTA group, 13 mice from Crhr1VTA group | Ordinary one-way ANOVA | F (3, 42) = 12.74 | <0.0001 | **** | Bonferroni's multiple comparisons test | CckVTA vs. Crhr1VTA, p >0.9999, CckVTA vs. DATVTA, p >0.9999, CckVTA vs. VgatVTA, p <0.0001, Crhr1VTA vs. DATVTA, p >0.9999, Crhr1VTA vs. VgatVTA, p <0.0001, DATVTA vs. VgatVTA, p = 0.0002 |
| S2F | Difference in mean z-scored fluorescence during action-cue period between CckVTA and Crhr1VTA groups | 17 mice from CckVTA group, 13 mice from Crhr1VTA group | Unpaired t test | t=2.128, df=28 | 0.0422 | * | NA | NA |
| S2G | Difference in mean correlation coefficient from the time and mean z scored fluorescence during pre-trial initation lever press correlation across day 1 and day 5 of acquisition between CckVTA and Crhr1VTA groups | 17 mice from CckVTA group, 13 mice from Crhr1VTA group | Two-way RM ANOVA | F (1, 28) = 3.388 | 0.0763 | ns | Two-stage linear step-up procedure of Benjamini, Krieger and Yekutieli | Day 1, p = 0.0203, Day 5, p = 0.8081 |
| S2H | Difference in mean latency to decay during action-cue period between CckVTA and Crhr1VTA groups | 16 mice from CckVTA group, 13 mice from Crhr1VTA group | Ordinary one-way ANOVA | F (3, 42) = 23.15 | <0.0001 | **** | Bonferroni's multiple comparisons test | CckVTA vs. Crhr1VTA, p = 0.0074, CckVTA vs. DATVTA, p = 0.7857, CckVTA vs. VgatVTA, p <0.0001, Crhr1VTA vs. DATVTA, p = 0.8377, Crhr1VTA vs. VgatVTA, p <0.0001, DATVTA vs. VgatVTA, p <0.0001 |
| S3B | Difference in mean latency to decay during reward omission period between CckVTA and Crhr1VTA groups | 12 mice from CckVTA group, 13 mice from Crhr1VTA group | Unpaired t test | t=3.288, df=23 | 0.0032 | ** | NA | NA |
| S3D | Difference in baseline subtracted mean z-scored fluorescence during reward period between CckVTA and Crhr1VTA groups | 12 mice from CckVTA group, 13 mice from Crhr1VTA group | Unpaired t test | t=2.204, df=23 | 0.0378 | * | NA | NA |
| S4E | Difference in baseline subtracted mean z-scored fluorescence during reward period across previous outcome conditions for DATVTA group | 5 mice | Paired t test | t=2.204, df=4 | 0.0923 | ns | NA | NA |
| S4E | Difference in baseline subtracted mean z-scored fluorescence during reward period across previous outcome conditions for CckVTA group | 11 mice | Paired t test | t=2.793, df=10 | 0.019 | * | NA | NA |
| S4E | Difference in baseline subtracted mean z-scored fluorescence during reward period across previous outcome conditions for Crhr1VTA group | 9 mice | Paired t test | t=2.221, df=8 | 0.0571 | ns | NA | NA |

| | | | | | | | | |
|---|---|---|---|---|---|---|---|---|
| S4E | Difference in baseline subtracted mean z-scored fluorescence during reward period across previous outcome conditions for VgatVTA group | 8 mice | Paired t test | t=3.220, df=7 | 0.0147 | * | NA | NA |
| S6E | Relationship between number of starter cells and number of input cells for the rabies tracing experiment | 3 mice from CckVTA group, 3 mice from Crhr1VTA group | Pearson's correlation | r = 0.9449 | 0.0045 | ** | NA | NA |
| S6E | Relationship between number of starter cells and number of input cells for the rabies tracing experiment | 3 mice from CckVTA group, 3 mice from Crhr1VTA group | Pearson's correlation | r = 0.9449 | 0.0045 | ** | NA | NA |

**Conclusions**

Recent work has established a pattern of functional heterogeneity within and among midbrain neuronal populations in mediating motivated behavior. Given this, an important question is: What do the neural dynamics of heterogeneous midbrain populations encode and what intrinsic neuronal properties could underlie their distinct functions? To address these questions, we examined how specific aspects of reward association and motivation are regulated by heterogeneous dopaminergic and GABAergic subpopulations within the ventral tegmental area. We found that VTA dopaminergic subpopulations and the VTA GABAergic population carry distinct reward-related signals and revealed a striking pattern of functional heterogeneity among projection-defined VTA dopamine neuron populations. We believe that our comprehensive assessment of subpopulations of neurons within the VTA provides important conceptual advances that are important for our understanding of the midbrain dopamine system and motivated behavior. Further, our findings have broader implications for understanding the functional heterogeneity of neural systems in the regulation of diverse behaviors.

Projection-defined VTA dopamine subpopulations and the VTA GABA population contribute to reward association and motivation through distinct mechanisms. The *Cck*$_{VTA}$ and *Crhr1*$_{VTA}$ dopamine populations, but not the Vgat$_{VTA}$ population, preferentially encode distinct features of prediction-error, reward anticipation, and action-cue information. By contrast, the Vgat$_{VTA}$ population preferentially encodes reward retrieval and its response profile *in vivo* strongly contrasts those of VTA dopamine subpopulations. Both the neural activity dynamics and behavioral effects of neural manipulations of VTA dopamine subpopulations are consistent with distinct roles in reward association and motivation. We also found that in addition to their NAc subregion synaptic projection target, *Crhr1*$_{VTA}$ and *Cck*$_{VTA}$ subpopulations can be defined by their distinct electrophysiological properties, functional connectivity with inhibitory and disinhibitory VTA circuits, and pattern of brain-wide monosynaptic input.

Given our results, future work could be directed towards understanding the causal mechanisms associated with the membrane properties of VTA subpopulations. The suite of genetic tools outlined in our approaches could be harnessed to dissect the role of specific ion channels, pumps, and receptors that are known to regulate the intrinsic membrane properties of neurons. Further, future experiments could be targeted at

revealing the information-coding properties of monosynaptic inputs to VTA dopamine subpopulations. Critically, the causal contribution of GABAergic inhibition and disinhibition to the activity dynamics and encoding properties of VTA dopamine subpopulations during behavior remain key issues for future work. Additionally, monitoring the neural dynamics of VTA subpopulations during complex behaviors using single-cell resolution recording methods is a necessary step in revealing the functional contributions of these cells to motivated behavior in detail.

**Bibliography**


1. Adamantidis, A. R. *et al.* Optogenetic interrogation of dopaminergic modulation of the multiple phases of reward-seeking behavior. *J. Neurosci.* **31**, 10829–10835 (2011).

2. Adcock, R. A., Thangavel, A., Whitfield-Gabrieli, S., Knutson, B. & Gabrieli, J. D. E. Reward-Motivated Learning: Mesolimbic Activation Precedes Memory Formation. *Neuron* **50**, 507–517 (2006).

3. Bakhurin, K. I., Hughes, R. N., Jiang, Q., Fallon, I. P. & Yin, H. Force tuning explains changes in phasic dopamine signaling during stimulus-reward learning. *bioRxiv* 2023.04.23.537994 (2023).

4. Balleine, B. W., Delgado, M. R. & Hikosaka, O. The role of the dorsal striatum in reward and decision-making. *J. Neurosci.* **27**, 8161–8165 (2007).

5. Bayer, H. M. & Glimcher, P. W. Midbrain dopamine neurons encode a quantitative reward prediction error signal. *Neuron* **47**, 129–141 (2005).

6. Beier, K. T. *et al.* Circuit Architecture of VTA Dopamine Neurons Revealed by Systematic Input-Output Mapping. *Cell* **162**, 622–634 (2015).

7. Berridge, K. C. & Robinson, T. E. What is the role of dopamine in reward: Hedonic impact, reward learning, or incentive salience? *Brain Research Reviews* (1998) doi:10.1016/S0165-0173(98)00019-8.

8. Bouarab, C., Thompson, B. & Polter, A. M. VTA GABA Neurons at the Interface of Stress and Reward. *Front. Neural Circuits* **13**, 1–12 (2019).

9. Brischoux, F., Chakraborty, S., Brierley, D. I. & Ungless, M. A. Phasic excitation of dopamine neurons in ventral VTA by noxious stimuli. *Proc. Natl. Acad. Sci. U. S. A.* **106**, 4894–4899 (2009).

10. Bromberg-Martin, E. S., Matsumoto, M. & Hikosaka, O. Dopamine in Motivational Control: Rewarding, Aversive, and Alerting. *Neuron* **68**, 815–834 (2010).

11. Cai, L. X. *et al.* Distinct signals in medial and lateral VTA dopamine neurons modulate fear extinction at different times. *Elife* **9**, 1–23 (2020).

12. Castro, D. C. & Bruchas, M. R. A Motivational and Neuropeptidergic Hub : Anatomical and Functional Diversity within the Nucleus Accumbens Shell. *Neuron* **102**, 529–552 (2019).

13. Chergui, K. *et al.* Tonic Activation of NMDA Receptors Causes Spontaneous Burst Discharge of Rat Midbrain Dopamine Neurons In Vivo. *Eur. J. Neurosci.* **5**, 137–144 (1993).

14. Choi, J. Y. *et al.* A Comparison of Dopaminergic and Cholinergic Populations Reveals Unique Contributions of VTA Dopamine Neurons to Short-Term Memory. *Cell Rep.* **33**, (2020).

15. Chung, A. S., Miller, S. M., Sun, Y., Xu, X. & Zweifel, L. S. Sexual congruency in the connectome and translatome of VTA dopamine neurons. *Sci. Rep.* **7**, 1–11 (2017).

16. Collins, A. L. & Saunders, B. T. Heterogeneity in striatal dopamine circuits: Form and function in dynamic reward seeking. *J. Neurosci. Res.* **98**, 1046–1069 (2020).

17. Cox, J. & Witten, I. B. Striatal circuits for reward learning and decision-making. *Nature Reviews Neuroscience* (2019) doi:10.1038/s41583-019-0189-2.

18. de Jong, J. W. *et al.* A Neural Circuit Mechanism for Encoding Aversive Stimuli in the Mesolimbic Dopamine System. *Neuron* 1–19 (2018) doi:10.1016/j.neuron.2018.11.005.

19. de Jong, J. W., Liang, Y., Verharen, J. P. H., Fraser, K. M. & Lammel, S. State and rate-of-change encoding in parallel mesoaccumbal dopamine pathways. *Nat. Neurosci.* 22–26 (2024) doi:10.1038/s41593-023-01547-6.

20. Dixon, C., Sah, P., Lynch, J. W. & Keramidas, A. GABAa receptor α and γ subunits shape synaptic currents via different mechanisms. *J. Biol. Chem.* **289**, 5399–5411 (2014).

21. Doya, K. Complementary roles of basal ganglia and cerebellum in learning and motor control. *Curr. Opin. Neurobiol.* **10**, 732–739 (2000).

22. Eban-Rothschild, A., Rothschild, G., Giardino, W. J., Jones, J. R. & De Lecea, L. VTA dopaminergic neurons regulate ethologically relevant sleep-wake behaviors. *Nat. Neurosci.* **19**, 1356–1366 (2016).

23. Engelhard, B. *et al.* Specialized coding of sensory, motor and cognitive variables in VTA dopamine neurons. *Nature* **570**, 509–513 (2019).

24. Eshel, N. *et al.* Arithmetic and local circuitry underlying dopamine prediction errors. *Nature* **525**, 243–246 (2015).

25. Eshel, N., Tian, J., Bukwich, M. & Uchida, N. Dopamine neurons share common response function for reward prediction error. *Nat. Neurosci.* **19**, 479–486 (2016).

26. Faget, L. *et al.* Afferent Inputs to Neurotransmitter-Defined Cell Types in the Ventral Tegmental Area. *Cell Rep.* **15**, 2796–2808 (2016).

27. Farrant, M. & Kaila, K. The cellular, molecular and ionic basis of GABAA receptor signalling. *Prog. Brain Res.* **160**, 59–87 (2007).

28. Farrell, K. *et al.* Article Midbrain dopamine neurons signal phasic and ramping reward prediction error during goal- directed navigation ll ll Midbrain dopamine neurons signal phasic and ramping reward prediction error during goal-directed navigation. *CellReports* **41**, 111470 (2022).

29. Floresco, S. B. The Nucleus Accumbens : An Interface Between Cognition , Emotion , and Action. (2015) doi:10.1146/annurev-psych-010213-115159.

30. Fürth, D. *et al.* An interactive framework for whole-brain maps at cellular resolution HHS Public Access Author manuscript. *Nat Neurosci* **21**, 139–149 (2018).

31. Gan, J. O., Walton, M. E. & Phillips, P. E. M. Dissociable cost and benefit encoding of future rewards by mesolimbic dopamine. *Nat. Neurosci.* **13**, 25–27 (2010).

32. Glasgow, S. D., McPhedrain, R., Madranges, J. F., Kennedy, T. E. & Ruthazer, E. S. Approaches and limitations in the investigation of synaptic transmission and plasticity. *Front. Synaptic Neurosci.* **11**, 1–16 (2019).

33. Grove, J. C. R. *et al.* Dopamine subsystems that track internal states. *Nature* **608**, 374–380 (2022).

34. Gunaydin, L. A. *et al.* Natural neural projection dynamics underlying social behavior. *Cell* **157**, 1535–1551 (2014).

35. Hamid, A. A. *et al.* Mesolimbic dopamine signals the value of work. *Nat. Neurosci.* **19**, 117–126 (2015).

36. Harris, J. J., Kollo, M., Erskine, A., Schaefer, A. & Burdakov, D. Natural VTA activity during NREM sleep influences future exploratory behavior. *iScience* **25**, 104396 (2022).

37. Heymann, G. *et al.* Synergy of Distinct Dopamine Projection Populations in Behavioral Reinforcement. *Neuron* **105**, 909-920.e5 (2020).

38. Hoang, I. B. *et al.* A novel hypothalamic-midbrain circuit for model-based learning. 1–44 (2023).

39. Hodos, W. Progressive ratio as a measure of reward strength. *Science (80-. ).* **134**, 943–944 (1961).

40. Horvitz, J. C. Mesolimbocortical and nigrostriatal dopamine responses to salient non- reward events. *Neuroscience* **96**, 651–656 (2000).

41. Howe, M. W., Tierney, P. L., Sandberg, S. G., Phillips, P. E. M. & Graybiel, A. M. Prolonged dopamine signalling in striatum signals proximity and value of distant rewards. *Nature* **500**, 575–579 (2013).

42. Jeong, H. Mesolimbic dopamine release conveys causal associations. **34**, 642–685 (2022).

43. Jhou, T. C., Fields, H. L., Baxter, M. G., Saper, C. B. & Holland, P. C. The Rostromedial Tegmental Nucleus (RMTg), a GABAergic Afferent to Midbrain Dopamine Neurons, Encodes Aversive Stimuli and Inhibits Motor Responses. *Neuron* **61**, 786–800 (2009).

44. Jin, M. *et al.* SMART: An Open-Source Extension of WholeBrain for Intact Mouse Brain Registration and Segmentation. *eNeuro* **9**, 1–15 (2022).

45. Jo, Y. S., Heymann, G. & Zweifel, L. S. Dopamine Neurons Reflect the Uncertainty in Fear Generalization. *Neuron* **100**, 916-925.e3 (2018).

46. Johnson, S. W. & North, R. A. Two types of neurone in the rat ventral tegmental area and their synaptic inputs. *J. Physiol.* **450**, 455–468 (1992).

47. Juan, P., Barandela, M. & Jim, C. The Dopaminergic Control of Movement-Evolutionary Considerations. (2021).

48. Juarez, B. *et al.* Temporal scaling of dopamine neuron firing and dopamine release by distinct ion channels 1 shape behavior. **8869**, 1–16 (2023).

49. Kelley, A. N. N. E. Functional Specificity of Ventral Striatal Compartments in Appetitive Behaviors ANN. *Ann. NEW YORK Acad. Sci.* (1999).

50. Lammel, S. *et al.* Unique Properties of Mesoprefrontal Neurons within a Dual Mesocorticolimbic Dopamine System. *Neuron* **57**, 760–773 (2008).

51. Lammel, S., Ion, D. I., Roeper, J. & Malenka, R. C. Projection-Specific Modulation of Dopamine Neuron Synapses by Aversive and Rewarding Stimuli. *Neuron* **70**, 855–862 (2011).

52. Lammel, S. *et al.* Input-specific control of reward and aversion in the ventral tegmental area. *Nature* **491**, 212–217 (2012).

53. Madangopal, R. *et al.* Incubation of palatable food craving is associated with brain-wide neuronal activation in mice. *Proc. Natl. Acad. Sci. U. S. A.* **119**, 1–11 (2022).

54. Markowitz, J. E. *et al.* Spontaneous behaviour is structured by reinforcement without explicit reward. (2022) doi:10.1038/s41586-022-05611-2.

55. Mohebi, A. *et al.* Dissociable dopamine dynamics for learning and motivation. *Nature* **570**, 65–70 (2019).

56. Morales, M. & Margolis, E. B. Ventral tegmental area: Cellular heterogeneity, connectivity and behaviour. *Nat. Rev. Neurosci.* **18**, 73–85 (2017).

57. Nair-Roberts, R. G. *et al.* Stereological estimates of dopaminergic, GABAergic and glutamatergic neurons in the ventral tegmental area, substantia nigra and retrorubral field in the rat. *Neuroscience* **152**, 1024–1031 (2008).

58. Nieh, E. H. *et al.* Inhibitory Input from the Lateral Hypothalamus to the Ventral Tegmental Area Disinhibits Dopamine Neurons and Promotes Behavioral Activation. *Neuron* **90**, 1286–1298 (2016).

59. Niv, Y., Daw, N. D., Joel, D. & Dayan, P. Tonic dopamine: Opportunity costs and the control of response vigor. *Psychopharmacology (Berl).* **191**, 507–520 (2007).

60. Nugent, A. L., Anderson, E. M., Larson, E. B. & Self, D. W. Incubation of cue-induced reinstatement of cocaine, but not sucrose, seeking in C57BL/6J mice. *Pharmacol. Biochem. Behav.* **159**, 12–17 (2017).

61. O'Doherty, J. P., Cockburn, J. & Pauli, W. M. Learning , Reward , and Decision Making. (2017) doi:10.1146/annurev-psych-010416-044216.

62. O'Doherty, J. *et al.* Dissociable Roles of Ventral and Dorsal Striatum in Instrumental Conditioning. *Science (80-. ).* **304**, 452–454 (2004).

63. Ogawa, S. K., Cohen, J. Y., Hwang, D., Uchida, N. & Watabe-Uchida, M. Organization of monosynaptic inputs to the serotonin and dopamine neuromodulatory systems. *Cell Rep.* **8**, 1105–1118 (2014).

64. Parker, N. F. *et al.* Choice-selective sequences dominate in cortical relative to thalamic inputs to NAc to support reinforcement learning. *Cell Rep.* **39**, 110756 (2022).

65. Poulin, J. *et al.* Mapping projections of molecularly defined dopamine neuron subtypes using intersectional genetic approaches. *Nat. Neurosci.* doi:10.1038/s41593-018-0203-4.

66. Renier, N. *et al.* Mapping of Brain Activity by Automated Volume Analysis of Immediate Early Genes. *Cell* **165**, 1789–1802 (2016).

67. Saddoris, M. P., Cacciapaglia, F., Wightman, R. M. & Carelli, R. M. Differential dopamine release dynamics in the nucleus accumbens core and shell reveal complementary signals for error prediction and incentive motivation. *J. Neurosci.* **35**, 11572–11582 (2015).

68. Salamone, J. Interference With Accumbens Dopamine Transmission Makes Rats More Sensitive To Work Requirements But Does Not Impair Primary Food Reinforcement. *Behav. Pharmacol.* **10**, S79 (1999).

69. Salamone, J. D. & Correa, M. The Mysterious Motivational Functions of Mesolimbic Dopamine. *Neuron* **76**, 470–485 (2012).

70. Salinas-Hernández, X. I. *et al.* Dopamine neurons drive fear extinction learning by signaling the omission of expected aversive outcomes. *Elife* **7**, 1–25 (2018).

71. Sanford, C. A. *et al.* A Central Amygdala CRF Circuit Facilitates Learning about Weak Threats. *Neuron* **93**, 164–178 (2017).

72. Saunders, B. T., Richard, J. M., Margolis, E. B. & Janak, P. H. Dopamine neurons create Pavlovian conditioned stimuli with circuit-defined motivational properties. *Nat. Neurosci.* **21**, 1072–1083 (2018).

73. Schultz, W., Dayan, P. & Montague, P. R. A neural substrate of prediction and reward. *Science (80-. ).* **275**, 1593–1599 (1997).

74. Schultz, W. Predictive reward signal of dopamine neurons. *J. Neurophysiol.* **80**, 1–27 (1998).

75. Segal, M. Dendritic spines, synaptic plasticity and neuronal survival: Activity shapes dendritic spines to enhance neuronal viability. *Eur. J. Neurosci.* **31**, 2178–2184 (2010).

76. Simon, R. C. *et al.* Opto-seq reveals input-specific immediate early gene induction in ventral tegmental area cell types. (2023).

77. Soden, M. E. *et al.* Anatomic resolution of neurotransmitter-specific projections to the VTA reveals diversity of GABAergic inputs. *Nat. Neurosci.* 1–13 (2020) doi:10.1038/s41593-020-0657-z.

78. Soden, M. E. *et al.* Distinct Encoding of Reward and Aversion by Peptidergic BNST Inputs to the VTA. *Front. Neural Circuits* **16**, 1–13 (2022).

79. Solié, C., Girard, B., Righetti, B., Tapparel, M. & Bellone, C. VTA dopamine neuron activity encodes social interaction and promotes reinforcement learning through social prediction error. *Nat. Neurosci.* **25**, 86–97 (2022).

80. Sun, Y. *et al.* Cell-type-specific circuit connectivity of hippocampal CA1 revealed through cre-dependent rabies tracing. *Cell Rep.* **7**, 269–280 (2014).

81. Szelenyi, E. R. *et al.* An arginine-rich nuclear localization signal (ArgiNLS) strategy for streamlined image segmentation of single-cells. *bioRxiv* 2023.11.22.568319 (2023).

82. Tan, K. R. *et al.* GABA Neurons of the VTA Drive Conditioned Place Aversion. *Neuron* **73**, 1173–1183 (2012).

83. Tian, J. *et al.* Distributed and Mixed Information in Monosynaptic Inputs to Dopamine Neurons. *Neuron* **91**, 1374–1389 (2016).

84. Torquet, N. *et al.* Social interactions impact on the dopaminergic system and drive individuality. *Nat. Commun.* **9**, 1–11 (2018).

85. Tsai, H.-C. *et al.* Phasic Firing in Dopaminergic Neurons Is Sufficient for Behavioral Conditioning. *Science (80-. ).* **324**, 1080–1084 (2009).

86. van Elzelingen, W. *et al.* A unidirectional but not uniform striatal landscape of dopamine signaling for motivational stimuli. *Proc. Natl. Acad. Sci. U. S. A.* **119**, 1–12 (2022).

87. Van Zessen, R., Phillips, J. L., Budygin, E. A. & Stuber, G. D. Activation of VTA GABA Neurons Disrupts Reward Consumption. *Neuron* **73**, 1184–1194 (2012).

88. Wanat, M. J., Kuhnen, C. M. & Phillips, P. E. M. Delays conferred by escalating costs modulate dopamine release to rewards but not their predictors. *J. Neurosci.* **30**, 12020–12027 (2010).

89. Wassum, K. M., Ostlund, S. B. & Maidment, N. T. Phasic mesolimbic dopamine signaling precedes and predicts performance of a self-initiated action sequence task. *Biol. Psychiatry* **71**, 846–854 (2012).

90. Watabe-Uchida, M., Zhu, L., Ogawa, S. K., Vamanrao, A. & Uchida, N. Whole-Brain Mapping of Direct Inputs to Midbrain Dopamine Neurons. *Neuron* **74**, 858–873 (2012).

91. Witten, I. B. *et al.* Recombinase-driver rat lines: Tools, techniques, and optogenetic application to dopamine-mediated reinforcement. *Neuron* **72**, 721–733 (2011).

92. Xu, N. *et al.* Functional Connectivity of the Brain Across Rodents and Humans. *Front. Neurosci.* **16**, 1–27 (2022).

93. Yang, H. *et al.* Nucleus Accumbens Subnuclei Regulate Motivated Behavior via Direct Inhibition and Disinhibition of VTA Dopamine Subpopulations. *Neuron* **97**, 434-449.e4 (2018).

94. Zweifel, L. S. *et al.* Disruption of NMDAR-dependent burst firing by dopamine neurons provides selective assessment of phasic dopamine-dependent behavior. *Proc. Natl. Acad. Sci. U. S. A.* **106**, 7281–7288 (2009).